PRODUCTION OF HIGH SPECIFIC ACTIVITY RHENIUM-186 FOR RADIOTHERAPEUTIC APPLICATIONS AND REFORMULATION OF A NOVEL LIQUID BRACHYTHERAPY AGENT

A Dissertation

Presented to

the Faculty of the Graduate School

at the University of Missouri-Columbia

In Partial Fulfilment

of the Requirements for the Degree

Doctor of Philosophy

By

ANSTER CHARLES

Dr. Silvia S. Jurisson, Dissertation Advisor

Dr. Heather M. Hennkens, Dissertation Advisor

July 2022

The undersigned, approved by the dean of the Graduate School, have examined the dissertation entitled

PRODUCTION OF HIGH SPECIFIC ACTIVITY RHENIUM FOR RADIOTHERAPEUTIC APPLICATIONS AND REFORMULATION OF A NOVEL LIQUID BRACHYTHERAPY AGENT

presented by Anster Charles, a candidate for the degree of Doctor of Philosophy, and hereby certify that, in their opinion, it is worthy of acceptance.

_____

Dr. Silvia S. Jurisson

_____

Dr. Heather M. Hennkens

_____

Dr. C. Michael Greenlief

_____

Dr. Gary L. Solbrekken

DEDICATION

This thesis is dedicated to my parents, Antoine and Alice, and my siblings, Antonia and Alister who have supported me immensely over the years. I would not make it this far without you.

ACKNOWLEDGMENTS

I would like to thank Dr. C. Michael Greenlief and Dr. Gary S. Solbrekken for serving on my committee and providing me with advice during the process.

I also extend my gratitude to the collaborators who helped me accomplish my studies for my various projects. Dr. Scot Wilbur, Dr. Yawen Li, Dr. Firouzeh Najafi, Dr. Li Ma, Chathurya Munindradasa, and Rebecca Hoerres were instrumental in the rhenium production, separation, and radiolabeling work. The Isotherapeutics Group, Dr. Charles Maitz, Dr. David Stalla, Lisa Watkinson, and Terry Carmack all made significant contributions towards my yttrium hydroxycarbonate microparticle studies. Dr. John Lydon and Mary Embree provided assistance and ideas for several projects that I worked on. Alex Saale, and Michael Hall of Essential Isotopes assisted with cyclotron irradiations of targets. The members of the Jurisson and Hennkens groups provided assistance throughout my studies by providing ideas and revising presentations.

TABLE OF CONTENTS

LIST OF FIGURES

LIST OF TABLES

ACADEMIC ABSTRACT

The continued development of methods for the production and separation of high specific activity (HSA) rhenium-186 ($t_{1/2}$ = 90.64 h, $E_{\beta\text{-ave}}$ = 359 keV (71%), 306 keV (22%)) would largely increase its use as a therapeutic analogue to the widely used ^{99m}Tc ($t_{1/2}$ = 6.01 h, E_{γ} = 141 keV (89%)). Rhenium-186 has favorable decay properties that make it an attractive candidate for radioimmunotherapy, providing that the radionuclide can be obtained in high specific activity. The similar chemical characteristics of Re and Tc in theory may allow ^{186}Re-based radiopharmaceuticals to be developed as therapeutic analogues to their ^{99m}Tc counterparts. In this research, two methods were evaluated for the production and separation of HSA ^{186}Re, and several methods were also evaluated for their efficiency in the selective separation of ^{186}Re post production, as well as high recovery of the costly enriched target material.

Yttrium-90 ($t_{1/2}$ = 64 h, $E_{\beta\text{-max}}$ = 2.28 MeV (99.99%)) also displays excellent decay properties for targeted radiotherapy, which is exploited by the formulation of a novel liquid brachytherapy agent, BetaBrach™. The HSA ^{90}Y utilized for the current formulation of BetaBrach™ can be replaced by low specific activity (LSA) ^{90}Y produced in a nuclear reactor. Replacing HSA ^{90}Y with LSA ^{90}Y may offer significant economic advantages if the demand for BetaBrach™ requires large scale production of ^{90}Y. Thus, this work also evaluates the chemical and physical characterization of LSA ^{90}Y formulated BetaBrach™ as well as its therapeutic efficacy.

Chapter 1

Introduction

1.1 Background on radiopharmaceuticals

Radiopharmaceuticals are a subset of pharmaceuticals that contain radioactive isotopes for diagnostic and/ or therapeutic medical applications [1, 2]. The nuclear properties of the radionuclide incorporated into a radiopharmaceutical determine its modality [3]. Electromagnetic ionizing radiation is predominantly utilized for imaging in medical applications due to its inherent ability to penetrate matter, and conversely, the short range of particulate ionizing radiation is employed in therapy [4, 5].

1.2 Characteristics of radioactive decay

Radioactive decay is a phenomenon used to describe the spontaneous emission of ionizing radiation by unstable nuclei, usually in three basic forms aptly named alpha (α) decay, beta (β) decay, and gamma (γ) decay to denote their respective penetrating ability in increasing order [6]. Alpha decay is observed in most heavy nuclei with $Z > 83$ through the emission of a monoenergetic $^{4}He^{2+}$ particle from the nucleus of the unstable parent, resulting in a 4 unit decrease in atomic mass (**Table 1**) [6]. Due to the relatively high mass and charge of α particles, they travel a short distance before coming to a full stop [6, 7].

Table 1: Characteristics of Radioactive Decay.

Decay Type	Emission	ΔZ	ΔN	ΔA	Example	Occurrence
α	$^{4}He^{2+}$	-2	-2	-4	$^{223}Ra \rightarrow {}^{219}Rn + \alpha$	$Z > 83$
β^-	$e^-, \bar{\nu}_e$	+1	-1	0	$^{186}Re \rightarrow {}^{186}Os + \beta^- + \bar{\nu}_e$	$N/Z > (N/Z)_{stable}$
β^+	e^+, ν_e	-1	+1	0	$^{18}F \rightarrow {}^{18}O + \beta^+ + \nu_e$	$N/Z < (N/Z)_{stable;}$ electropositive nuclei
EC	ν_e	-1	+1	0	$e^- + {}^{207}Bi \rightarrow {}^{207}Pb + \nu_e$	$N/Z < (N/Z)_{stable;}$ alternative to β^+
γ	Photon	0	0	0	$^{99m}Tc \rightarrow {}^{99}Tc + \gamma$	Excited nuclei
IC	Electron	0	0	0	$^{203*}Tl \rightarrow {}^{203}Tl + e^-$	Alternative to γ–ray

Beta decay is observed in nuclei that are either neutron-rich or proton-rich. Radioactive decay in a neutron-rich nucleus is achieved by the concurrent conversion of a nuclear neutron into a proton along with the ejection of an energetic β^- particle and an antineutrino ($\bar{\nu}_e$) (**Figure 1**) [6, 8]. Conversely, a proton-rich nucleus may decay via the conversion of a nuclear proton into a neutron and an energetic β^+ particle and a neutrino (ν_e), [6, 9]. Since the energy is shared between the emitted β and ν particles, a continuous energy spectrum ranging from zero to the decay energy can be measured for beta decay. The combination of the relatively low mass of β particles and single charge results in a higher penetrative power when compared to α particle decay. Electron capture (EC) is another form of radioactive decay that occurs in proton rich nuclei and is observed mostly in heavier nuclei, where practically all the energy is taken away by the

emitted neutrino with the simultaneous absorption of an electron from the K or L electron shell and conversion of a nuclear proton into a neutron [6, 10]. Auger electrons and X-rays follow to fill the vacancy of the ejected electron. Conversely, light proton-rich nuclei favor β^+ emission.

Excited nuclei may lose energy by the emission of a γ ray to achieve a more stable nuclear state [6]. The energy of the emitted photon is determined by the energy difference between the metastable state and the relaxed state. Internal conversion (IC) is an alternative route to achieve stability whereby the excited nucleus transfers its energy to an orbital electron, which is then ejected from the atom and is followed by Auger electrons and X-ray emissions [6, 11].

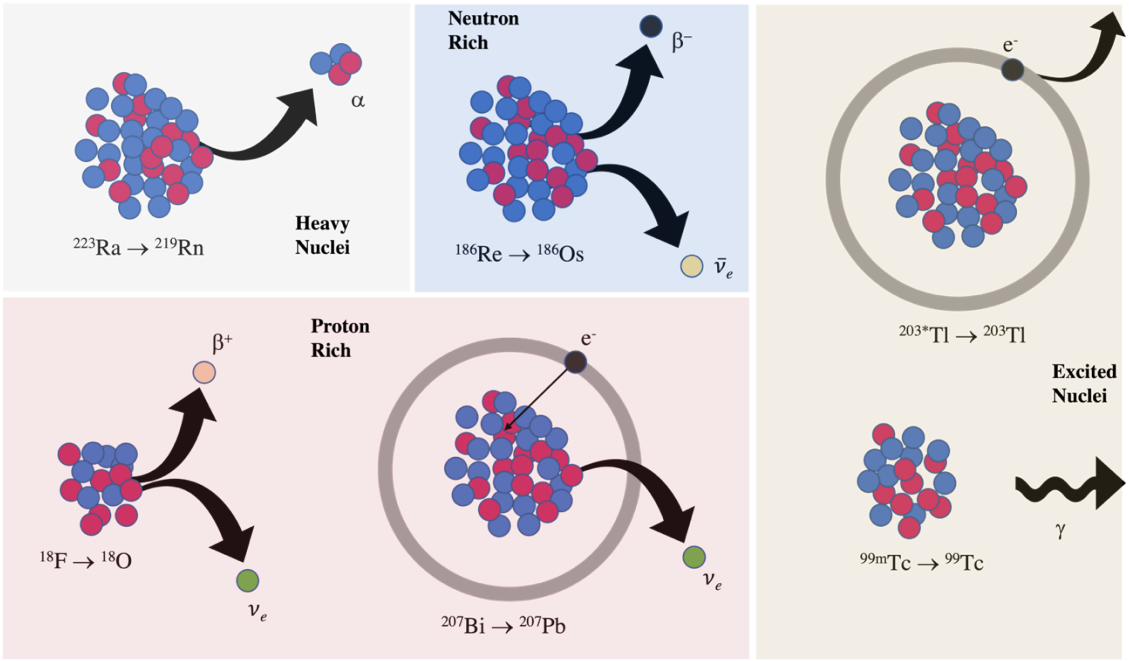

Figure 1: Types of radioactive decay. Left to right: α decay, β^- decay, IC, β^+ decay, EC, γ decay.

1.3 Applications of radiopharmaceuticals

Ionization of the chemical bonds in biological matter is usually observed following the absorption of large amounts of energy from an exposure to ionizing radiation [12]. The energy associated with the bonds in organic compounds (<10 eV) is much lower than the energy dissipated per ionization event (33 eV) [13, 14]. Following the characterization of radioactivity by Marie Curie in the late nineteenth century, Pierre Curie demonstrated the cell killing ability of ionizing radiation by holding a tube of radium against his arm to produce an ulceration [15, 16]. This newly discovered alkaline earth metal was quickly found to exhibit cancer suppressing properties upon insertion into tumors, resulting in an entirely new form of treatment referred to as brachytherapy. By the 1920s, the rarity and demand for radium-226 was so high that 1 gram was worth $100,000 ($1.3 million in today's money) [17]. Eventually, as the genetic and biological effects of radiation exposure were increasingly understood in more detail, it became apparent that more precise forms of radiotherapy needed to be developed to avoid collateral damage to healthy tissues [18].

We now know that the biological effects of radiation are induced by damage to one of the most critical targets of therapeutic radiopharmaceuticals; deoxyribonucleic acid (DNA) [19]. The absorption of any form of ionizing radiation – electromagnetic or charged and uncharged particles may lead to interactions with the critical targets of cells [19]. Direct action of radiation is the dominant process if radiation with a high linear energy transfer (LET), such as alpha particles, ionize atoms of the target and lead to biological changes. Alternatively, indirect action is dominant when low LET radiation (γ rays, β^-, photons)

may produce free radicals such as $H_2O^{\bullet}$, $^{\bullet}OH$, and $H^{\bullet}$ from interactions with water molecules in the cell that can cause critical damage to the nucleus [20–22].

Advances in radiopharmaceuticals for tumor diagnosis and therapy have led to the emergence of various drug modalities designed for specific uptake of radionuclides into their intended targets. One of the simplest examples of targeted therapy is ^{223}Ra in the form of $[^{223}Ra]RaCl_2$ for the treatment of metastatic bone cancer. Radium-223 ($t_{1/2}$ = 11.43 d, E_{α} = 5.7 MeV (51.6%), 5.6 MeV (25.2%)) behaves as a calcium mimic so upon administration, it is preferentially absorbed by actively growing bone tissue (**Figure 2**) [23, 24].

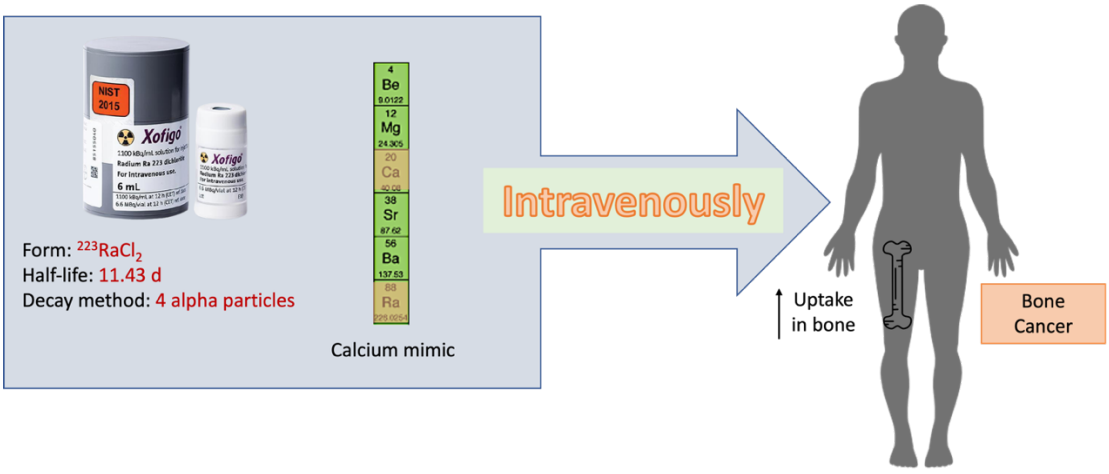

Figure 2: Mechanism of action for ^{223}Ra containing Xofigo®.

Another targeted approach, brachytherapy, generally uses surgically implanted sealed radiation sources that are placed either inside or next to the area requiring treatment. This allows the radiation to affect only a very localized area surrounding the implant, thus limiting the cytotoxic effects to surrounding tissues. ^{192}Ir-encased metal brachytherapy seeds ($t_{1/2}$ = 73.8 d, $E_{\beta\text{-Avg}}$ = 208 keV (48%), 160 keV (41%)) represent one of the more

common forms of brachytherapy used in the treatment of several types of cancer such as cervical cancer, prostate cancer, and head and neck cancer (**Figure 3**) [25, 26].

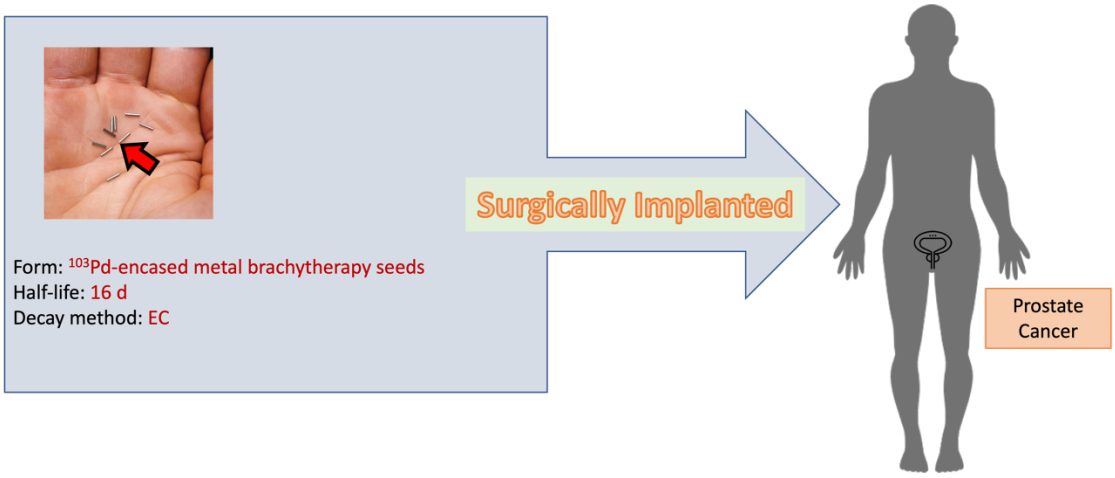

Figure 3: Implanted brachytherapy beads for prostate cancer treatment.

Fluorodeoxyglucose (^{18}F), also commonly known as [^{18}F]FDG is a medical metabolic radiotracer used for positron emission tomography (PET) [9, 27]. Unlike a normal glucose molecule, the hydroxyl group at the C-2 carbon is replaced with the positron-emitting radionuclide, fluorine-18 ($t_{1/2}$ = 109.77 min, $E_{\beta+\,Avg}$ = 249 keV (96.7%)) in [^{18}F]FDG [27]. Tissues such as the brain and tumors that exhibit uptake of glucose have a high metabolism, thus [^{18}F]FDG serves as a marker for the uptake of glucose (**Figure 4**). [^{18}F]FDG molecules accumulate in these targeted tissues after intravenous administration because the metabolism of [^{18}F]FDG is inhibited by the absence of the hydroxyl group at the C-2 carbon which prevents the molecule from exiting the cell before radioactive decay. A PET scanner can be used to detect the annihilation photons that are emitted at approximately 180° apart with a resolving time in the picosecond to nanosecond range to determine their point of origin [28]. This raw data is then used for image reconstruction

to create 2D and 3D images that show the intensity of the distribution of the glucose analogue.

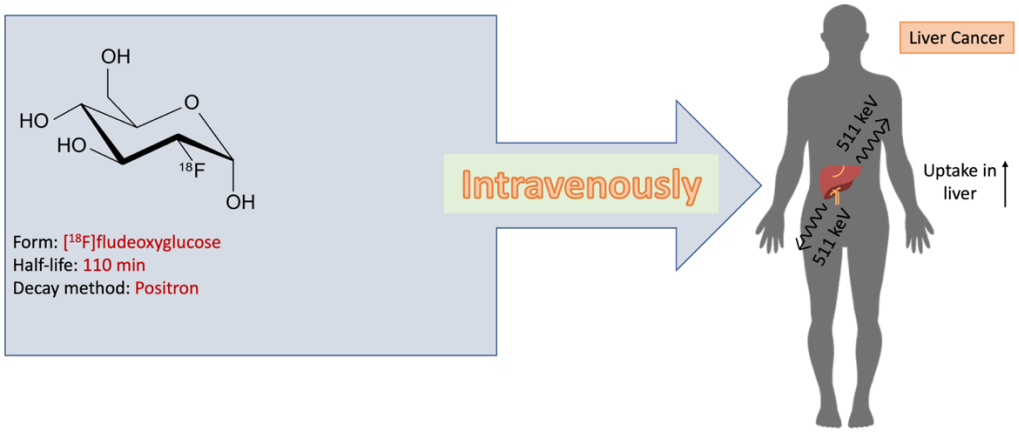

Figure 4: Administration of [^{18}F]fludeoxyglucose for PET imaging.

Radioactive isotopes of metals, also known as radiometals, are commonly used in diagnostic and therapeutic radiopharmaceuticals, with ^{99m}Tc being the most utilized for single-photon emission computed tomography (SPECT) [29, 30]. The design of most radiometal-based radiopharmaceuticals aims to maximize *in vivo* stability, which is achieved by coordination of the radiometal with a chelator to form a metal-ligand complex. Several prominent radiopharmaceuticals have employed this approach including ^{99m}Tc-based Sestamibi™ and Ceretec™ ($t_{1/2}$ = 6.01 h, E_γ = 140 keV (89%)), and ^{153}Sm-based Quadramet™ ($t_{1/2}$ = 46.28 h, E_{β^-} = 225 keV (49.4%), 199 keV (31.3%)) (**Figure 5**) [30].

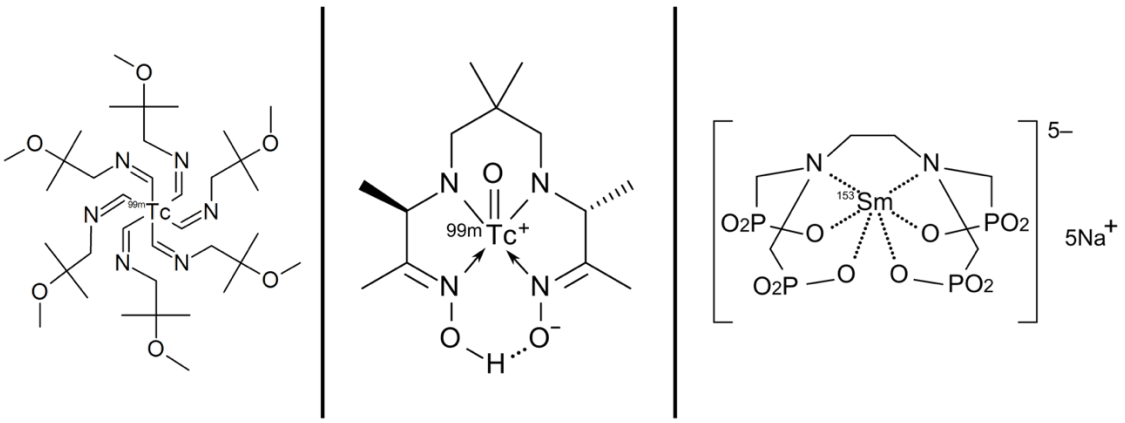

Figure 5: Left to right, structures of Sestamibi™, Ceretec™ and Quadramet™.

The bifunctional chelator approach is a more recent, sophisticated, and powerful technique for overcoming one of the main obstacles in radioimaging and radiotherapy, specific localization in diseased tissues [31]. The general design of a bifunctional chelator includes a chelated radiometal attached to a targeting molecule such as a peptide or antibody via a linker (**Figure 6**). The high affinity of the selected targeting moiety for its counterpart over-expressed receptor on target cells results in the localized accumulation of the radiopharmaceutical post injection, followed by rapid clearance from the blood and other normal organs to minimize their exposure to cytotoxic radiation [31].

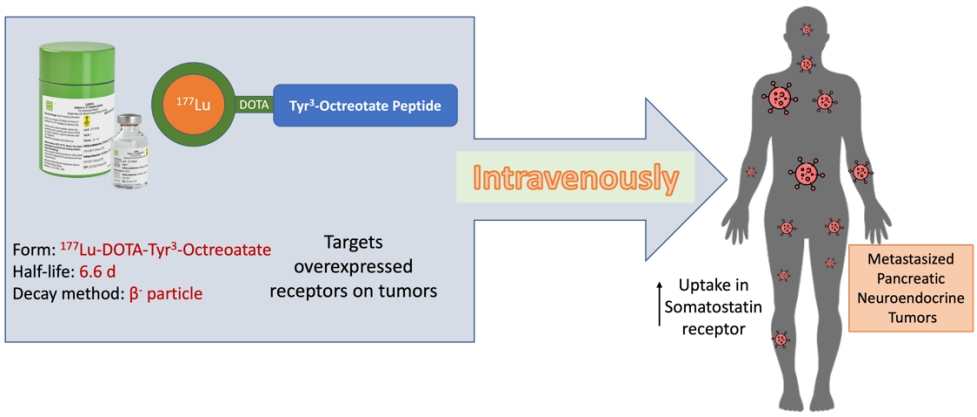

Figure 6: Example of a targeted radiotherapeutic bifunctional chelator, ^{177}Lu-DOTA-Octreotate.

1.4 Radionuclide production methods

Most radionuclides relevant to nuclear medicine are not available naturally, thus, artificial radionuclides are produced via a variety of nuclear reaction pathways induced by charged particle bombardment, neutron irradiation, fission, photon induced reactions, etc [32]. Charged particle bombardment is typically achieved by the acceleration of ions in a particle accelerator toward a stationary target to induce nuclear reactions [32, 33] (**Figure 7**). Neutron irradiation of targets is mainly performed by exposing the target material to the neutron field generated by the fission of ^{235}U in a nuclear reactor [34]. To obtain maximum radionuclidic yield and purity, it is critical to optimize the design of the target. For charged-particle radionuclide production in accelerators, the thickness and density of the target determines its stopping power, and consequently, the energy of the particles as they travel through the target [33]. The energy of the charged particles determines the cross-section or probability of a nuclear reaction; therefore, the thickness of the target must be calculated prior to bombardment so that the maximum cross-section

of the desired nuclear reaction can be exploited. The production of radionuclides in an accelerator is described by **Equation 1**.

$$Y = \frac{N_A \cdot I}{A_T}\left(1 - e^{-\lambda \cdot t}\right)\int_{E_E}^{E_I} \sigma_T(E)\frac{dE}{S_T(E)}$$

Equation 1

where Y is the radioisotope yield at end of bombardment (EOB) in Bq, N_A is the number of target nuclei, I is the incident particle flux per second and is related to the beam current, A_T is the atomic mass number of the target nucleus, λ is the decay constant in s^{-1} and is equal to $\ln(2)/t_{1/2}$, t is the irradiation time in seconds, E_I is the incident energy of the beam particles, E_E is the exit energy of the beam particles, σ_T is the cross section of the target nuclei in cm^2, and S_T is the total stopping power.

The neutron flux in reactors irradiates targets three-dimensionally so the geometry of the target is less important, however, the mass of the target is proportional to the product yield [34]. The production of radionuclides in a reactor is described by **Equation 2**.

$$Y = N_o \cdot \sigma \cdot \phi \cdot \left(1 - e^{\lambda \cdot t}\right)$$

Equation 2

Where Y is the radioisotope yield at end of irradiation (EOI) in Bq, N_o is the number of nuclei of the target, σ is the reaction cross section in cm^2, ϕ is the neutron flux in $n/cm^2/s$,

λ is the decay constant in s^{-1} and is equal to $\ln(2)/t_{1/2}$, and, t is the irradiation time in seconds.

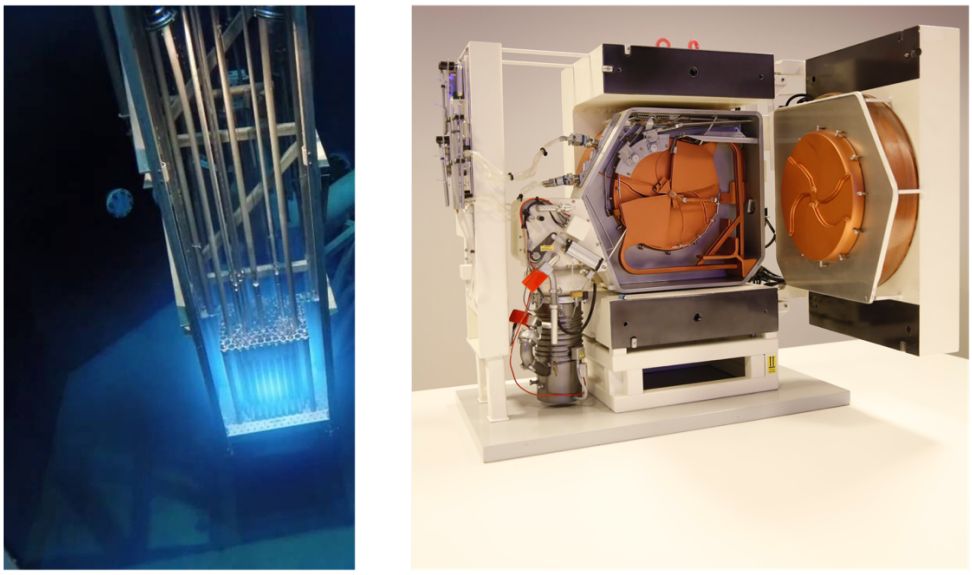

Figure 7: Left, a water moderated nuclear reactor and right, a medical cyclotron used for radionuclide production.

1.5 Basics of targetry

A key requirement for radionuclide production involves preparation of the targets that will be subjected to either charged particle or neutron irradiation. A target material of high purity, low cost, sustainable recyclability, and suitable chemical and physical form is essential to ensure the security of the supply of the therapeutic radionuclides [32]. Each radionuclide also has unique radiochemical properties and requires a specific and efficient production process as well as effective methods for separation from the target material when needed. A thorough understanding of the relevant nuclear reactions is also

critical to maximize yields of the intended radionuclide, while minimizing the production of contaminant nuclides.

The composition of targets is also very important, and the physical form of targets may include powders, foils, electrodeposited films, pressed pellets, liquids, and gases [33]. Metals are typically highly favored due to their high melting points, high thermal conductivity, high melting point, and high density of target atoms. Sometimes, compound materials such as oxides, sulfides and other salts containing a lower density of target atoms are used in both reactor and accelerator production over metals because they offer higher chemical stability under irradiation, are more readily available commercially, and/ or simplify the post-irradiation process. For example, ytterbium oxide, Yb_2O_3 is used to produce ^{177}Lu via the $^{176}Yb(n,\gamma)^{177}Y \xrightarrow{\beta-} ^{177}Lu$ nuclear reaction in a reactor because the instability of Yb metal under reactor conditions causes oxidation. Aluminum perrhenate, $Al(ReO_4)_3$, is used for ^{186}Re production because it helps to simplify the post irradiation dissolution process. Nickel metal targets are prepared by electrodeposition on a gold backing for the production of ^{64}Cu by way of the $^{64}Ni(p,n)^{64}Cu$ nuclear reaction in a cyclotron.

1.6 Challenges of charged particle irradiations

The final yield of the product radionuclide in an accelerator is directly proportional to the amount of time the target is irradiated and the irradiation current. The amount of radioactivity required for experimental studies and clinical applications depends on the physical properties of the radionuclide and end application, and ranges from single digit to several thousand millicuries [4, 5]. Thus, radionuclides obtained via charged particle

irradiation should maximize the current and time exposure of the targets. Unfortunately, the heat generated in the target is proportional to the current and deposited energy, **Equation 3.**

$$P = \Delta E \cdot I \qquad \textbf{Equation 3}$$

where P is the power in Watts (W), ΔE is the energy in MeV, and I is the current in μA. A beam degraded from 30 MeV to 0 MeV with a 100 μA current deposits 3000 W into an irradiated target. Inadequate removal of the heat may lead to target failure through physical phase changes such as melting or boiling, which may lead to lost material and contamination [33]. A critical component of target design involves removal of the induced heat by improving the cooling efficiency of targets through the exploitation of heat transfer **Equations 4** and **5**.

$$\Delta E \cdot I = Q_{total} \qquad \textbf{Equation 4}$$

$$Q_{total} = Q_{cond} + Q_{conv} + Q_{rad} \qquad \textbf{Equation 5}$$

where Q_{cond} is the heat lost by conduction, Q_{conv} is the heat lost by convection, and Q_{rad} is the heat lost by radiation.

The basic design of solid targets achieves removal of heat by contacting the target material to a highly thermal conducting metal backing to facilitate conductive heat

transfer away from the material [35]. Transfer of heat away from the backing material is achieved via convective heat transfer with a turbulent water flow rate. Radiative heat transfer becomes relevant at temperatures exceeding 500 °C (**Figure 8**).

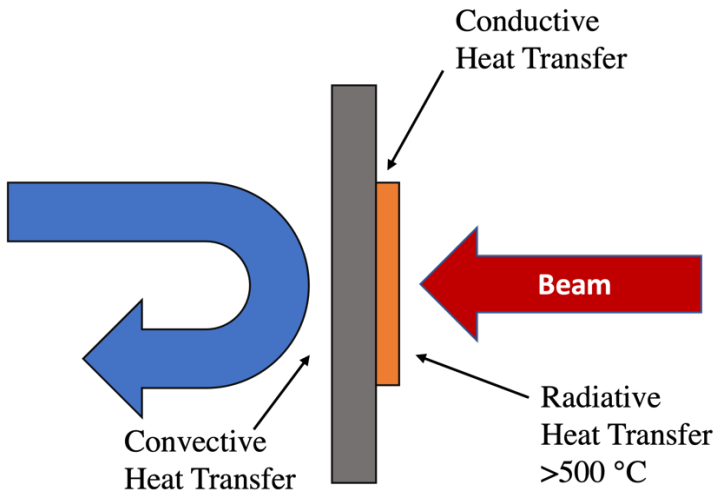

Figure 8: The basic process of heat transfer in an accelerator irradiated solid target.

1.7 Separation Techniques

In most cases, after a radionuclide is produced, it is critical to implement quick and robust methods to separate the product from the starting target material and co-produced contaminants to minimize the loss of product and ensure high purity of the product. This is usually achieved through the application of techniques such as chromatography and liquid-liquid extraction [36, 37]. Other methods, including distillation and precipitation, are used less frequently.

Chromatography is generally considered to be one of the most practical separation methods and is the most widely used technology for the isolation and purification of a radionuclide product. Two common types of chromatography are ion exchange

chromatography and extraction chromatography [36]. Ion exchange chromatography relies on the reversible exchange of ions in solution with ions electrostatically bound to the surface of a support media based on their charge density. An example of the application of ion exchange chromatography can be seen in the purification of ^{99}Mo for the preparation of $^{99}Mo/^{99m}Tc$ generators. A molybdate ($^{99}MoO_4^{2-}$) solution is loaded onto on a Dowex-1 anion exchange column, which is then washed with concentrated HCl to elute impurities. The adsorbed $^{99}MoO_4^{2-}$ is converted to ammonium heptamolybdate $(NH_4)_6Mo_7O_{24}$ using aqueous ammonia followed by elution with dilute HCl [38]. $^{99}Mo/^{99m}Tc$ generators exploit the difference in adsorption of $^{99}MoO_4^{2-}$ and pertechnetate ($^{99m}TcO_4^-$) to acidified alumina columns to routinely produce ^{99m}Tc for use in nuclear medicine. The affinity of the $^{99}MoO_4^{2-}$ ion to acidified alumina is much stronger than $^{99m}TcO_4^-$, and the latter is readily eluted from the generator with sterile saline solution while the former remains bound to the column (**Figure 9**).

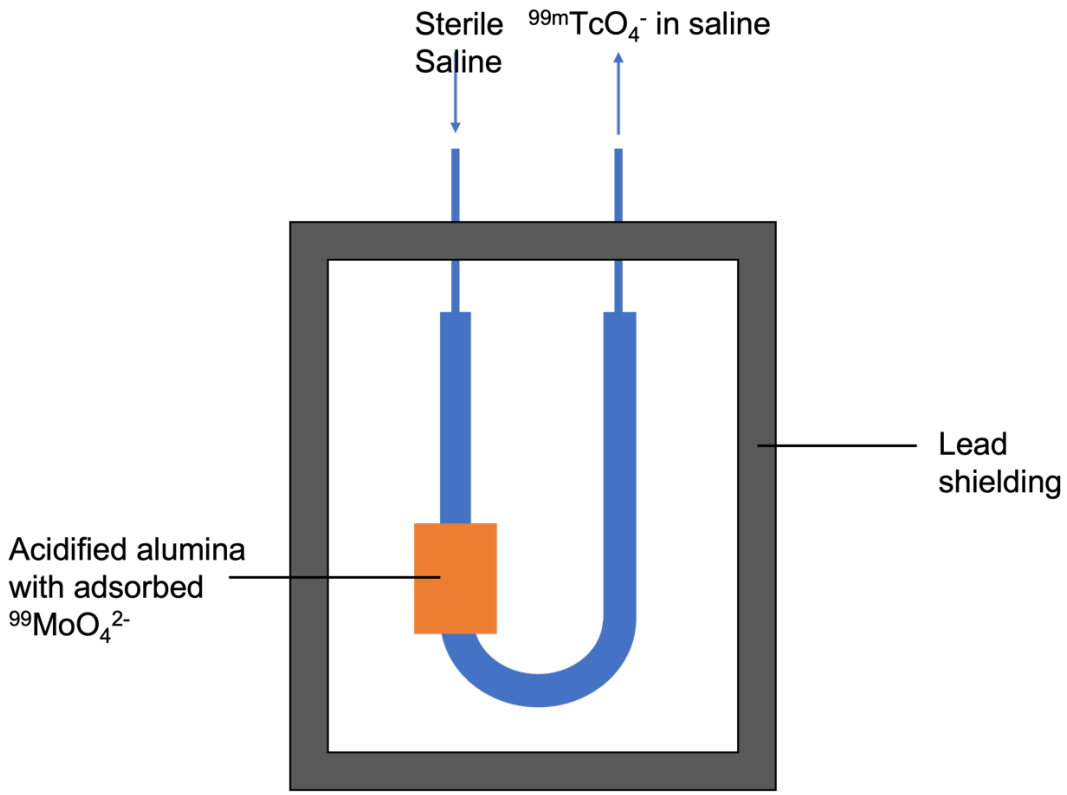

Figure 9: Schematic of a $^{99}Mo/^{99m}Tc$ adsorption generator.

Liquid-liquid extraction is predicated on the relative hydrophobicity of the components in a mixture to achieve separation. It involves two different immiscible liquids, usually water (polar) and an organic solvent (non-polar). The components of the mixture must have differences in solubility in the two liquids, and when vigorously shaken, the two liquids come into contact with one another to allow the components to disperse into the corresponding layer in which they have the highest solubility. An example of this technique is the use of methyl ethyl ketone for the effective extraction of ^{99m}Tc from ^{99}Mo in a $^{99}Mo/^{99m}Tc$ extraction generator under basic conditions (**Figure 10**) [39].

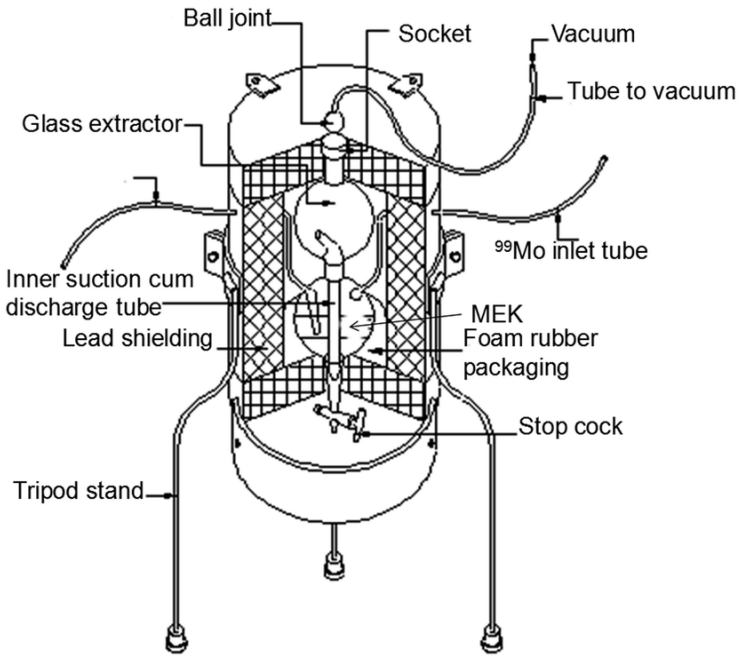

Figure 10: Schematic of a $^{99}Mo/^{99m}Tc$ extraction generator [40].

Extraction chromatography is a very attractive separation method that combines the selectivity of liquid-liquid extraction with the ease of operation of column-based separation methods. The continued advances in the development of highly specific ligands capable of forming strong, selective complexes with metal ions promise to broaden the scope of the technique.

1.8 Objectives of Dissertation

This dissertation involves radionuclide production and separation methods, and the reformulation and characterization of radiolabeled microparticles.

Chapter 2 covers the production of high specific activity (HSA) ^{186}Re from the irradiation of pressed, graphite-sandwiched $^{186}WS_2$ targets by way of the $^{186}W(p,n)^{186}Re$ reaction in a

~16.5 MeV medical cyclotron. A new, all metal target capsule was designed with the goal of improving the thermal efficiency of the target during irradiation compared to the previous design. A recycling method was also evaluated to recover the costly enriched target material from decayed irradiated targets.

Chapter 3 covers the production of HSA ^{186}Re from irradiation of ^{186}W metal targets via the ^{186}W(d,2n)^{186}Re reaction at the University of Washington Cyclotron Facility. Several separation methods were also evaluated and compared for their efficiency for the isolation of Re, and recovery of W.

Chapter 4 covers the characterization and reformulation of a novel ^{90}Y-based liquid brachytherapy agent for the treatment of solid tumors. Quality control (QC) methods were developed for the reformulated drug and biodistribution and therapy studies were performed in tumor bearing mice.

Chapter 5 summarizes the findings of the preceding chapters and discusses the future of the projects.

Chapter 2

Production of High Specific Activity ^{186}Re via the ^{186}W(p,n)^{186}Re Reaction in a PETtrace Cyclotron

Part of this work is reprinted (adapted) with permission from {Anster Charles, Firouzeh Najafi Khosrashahi, Li Ma, Chathurya Munindradasa, Rebecca Hoerres, John D. Lydon, Steven P. Kelley, James Guthrie, David Rotsch, Dmitri Medvedev, Cathy S. Cutler, Yawen Li, D. Scott Wilbur, Heather M. Hennkens, Silvia S. Jurisson. Evaluation of $^{186}WS_2$ target material for production of high specific activity ^{186}Re via proton irradiation: Separation, radiolabeling and recovery/recycling. Radiochim. Acta. Published January 2022.

2.1 Introduction

Rhenium-186 ($t_{1/2}$ = 90.64 h, E_{β^-} = 359 keV (71%), 306 keV (22%)) is a very promising therapeutic radionuclide, which decays via the emission of β^- particles with energies of 1.07 MeV (71%) and 0.93 MeV (22%) resulting in a targeted tissue range of 3.6 mm [41]. Like ^{188}Re, another rhenium radioisotope of particular interest, the potential value of ^{186}Re is strengthened by its gamma photon (E_γ = 137 keV (9%)), which may be used concurrently for Single Photon Emission Computed Tomography (SPECT) imaging for theragnostic applications, [42]. Furthermore, the similar coordination chemistry of rhenium and technetium can be exploited for targeted radiopharmaceutical development. The excellent properties of ^{99m}Tc ($t_{1/2}$ = 6.01 h, E_γ = 141 keV (89%)) have allowed the

radionuclide to retain its importance to nuclear medicine by accounting for 80% of nuclear imaging procedures globally despite its recent supply and demand issues and the emergence of Positron Emission Tomography (PET) [43]. Due to the lanthanide contraction, rhenium has an ionic radius similar of technetium, often leading to isostructural rhenium and technetium complexes [44]. Collectively, these favorable features of ^{186}Re serve as a premise for the development of therapeutic analogues to diagnostic radiopharmaceuticals based on ^{99m}Tc.

Rhenium-186 is routinely produced in a nuclear reactor via the ^{185}Re(n,γ)^{186}Re reaction, but the low specific activity of the produced ^{186}Re renders it unfeasible for radioimmunotherapy applications [45–47]. Alternative routes to ^{186}Re production include proton (^{186}W(p,n)^{186}Re) and deuteron (^{186}W(d,2n)^{186}Re) reactions on enriched ^{186}W at accelerators, which would generate high specific activity (HSA) ^{186}Re [48–52]. Tungsten metal is hard and brittle, and thus enriched ^{186}W is not available as a foil and the metal powder does not press well [53]. Tungsten disulfide has material and physical properties suitable for pressed targets as it forms two dimensional sheets as does graphene, and thus its industrial use as a lubricant, among other applications [54–56]. This property led to the evaluation of tungsten disulfide as an alternative to W metal powder as a target material for irradiation with protons and deuterons at accelerators [53]. Thick $^{186}WS_2$ pressed targets may allow production of ^{186}Re with the higher specific activity required for immunotherapy via the ^{186}W(p,n)^{186}Re reaction using incident beams of 11 MeV [53]. A 2015 study of the global network of cyclotrons approximated that 1050 small medical cyclotrons (<16 MeV p^+) were in routine use at hospitals,

universities, and commercial plants, all of which have the required proton energy to enable routine ^{186}Re production at the research scale [57].

In this investigation, an aluminum target capsule was designed and fabricated to allow production of HSA ^{186}Re on a PETtrace medical cyclotron using graphite-sandwiched pressed $^{186}WS_2$ targets. Various proton beam currents and durations were evaluated to determine the maximum achievable irradiation parameters before target failure occurs. Following irradiation, the targets undergo dissolution, separation, and recovery of ^{186}Re and ^{186}W, followed by ^{186}Re radiolabeling with a newly designed ligand, namely 222-monoaminemonoamide (MAMA)-*N*-propionate. Additional radiolabeling to generate the tricarbonyl core, $[^{186}Re][Re(CO)_3(OH_2)_3]^+$, was successful. A recovery and recycling method for highly enriched $^{186}WS_2$ to increase the efficiency and cost effectiveness of the process was also evaluated.

2.2 Experimental

2.2.1 Materials and Methods

Natural WS_2 was purchased from Sigma Aldrich. Enriched $^{186}WO_3$ (99.82%) was purchased from Isoflex USA (San Francisco, CA). All solvents and reagent grade acids and bases were purchased from Fisher Scientific or Sigma-Aldrich and used without further purification. Only 18 MΩ water was used during the experiments.

2.2.2 Physical Measurements

Reversed phase HPLC (RP-HPLC) was performed using a Shimadzu Prominence HPLC system equipped with a pump, controller, a Prominence UV-Vis detector (model SPD20-AV) and Phenomenex Jupiter C18 (5 μm, 150 mm x 4.6 mm) column. An ORTEC HPGe detector equipped with Genie multichannel analysis software was used to evaluate ^{186}Re liquid samples. X-ray powder diffraction (XRD) measurements were collected on a Bruker Prospector CCD diffractometer (Incoatec IμS micro-focus Cu source, λ = 1.54178 Å, 45 kV, 0.65 mA) with the samples in polyamide capillary tubes, and data were processed with DIFFRAC software. Inductively-coupled plasma mass spectrometry (ICP-MS) analyses for sample purity and isotopic abundance of ^{186}W were made using a PerkinElmer NexION 300X ICP-MS run in KED mode at a He flow rate of 2 mL/min.

2.2.3 Target preparation and irradiation

2.2.3.1 Design of target capsule

A CAD designed Aluminum 6061 target capsule (Ø = 19.040 mm) comprised of a base and a lid were machined within tolerances of 0.025 mm. A bore (Ø = 13.020 mm) was centered on the circular base along with a 0.990 mm wide circular groove (Ø = 15.494 mm). The lids were machined to a thickness of 0.500 mm to degrade 16.5 MeV protons to 11.6 MeV and a 0.990 mm wide circular ridge (Ø = 15.494 mm) allowed the lid to be fastened onto the base (**Figure 11**). Small suction cups were used to open the target capsule following bombardment.

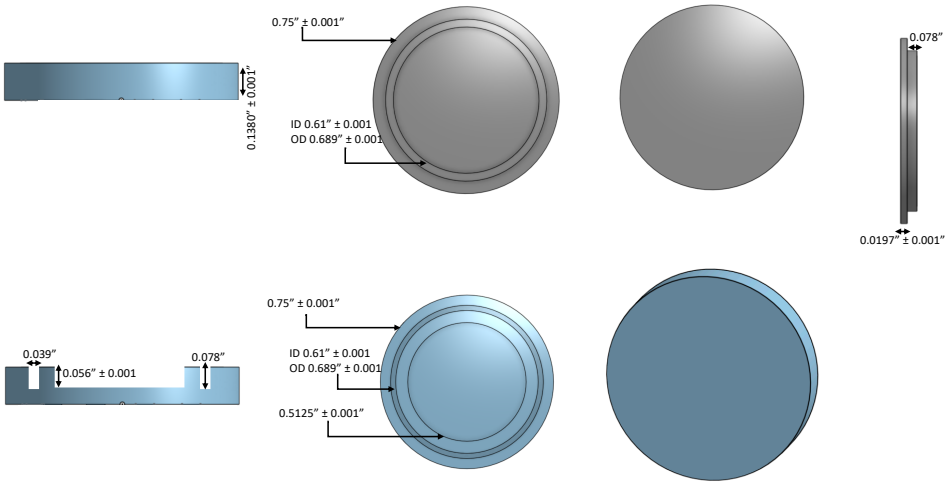

Figure 11: CAD designed aluminum target capsule

2.2.3.2 Synthesis of $^{186}WS_2$

Enriched $^{186}WO_3$ powder (99.9% enrichment; Isoflex) was converted into $^{186}WS_2$ by heating at 900 °C in a porcelain crucible in a tube furnace in an atmosphere of argon/hydrogen (5:1) for 1 h, followed by 1 h in an atmosphere of H_2S (>99.5%, Sigma Aldrich) at 900 °C (**Figure 12**). X-ray powder diffraction (XRD) and inductively coupled plasma mass spectrometry (ICP-MS) were employed for characterization of the synthesized $^{186}WS_2$.

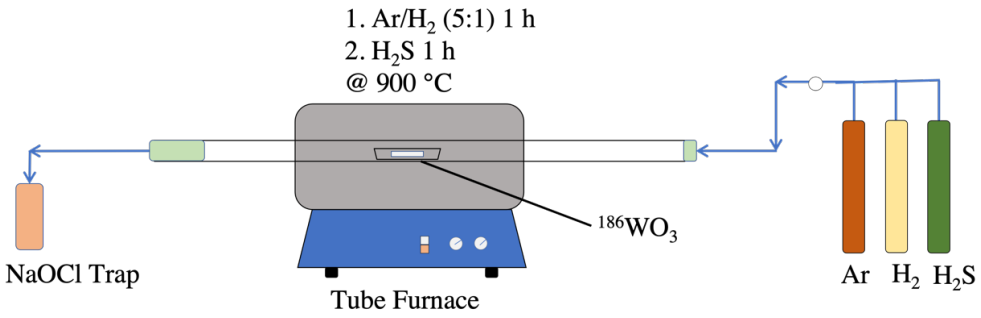

Figure 12: Synthesis of $^{186}WS_2$ in a tube furnace

2.2.3.3 Preparation of $^{nat}WS_2$ and $^{186}WS_2$ targets

Natural and enriched WS_2 targets (~189 mg) were uniaxially pressed between two layers of graphite flakes (~310 mg below and ~22 mg above) to increase the target stability for 30 seconds with 13.8 MPa of hydraulic pressure using a Dake B-10 model manual utility hydraulic bench press. The Stopping and Range of Ions in Matter (SRIM-2013) software was used to determine the quantity of material required to degrade the beam from 10.8 to 7.6 MeV within the WS_2 layer, maximize ^{186}Re production and minimize other Re isotope production, and achieve full beam stoppage in the bottom graphite layer (**Figure 13**).

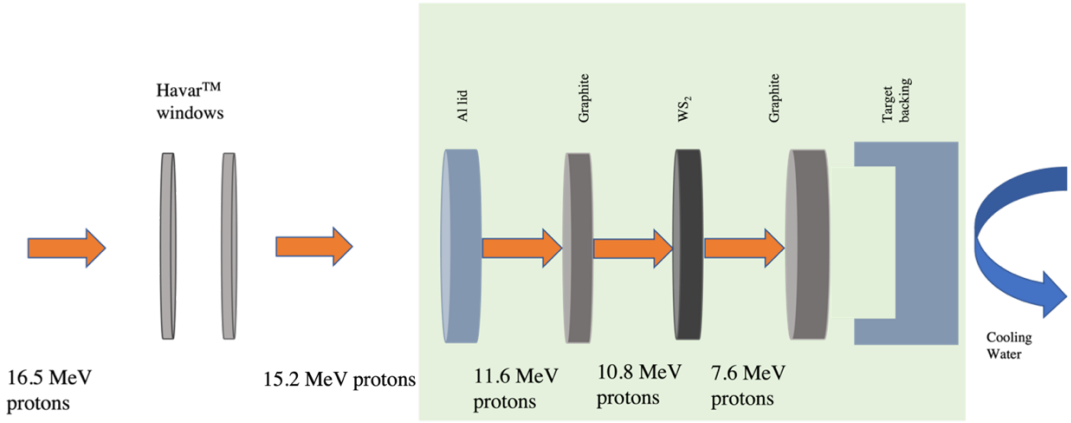

Figure 13: Solid target design. Green area represents target capsule

2.2.3.4 Irradiation of $^{nat}WS_2$ targets

Caution! Proton irradiation of W targets yields Re and W radioisotopes, which were handled only by trained personnel in laboratories approved for work with radioactive materials. Graphite encased $^{nat}WS_2$ targets were bombarded with 16.5 MeV protons on a General Electric (GE) PETtrace 860 cyclotron at 20 μA, 30 μA, 40 μA, and 50 μA for 15

minutes to determine whether the target could withstand these currents without target failure. A COMSOL Multiphysics 5.1 conjugate heat transfer model was designed to predict the maximum temperature reached in the target during irradiation. A second $^{nat}WS_2$ was bombarded with a 16.5 MeV proton beam for 2 h at 20 μA to determine the yield of ^{186}Re at end of bombardment, followed by target dissolution and separation of ^{186}Re using a liquid-liquid extraction method detailed below.

2.2.3.5 Production of HSA ^{186}Re via the $^{186}W(p,n)^{186}Re$ nuclear reaction

Following the evaluation of the natural targets, enriched $^{186}WS_2$ targets were bombarded with 16.5 MeV proton beams on a GE PETtrace 860 cyclotron for 2 h and 4 h at 20 μA.

2.2.4 Target dissolution and isolation of ^{186}Re

After a decay period of around 16 h, the irradiated targets were opened using two suction cups, transferred to a beaker, and the top graphite layer was vigorously scraped off using a Teflon spatula. Hydrogen peroxide (30%, 8 mL) was added in 1-3 mL aliquots and heated to 35 °C to dissolve the target. The temperature was then raised to 80 °C to decompose any remaining H_2O_2, followed by cooling to room temperature, and filtering through a 0.2-mm filter. Water was added to the target solution to increase the volume to ~10 mL, NaOH (2 M, 1 mL) was added to adjust the pH to 14, and then NaCl (1 g) was added to the solution prior to transfer to a separatory funnel. Methyl ethyl ketone (10 mL; MEK) was added to the separatory funnel, followed by gentle mixing. The phases were allowed to separate and then the aqueous and MEK fractions were collected separately.

The MEK fraction was evaporated to near dryness by heating at 50 °C with air flow and the [^{186}Re]-perrhenate was reconstituted with 0.75 mL of 0.15 M saline solution. The [^{186}Re]-perrhenate was further purified on a 0.15 M NaCl conditioned acidified alumina column (0.5 mL bed volume, 0.49 g). HPGe spectra were obtained before and after MEK extraction to evaluate the purification process (**Figures S1** and **S2**).

2.2.5 Radiolabeling Studies

The following is a summary of the radiolabeling studies performed by Li Ma, Chathurya Munindradasa, and Rebecca Hoerres with two Re-complexes as QC methods for HSA ^{186}Re.

2.2.5.1 Deprotection of trityl-protected 222-MAMA-*N*-ethylpropionate

Trityl protected 222-MAMA ligand synthesized by Firouzeh Najafi Khosrashahi was deprotected with trifluoroacetic acid (95% TFA) and triethyl silane (5% TES) according to the method described in reference [58] before radiolabeling.

2.2.5.2 Synthesis of [^{186}Re]Re(V)-glucoheptonate ([^{186}Re]Re-GH)

An intermediate compound, ^{186}Re]Re(V)-glucoheptonate, was synthesized by reducing [^{186}Re]ReO_4^- with $SnCl_2$ and sodium glucoheptonate according to a method described in reference [58].

2.2.5.3 Synthesis of [^{186}Re]ReO(222-MAMA-*N*-ethylpropionate)

Radiolabeling of 222-MAMA-*N*-ethylpropionate with ^{186}Re was achieved by adding [^{186}Re]Re-GH to the deprotected ligand in **2.6.2** under conditions described in reference [58]. The radiochemical yield was determined by radio-HPLC.

2.2.5.4 Synthesis of [^{186}Re][$Re(CO)_3(OH_2)_3$]$^+$

[^{186}Re][$Re(CO)_3(OH_2)_3$]$^+$ was synthesized according to a method described in reference [58] by reducing ReO_4^- with carbon monoxide. The radiochemical yield was determined by radio-HPLC

2.2.6 Recovery of ^{186}W and recycling of $^{186}WS_2$

The aqueous fraction from the liquid-liquid extraction containing ^{186}W in the form of [$^{186}WO_4$]$^{2-}$ was converted into tungstic acid ([^{186}W]H_2WO_4) by precipitation with concentrated HCl (2 mL). The resulting suspension was centrifuged for 20 minutes, followed by decanting the supernatant, adding H_2O (10 mL) to the pellet, and then vortexing to resuspend the [^{186}W]H_2WO_4. The rinse-centrifuge cycle was repeated 9 more times with acetone replacing deionized water in the final rinse; the pellet was left to air dry overnight. Conversion of the dried [^{186}W]H_2WO_4 to $^{186}WO_3$ was achieved by heating in air in a tube furnace at 525 °C for 3 h. Finally, $^{186}WS_2$ was synthesized by heating the $^{186}WO_3$ at 900 °C in a porcelain crucible in a tube furnace in an atmosphere of argon/hydrogen (5:1) for 1 h, followed by 1 h in an atmosphere of H_2S at 900 °C. XRD and ICP-MS were used for characterization of the synthesized $^{186}WO_3$ and $^{186}WS_2$.

2.3 Results and Discussion

Rhenium-186 is an excellent therapeutic match for ^{99m}Tc. A routine source of HSA ^{186}Re would be beneficial for targeted radiotherapy applications, especially when limited numbers of receptors are present. Several reports on accelerator production of ^{186}Re from enriched ^{186}W targets with protons and deuterons have been published [47–53]. Proton irradiation is optimal at the highest cross section of ~10 MeV, which can be achieved at most medical cyclotrons although increased yields may be achieved at higher incident energies with the use of thicker targets. A remaining issue is the target form for tungsten [49, 50, 59, 60]. Enriched ^{186}W is only available as the metal powder or $^{186}WO_3$. The powder form does not press well and is very brittle and hard. While the metal powder has been sandwiched between graphite layers and annealed for irradiation [52], tungsten trioxide has poor thermal properties [53]. Thus, we have developed WS_2 as a potential target material; it presses well, and its 53 $Wm^{-1}K^{-1}$ thermal conductivity is higher than that of WO_3 (1.63 $Wm^{-1}K^{-1}$).

Our previous studies have shown that pressed WS_2 targets offer significant advantages over pressed W metal targets and electrodeposited W targets for production of ^{186}Re via proton bombardment, due to the reduction in cost of the required target preparation equipment, increase in physical target stability, and ease of regenerating WS_2 for reuse [53]. A graphite sandwiched WS_2 design was implemented to further improve the target stability under proton bombardment at higher beam currents and durations [53].

2.3.1 $^{186}WS_2$ synthesis and characterization

The commercially available chemical forms of enriched ^{186}W are the metal powder and $^{186}WO_3$. Several routes of synthesizing WS_2 are reported, but only those starting with $^{186}WO_3$ and using the minimal number of reagents to minimize contamination were considered for preparing enriched $^{186}WS_2$. The dominant literature preparation of WS_2 from WO_3 uses a sulfide source (generally, H_2S, $(NH_4)_2S$ or thiourea) by first reducing WO_3 to "blue tungsten" and then reacting with a sulfide source at high temperature under an inert atmosphere. Elemental sulfur can also be reacted with either W metal or WO_3, however, generally other reagents are also involved. $^{186}WS_2$ was successfully synthesized from $^{186}WO_3$ in about 99% yield using $H_2S(g)$ as the sulfide source. The synthesized $^{186}WS_2$ is a dark gray powder that is very distinct from the yellow $^{186}WO_3$ powder, and the characteristic $^{186}WS_2$ XRD peaks at 14.2°, 33.5°, 58.5°, and 60.5° confirmed the formation of the product (**Figure 14**). The absence of the 23.3° peak, which is characteristic of $^{186}WO_3$ powder, also confirmed that complete conversion to $^{186}WS_2$ was accomplished.

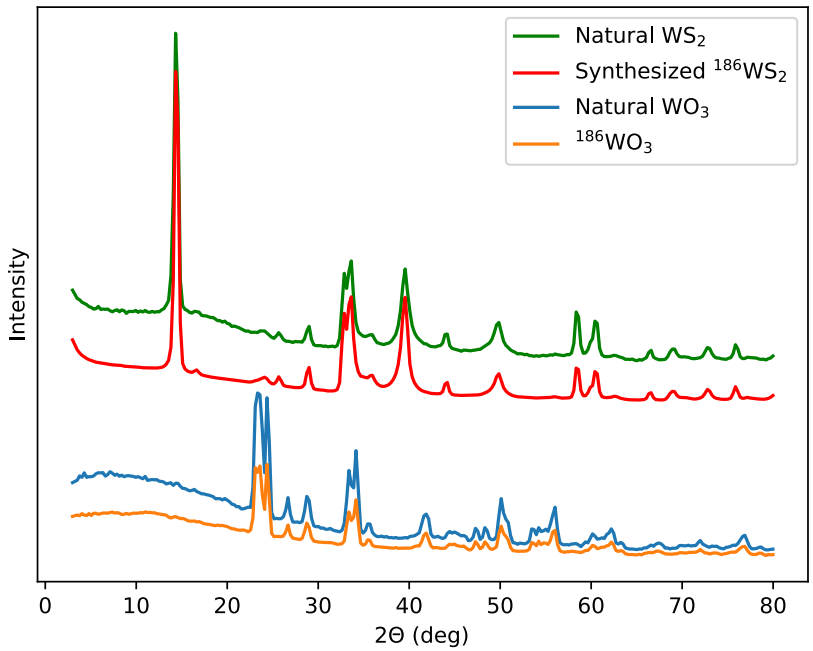

Figure 14. XRD of purchased $^{nat}WO_3$, $^{186}WO_3$, $^{nat}WS_2$ and synthesized $^{186}WS_2$ powders

2.3.2 Target preparation

Uniaxial pressing of graphite flakes and $^{186}WS_2$ with a 13 mm diameter die at high pressure into machined aluminum 6061 target capsules (**Figure 15**) resulted in physically compact, robust targets that were resistant to mild scraping with a spatula. The 0.5 mm thick aluminum lid that was fastened atop the target was designed to degrade 16.5 MeV protons to 11.6 MeV by SRIM-2013 predictions (**Figures 16 and 17**).

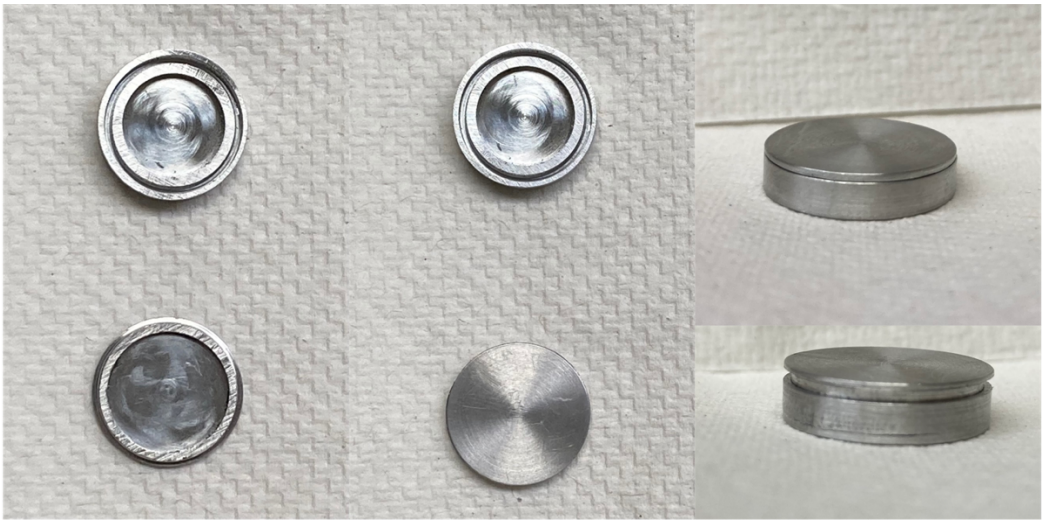

Figure 15. Machined aluminum 6061 target capsules

The densities of pressed graphite flakes and tungsten disulfide were determined by measuring the thickness of individually pressed layers with a micrometer and solving for the density (ρ) using **Equation 6**,

$$\rho = \frac{m}{\pi \cdot r^2 \cdot h} \qquad \textbf{Equation 6}$$

where m = mass, h = measured thickness of the layer, and r = radius of the target**.** The required mass for each of the layers that corresponded with incident and exit beam energies of ~10.8 and 7.6 MeV, respectively, in the $^{186}WS_2$ layer, and full beam stoppage in the lower graphite layer were used to prepare targets for irradiation with a $^{186}WS_2$ area density of 142 mg/cm^2.

2.3.3 Target irradiations

Pressed $^{nat}WS_2$ targets were irradiated at various beam currents for 15 min with 10.8 MeV protons, which had been degraded from 16.5 MeV to 11.6 MeV by the Al lid and to 10.8

MeV by the first graphite layer, to determine the maximum practical current for the $^{nat}WS_2$ targets on the GE PETtrace cyclotron (**Figure 16**).

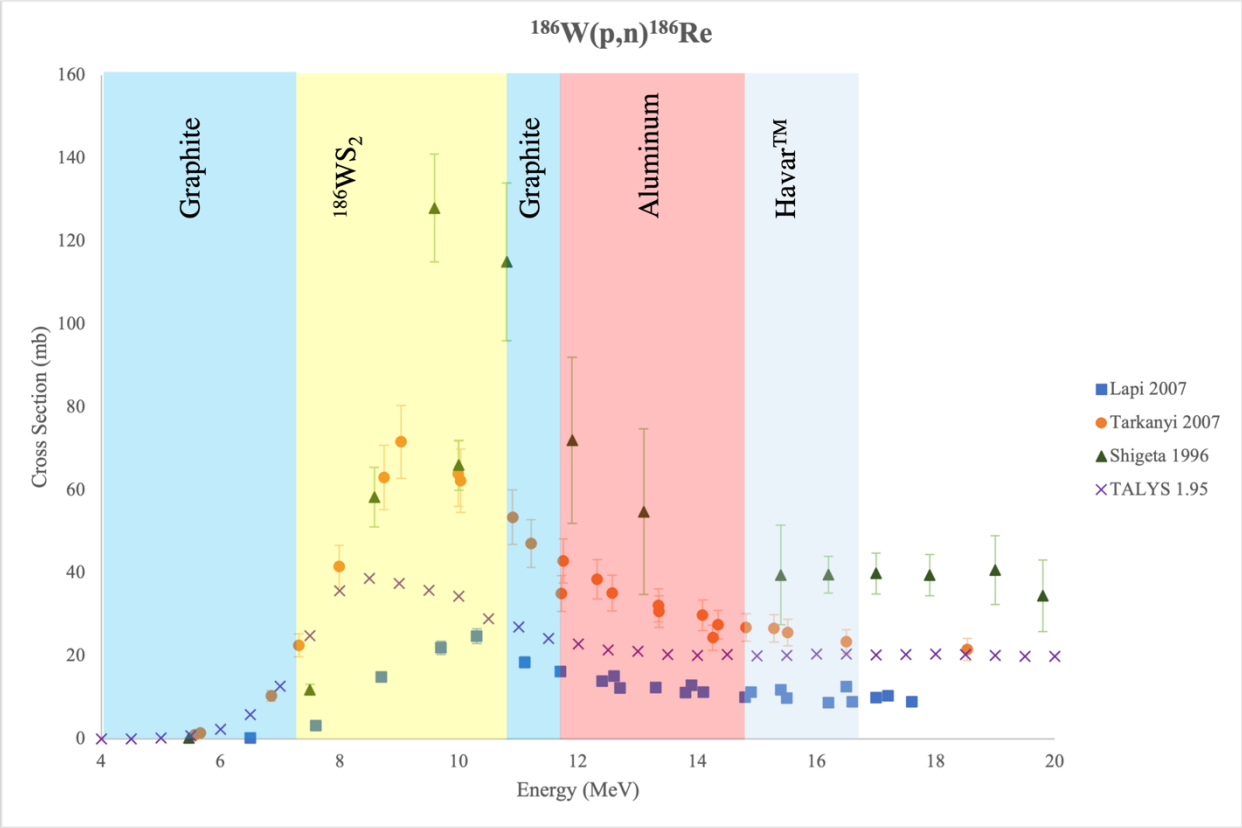

Figure 16. Combination of proton beam energy degradation data from SRIM and $^{186}W(p,n)^{186}Re$ excitation functions in the target layers

The utilization of an incident energy of 10.8 MeV within the $^{186}WS_2$ layer also mitigates the production of other Re radionuclidic impurities by way of competing nuclear reactions. Although the fractional isotopic abundance of other W isotopes in the target is low, an increase in the rate of production of multiple Re species such as ^{182}Re and ^{183}Re would be observed if opting for a higher incident energy (**Figure 17, Table 2**).

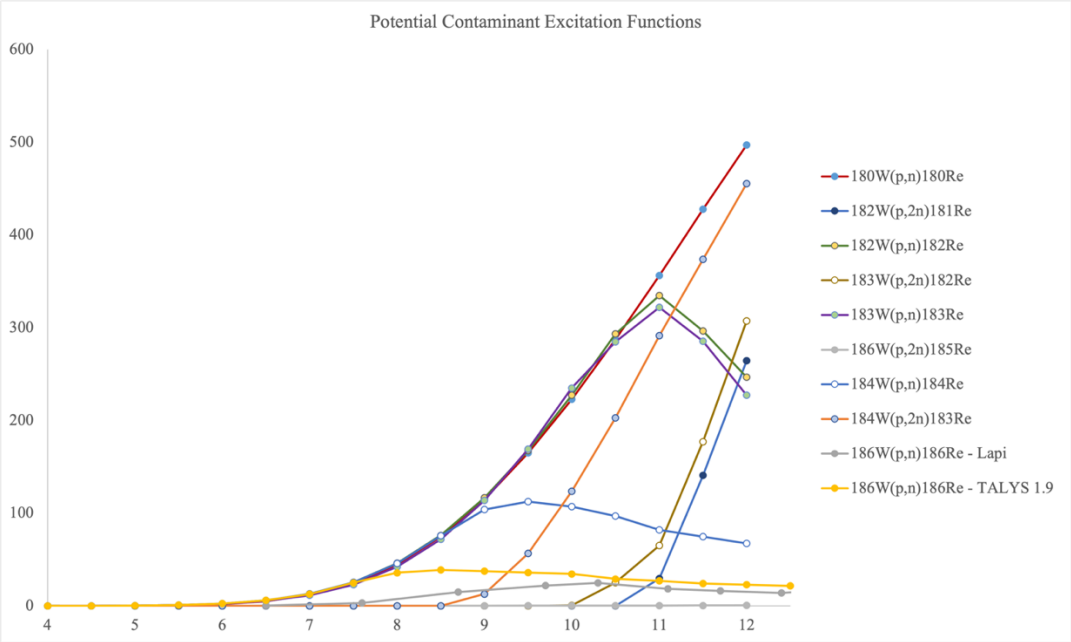

Figure 17. Predicted excitation functions of co-produced Re nuclides

Table 2. Summary of estimated contaminant Re nuclides at EOB using Talys 1.9 code, experimental activity determined by HPGe, and production yield

Contaminant	**Nuclear Reaction**	**Incident Energy (MeV)**	**Estimated Yield**
^{182}Re	^{182}W(p,n)^{182}Re	10.8	0.3 MBq (7 μCi)
	^{182}W(p,n)^{182}Re	14	0.71 MBq (19 μCi)
	^{183}W(p,2n)^{182}Re	10.8	0.0069 MBq (0.2 μCi)
	^{183}W(p,2n)^{182}Re	14	0.48 MBq (13 μCi)
^{183}Re	^{183}W(p,n)^{183}Re	10.8	0.0068 MBq (0.2 μCi)
	^{183}W(p,n)^{183}Re	14	0.017 MBq (0.5 μCi)
	^{184}W(p,2n)^{183}Re	10.8	0.02 MBq (0.6 μCi)

	$^{184}W(p,2n)^{183}Re$	14	0.2 MBq (5.4 μCi)
^{184}Re	$^{184}W(p,n)^{184}Re$ $^{184}W(p,n)^{184}Re$	10.8 14	0.05 MBq (13.5 μCi) 0.1 MBq (27 μCi)

2.3.4 Experimental and computational thermal analysis

The targets were actively cooled at the back with 20 °C water during irradiations, and visual inspection of the aluminum lid for physical damage showed burn marks beginning to occur at 40 μA (**Figure 18**).

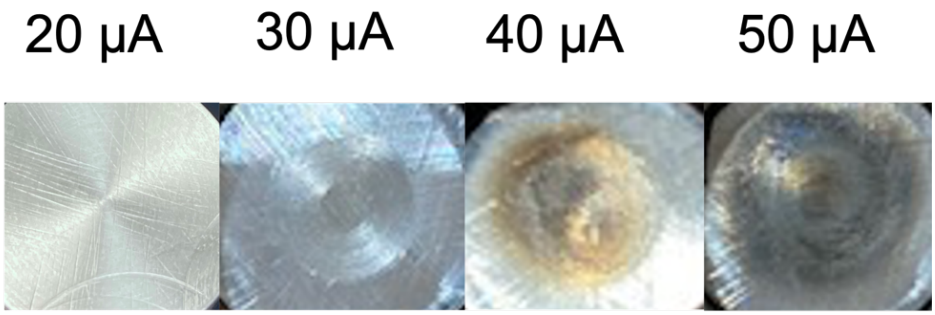

Figure 18. Photographs of targets irradiated with 20 μA, 30 μA, 40 μA and 50 μA proton beams showing extent of beam damage on the aluminum 6061 lid

A finite element analysis stationary study was used to model the maximum temperature in the target using COMSOL's conjugate heat transfer module, which combines all features from the Heat Transfer and Single-Phase Flow interfaces to describe heat transfer in solids and fluids and nonisothermal flow in fluids. A user defined mesh made of tetrahedra resulted in an acceptable average tetrahedral element quality for the study

(**Figures 19 and 20**). The boundary conditions for the study can be found in Supplemental Figures (**S1-S16**).

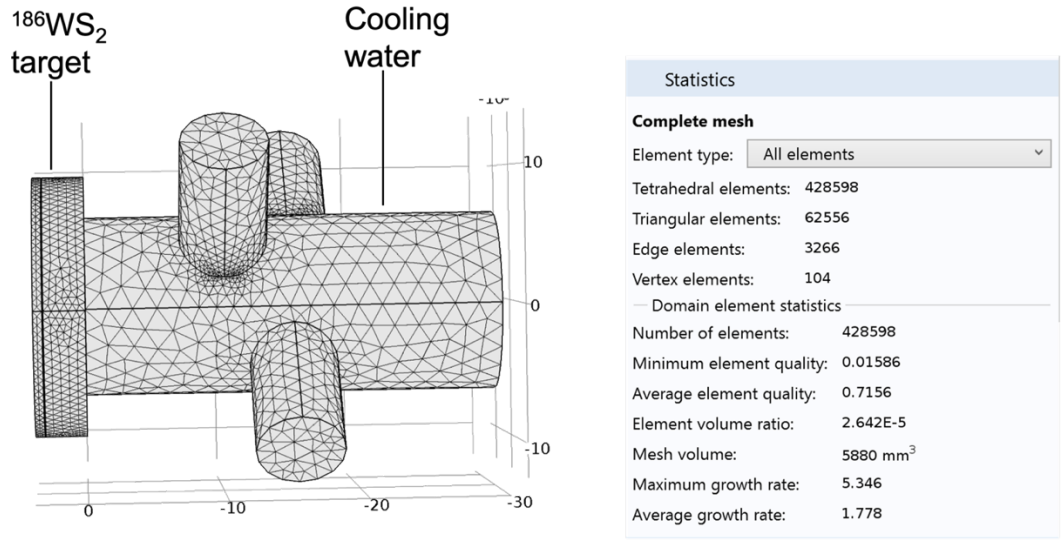

Figure 19. User-defined mesh for water cooled target used for thermal studies in COMSOL Multiphysics (left). Statistics of the generated mesh showing an average element quality of 0.72.

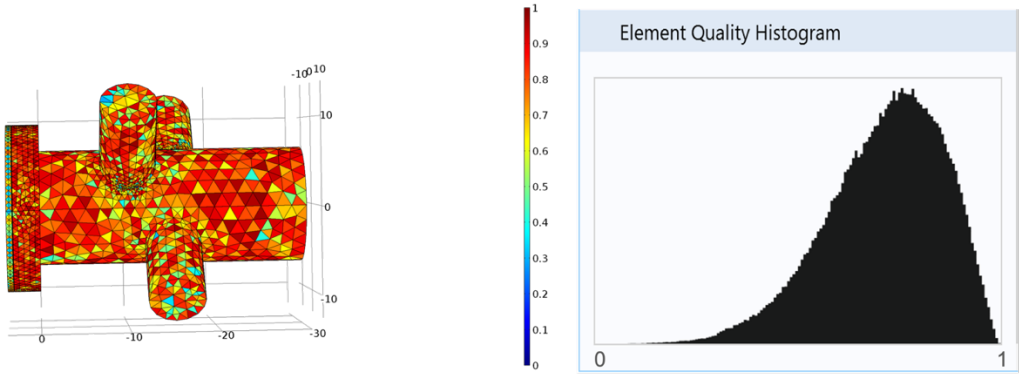

Figure 20. Mesh plot showing color coded quality analysis where red is high quality and blue is low quality (left). Element quality histogram showing quality of the mesh elements from 0 to 1 (right).

A maximum temperature of 652 °C was predicted in the aluminum lid at 50 μA, which is above the melting point range of aluminum 6061 (582-651 °C). The data summarized in **Table 3** and **Figures 21 and 22** suggest that beam currents should be kept below 40 μA for longer irradiations to maintain target integrity. Alternatively, eliminating the aluminum lid from the target design and degrading the beam to 11.59 MeV further upstream would significantly reduce the power deposition and heat in the target during irradiation to potentially allow for higher currents to increase ^{186}Re yield.

Table 3. Summary of predicted temperatures in the target calculated using COMSOL Multiphysics

Beam Current (μA)	**Power Deposited (W)**	**Predicted Temperature** (°C)
20	305	289
30	458	415
40	610	536
50	763	652

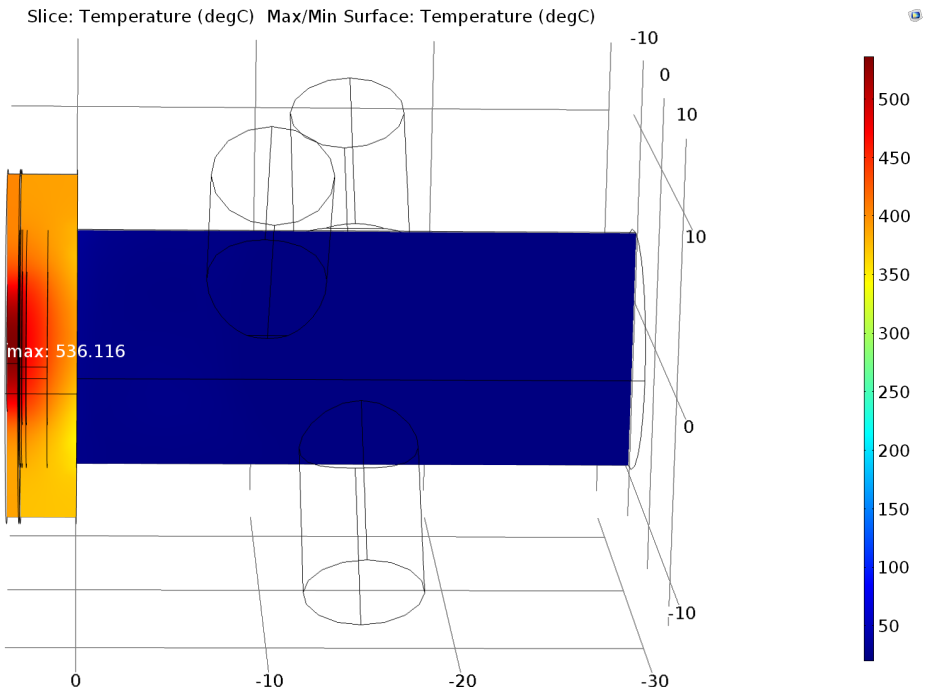

Figure 21. COMSOL predicted maximum temperature at 40 μA

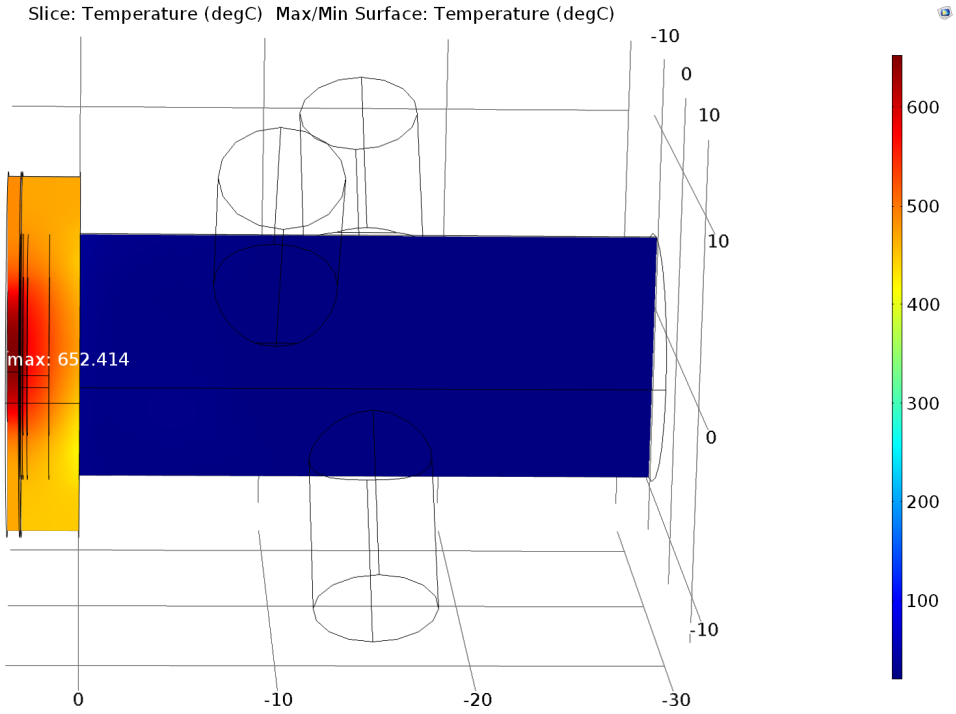

Figure 22. COMSOL predicted maximum temperature at 50 μA

2.3.5 ^{186}Re production

Longer irradiations of $^{nat}WS_2$ and $^{186}WS_2$ targets were performed with 16.5 MeV protons at 20 μA for 2 and 4 h to evaluate target integrity, experimental ^{186}Re production yields, a separation procedure, and radiolabeling efficiency of the isolated ^{186}Re. Theoretical yield estimates for a target proton entrance energy of 10.8 MeV and exit energy of 7.6 MeV calculated using Talys 1.9 and the IAEA Medical Isotope Browser tended to over-estimate the EOB yield of ^{186}Re by up to 50%. The use of a 99.9% enriched target resulted in an increased production rate of 3.5-fold higher than the natural target (**Table 4**). However, the 0.87 MBq $mA^{-1}h^{-1}$ production yield obtained from the 4 h irradiation was in good agreement with a theoretical estimate of 1.11 MBq $mA^{-1}h^{-1}$ obtained using cross section data from Hussain et al [61]. A comparison of the new aluminum target capsule and the old design at the same irradiation parameters revealed less physical damage to the new design (**Figure 23**). This may be due to the increased thermal efficiency of the new design achieved by the elimination of the adhesive. Inconsistencies in the ^{186}Re yields across the multiple runs may have been due to uncontrollable beam parameters of the non-optimized design of the solid target, and an unsteady support leg. A new solid target station was recently obtained from the University of Wisconsin which was designed to improve on the inconsistencies of the current design.

Table 4. Summary of estimated ^{186}Re activity at EOB using Talys 1.9 code, experimental activity determined by HPGe, and production yield

Sample	**^{186}W %**	**Current (μA)**	**Time (h)**	**Estimated Activity at EOB, MBq (μCi)**	**Activity at EOB, MBq (μCi)**	**Production Yield, MBq μA^{-1} h^{-1} (mCi μA^{-1} h^{-1})**
$^{nat}WS_2$	21.08	20	2	7.96 (215)	3.85 (104)	0.10 (2.60)
$^{186}WS_2$	99.82	20	2	37.37 (1009)	13.54 (366)	0.34 (9.15)
$^{186}WS_2$	99.82	20	4	74.7 (2019)	69.2 (1870)	0.87 (23.4)

Figure 23: Left, photograph of previous aluminum capsule design after a 2 h irradiation at 20 μA. Right, photograph of new aluminum capsule design after a 2 h irradiation at 20 μA

2.3.6 Target dissolution and separation

Dissolution of the target was achieved after ~1 h of gentle heating in 30% H_2O_2 approximately 12 hours after EOB. MEK extraction of ^{186}Re in the form of [^{186}Re][Na_2ReO_4] was achieved in high efficiency with multiple samples (**Table 5**, **Figures S17** and **S18**). Following evaporation of the MEK and reconstitution of the ^{186}Re in 0.15 M NaCl, a final purification step using an acidified alumina column (0.5 mL bed volume) further purified the product.

Table 5. Summary of ^{186}Re extraction and purification results

Sample	Irradiation Time at 20 mA (h)	MEK Extraction ^{186}Re Activity (%)	Alumina Column Purified Saline ^{186}Re Activity (%)	Purified ^{186}Re Activity MBq (μCi) after Alumina Column
$^{nat}WS_2$	2	93	91	2.66 (72)
$^{186}WS_2$	2	93	92	12.5 (338)
$^{186}WS_2$	4	92	83	51.4 (1390)

Analysis of a decayed aliquot by ICP-MS resulted in a specific activity of 28 Ci/mg for the isolated ^{186}Re and a total W content of 0.2 ppm. This represents a 9-fold increase over reactor-produced ^{186}Re via the ^{185}Re(n,γ)^{186}Re production route and is 74% of the theoretical specific activity at EOB [46].

The purchased $^{186}WO_3$ stock was analyzed by ICP-MS for comparison with the recovered ^{186}W and found to contain 13.1 mg of Re per g of $^{186}WO_3$, which resulted in 10.7 mg per g of $^{186}WS_2$ synthesized. This accounted for the lower-than-expected specific activity of the isolated ^{186}Re. Following irradiation and the MEK extraction procedure to separate the ^{186}Re, the ^{186}W recovered in the aqueous phase was analyzed for its purity;

the Re content was found to be below the detection limit of the ICP-MS instrument (**Table S19**).

The separation factor for this process was calculated based on the measured activities and ICP-MS results. The recovery of ^{186}W in the final ^{186}Re solution was determined to be 0.0072% (0.9 mg/12550 mg) and the recovery of the ^{186}Re was determined to be 83.03% (1390 mCi/1674 mCi). These values lead to a separation factor of $S_{Re,W}$ of 11,320 (83.03%/0.0072%).

2.3.7 Recovery of ^{186}W and recycling of $^{186}WS_2$

The ^{186}W remaining in the aqueous phase following MEK extraction of the $[^{186}Re][ReO_4]^-$ was recovered and recycled for re-use with the method we previously reported [53]. The ^{186}W from the extraction procedure was converted to tungstic acid, followed by conversion to tungsten trioxide in air at high temperature, and finally to tungsten disulfide in an H_2S atmosphere at high temperature. The total recovery of $[^{186}W]WS_2$ was 94%, with the majority of the unrecovered material lost during the rinse-centrifuge cycles on precipitation of tungstic acid. A ^{186}W enrichment assay of the recycled target by ICP-MS analysis was 99.79% compared to 99.83% originally in the purchased $^{186}WO_3$. Analysis by XRD confirmed the regeneration of $^{186}WS_2$ in high purity compared to previously synthesized $^{186}WS_2$ (**Figure 24**). This demonstrates that the recycling method can be reliably implemented for successive irradiations to ultimately mitigate the high initial cost of the target material. Additionally, the recovery and recycling removes the Re originally present in the enriched $^{186}WO_3$ purchased through the extraction process. The MEK extraction process could be performed before the synthesis of the $^{186}WS_2$ to remove

the Re present and yield a higher specific activity ^{186}Re in the first irradiation. Another 4 h irradiation at 30 μA was performed on the recycled material but a water leak in the cyclotron rendered the target unusable for further studies.

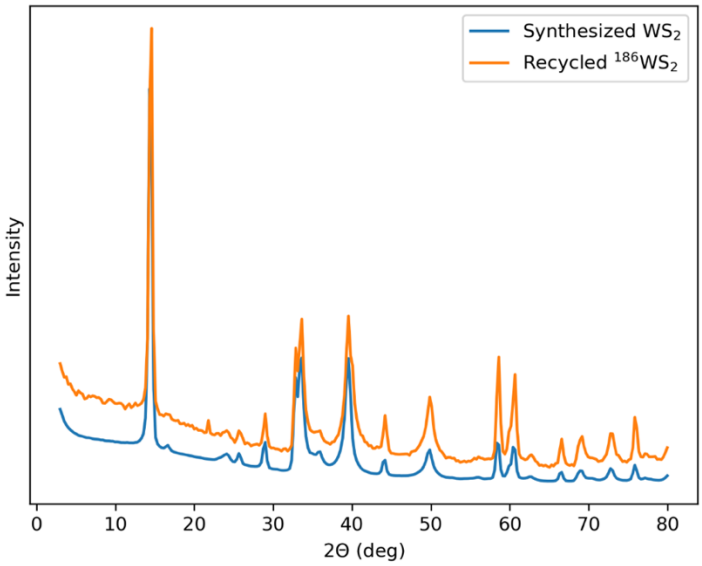

Figure 24. XRD of synthesized $^{186}WS_2$ powder and recycled $^{186}WS_2$ powder

2.4 Conclusions

High specific activity ^{186}Re was produced in good yield and purity on a GE PETtrace cyclotron via proton bombardment on an enriched $^{186}WS_2$ target material. $[^{186}Re][ReO_4]^-$ was isolated by MEK extraction with further purification through acidic alumina followed by radiolabeling with a new 222-MAMA-*N*-ethylpropionate ligand. The irradiated $^{186}WS_2$ target material was recovered from the aqueous phase of the MEK extraction and recycled in high yield and purity. Irradiation of recovered and recycled $^{186}WS_2$ would have a significantly higher specific activity of ^{186}Re since the Re present originally in the commercially purchased $^{186}WO_3$ was reduced below the detection limits

of the ICP-MS instrument during the recovery process. These results show the utility of the $^{186}WS_2$ target material for proton irradiation, and further studies (including re-irradiation after $^{186}WS_2$ recovery) are underway to evaluate higher current irradiations at longer times for maximum production using a re-designed solid target with increased reliability and cooling efficiency. Other future studies may include the irradiation of larger masses of $^{186}WS_2$ at the Brookhaven National Laboratory's Collider-Accelerator Department to obtain higher ^{186}Re yields for practical preclinical studies.

Chapter 3

Production of High Specific Activity (HSA) ^{186}Re via the ^{186}W(d,2n)^{186}Re Reaction and Evaluation of Separation Methods for No Carrier Added ^{186}Re from Deuteron Irradiated ^{186}W Targets

3.1 Introduction

Production of ^{186}Re via the ^{186}W(d,2n)^{186}Re reaction is a route that could potentially be exploited for acquiring HSA ^{186}Re for radioimmunotherapy purposes[62–64]. It may provide a viable alternative to reactor-produced low specific activity (LSA) ^{186}Re via the ^{185}Re (n,γ)^{186}Re reaction, which to date has only achieved a specific activity of ~3 Ci/mg [34, 46, 65]. Employing a particle accelerator to induce charged particle reactions on ^{186}W targets by way of the ^{186}W(p,n)^{186}Re and ^{186}W(d,2n)^{186}Re reactions produces HSA ^{186}Re from a different element, which can be chemically separated post-irradiation [52]. Previous studies have shown that deuteron bombardment of ^{186}W targets produces ^{186}Re yields that are at least three times higher than ^{186}Re produced from proton bombardment, requiring less target material [47, 52, 66]. In addition, the ^{186}Re produced by way of the ^{186}W(d,2n)^{186}Re also reportedly achieves higher specific activities compared to proton bombardment [51, 67].

Several methods for the chemical separation of radiorhenium from tungsten have been reported, including dry distillation, liquid-liquid extraction, anion exchange chromatography, and extraction chromatography [45, 49, 52, 60]. Due to the high cost of enriched ^{186}W target material, an effective method is required to isolate ^{186}Re from the

target solution and also maximize recovery yields for target recycling. Extraction of ^{186}Re into methyl ethyl ketone (MEK) is analogous to the extraction of ^{99m}Tc from ^{99}Mo in the ^{99}Mo/^{99m}Tc extraction generator and is a method of interest that offers high radiochemical purity and extraction yields of ^{186}Re in a time efficient fashion. Another promising method employs extraction chromatography via Analig Tc-02 and Re-02 resins (IBC Advanced Technologies), which utilize metal-selective molecular recognition technology. These resins have been demonstrated to effectively separate ^{186}Re from W while eluting ^{186}Re in H_2O [47, 52, 68].

3.2 Experimental

3.2.1 Materials and Methods.

Analig resins were purchased from IBC Advanced Technologies (Salt Lake City, UT). All solvents and reagent grade acids and bases were purchased from Fisher Scientific or Sigma-Aldrich and used without further purification. Only 18 MΩ water was used during the experiments. Reversed phase HPLC (RP-HPLC) was performed using a Hewlett Packard Series 1050 equipped with a pump, controller, a model 79853C UV/Vis detector and a Grace Alltima C18 (5 μm, 250 mm x 4.6 mm) column. An ORTEC HPGe detector equipped with Genie multichannel analysis software was used to evaluate ^{186}Re and ^{187}W liquid samples. Trityl-protected 222-MAMA-N-propionate (ethyl 6-((2-oxo-2((tritylthio)ethyl)amino)ethyl)(2-tritylthio)ethylamino)proprionate) was available from a previous study [58]. Low specific activity ^{186}Re was obtained from MURR. Tracer amounts of ^{187}W were prepared by neutron irradiation of natural ammonium

metatungstate (31 mg; $(NH_4)_6H_2W_{12}O_{40}\cdot xH_2O$; 99.99%; Sigma Aldrich) in the reflector region or pneumatic tube at MURR at a neutron flux of ~1 x 10^{13} n/cm^2/s for 15 min.

3.2.2 Preparation of ^{186}W Targets

Enriched ^{186}W metal powder (99.9%; 707 mg; Isoflex) was uniaxially pressed between two layers of graphite flakes (106 mg below and 56 mg above) for 30 seconds with 13.8 MPa of hydraulic pressure.

3.2.3 Production of HSA ^{186}Re via the ^{186}W(d,2n)^{186}Re Nuclear Reaction

The graphite encased target was bombarded with 22 MeV deuterons at the University of Washington Medical Cyclotron Facility's Scanditronix MC50 cyclotron for a total of 27 μAh, with an estimated incident deuteron energy of 19.5 MeV on the ^{186}W metal layer. A decay period of 4 days allowed co-produced ^{187}W to decay prior to processing.

3.2.4 Target Dissolution

The top graphite layer was removed with Teflon forceps and the irradiated target was transferred to a beaker. Hydrogen peroxide (30 %, H_2O_2, 32 mL) was then added in 1-3 mL aliquots and heated to 35°C to dissolve the target. The temperature was then raised to 80°C to decompose any remaining H_2O_2, allowed to cool to room temperature, and then filtered through glass wool to a final volume of 22.5 mL. The target solution was divided into two equal portions, one aliquot for a solvent extraction method and one aliquot for a column separation method for isolation of [^{186}Re]ReO_4.

3.2.5 Solvent Extraction Method

NaOH (5 M, 800 μL) was added to one aliquot of the target solution (11.25 mL) to adjust the pH to 14. The basic target solution was then transferred to a separatory funnel, and MEK (11.25 mL) was added, followed by gentle mixing. The aqueous and MEK fractions were collected separately, and each fraction was then back extracted. The MEK fraction was back-extracted with 10 mL of 1 M NaOH, and the aqueous fraction was back-extracted with 10 mL of MEK. Samples (2-10 μL) of the aqueous and MEK fractions were counted by HPGe gamma spectroscopy. The MEK was then evaporated using a Biotage V-10 evaporator and the Re-186 was reconstituted in 1 mL of 0.15 M saline solution.

3.2.6 Column Separation Method

Analig Tc-02 resin (350 mg) was dry packed into an empty column cartridge and conditioned with 10 mL of 1.5 M $(NH_4)_2CO_3$. $(NH_4)_2CO_3$ (3 M; 21.25 mL) was added to the second aliquot of target solution (11.25 mL), which was then loaded onto the column, and washed with 50 mL of 1.5 M $(NH_4)_2CO_3$. The $[^{186}Re]ReO_4^-$ was then eluted with two 3 mL aliquots of 80 °C water. All fractions were collected separately and counted by HPGe.

3.2.7 Deprotection of Trityl-protected 222-MAMA-N-propionate

222-MAMA-*N*-proprionate (26 mg; 80 μmol) was deprotected by reaction with trifluoroacetic acid (TFA; 2 mL; 26 mmol) and triethyl silane (TES; 1 μmol) at room temperature for 45 min. The TFA and TES were evaporated under argon gas at room

temperature. The dried residue was washed three times with hexane, and then dried under argon. The deprotected ligand (24 μmol) was stirred with tris(2-carboxyethyl) phosphine (TCEP; 2 mg, 7 μmol) and acetonitrile (1 mL) for 2 min to reduce any disulfide bonds that may have formed during solvent removal.

3.2.8 Synthesis of [^{186}Re]Re(V)-glucoheptonate

[^{186}Re]ReO_4^- (500 μL, 2.7 mCi) from the solvent extraction isolation method was added to a microcentrifuge tube containing a pre-mixed solution of 2 mg of $SnCl_2$ in 0.25 M HCl (20 μL) and 0.24 M sodium glucoheptonate solution (385 μL), and the reaction mixture was then heated at 40 °C for 40 min.

3.2.9 Radiolabeling of ^{186}Re with 222-MAMA-*N*-propionate

The [^{186}Re]Re(V)-glucoheptonate (100 μL) was added to a microcentrifuge tube containing the deprotected ligand (200 μL, 4 μmol), heated at 40 °C for 40 min, and assayed by radio-HPLC.

3.2.10 Optimization of the MEK Extraction Method of Rhenium

Tungsten target solution mimics of mass 350 and 700 mg were prepared by dissolving Na_2WO_4 (556 mg and 1112 mg) in de-ionized water (11.25 mL) and adjusted to pH 14 with 2 M NaOH (200 μL). Rhenium-186 and ^{187}W tracers (~10 μCi each) were then added to the solutions. To increase immiscibility between the aqueous and organic phases, NaCl (1 g) was added to the target solution prior to extraction. The target solutions were then transferred to a 25 mL separatory funnel, followed by liquid-liquid

extraction of $^{186}ReO_4^-$ with MEK (11.25 mL). A 10 mL aliquot of each phase was counted by HPGe. A second extraction was performed on the aqueous fraction using MEK (11.25 mL) and back extractions were performed on the MEK phases of the first and second extractions with pH 14 aqueous 2 M NaOH solution (11.25 mL) containing 1 g of dissolved NaCl. The two MEK phases were combined, evaporated to near dryness at 60 °C using nitrogen, and then reconstituted in 0.15 M NaCl (3 mL) prior to purification on a 0.15 M NaCl conditioned acidified alumina column (0.5 mL bed volume, 0.49 g).

3.2.11 Evaluation of Analig Tc-02 and Re-02 Resins for Separation of Re and W

Target solution mimics containing 350 or 700 mg of W were prepared by dissolving Na_2WO_4 (556 mg and 1112 mg) in 1.0 M NaOH or 1.5 M $(NH_4)_2CO_3$. Rhenium-186 and ^{187}W radiotracers (~10 μCi each) were added to the solutions. A Harvard Apparatus PHD 2000 syringe pump equipped with a 50 mL syringe and three-way Luer lock was used to draw up the target solution and pass it through 1 M NaOH or 1.5 M $(NH_4)_2CO_3$ preconditioned columns containing 350 mg of Analig Tc-02 or Re-02 resin at a rate of 1 mL/min (**Figure 25**). The columns were then washed with two successive volumes of 5 mL of 1 M NaOH or 1.5 M $(NH_4)_2CO_3$, followed by three successive elutions of ^{186}Re with 70 °C de-ionized water. All fractions were counted by HPGe.

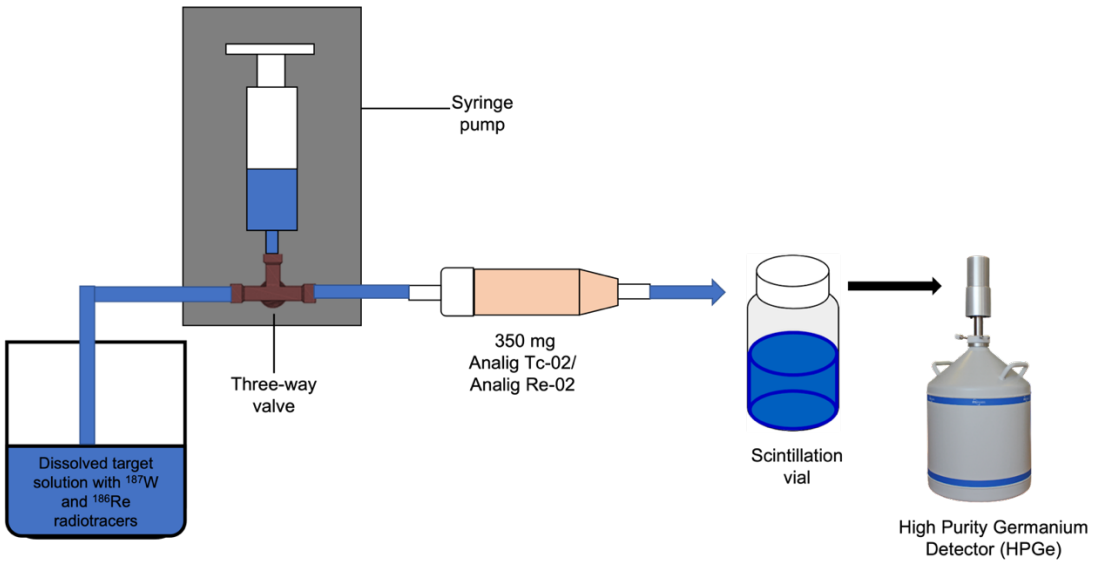

Figure 25: Experimental setup of semi-automated extraction chromatographic separation of Re from W using Analig resins

3.3 Results and Discussion

Previous studies performed at the University of Washington have shown that high specific activity ^{186}Re can be produced via the ^{186}W(d,2n)^{186}Re reaction using graphite-encased thick ^{186}W targets at higher production yields than the ^{186}W(p,n)^{186}Re reaction and with higher radionuclidic purity [52]. The objective of this study was to produce HSA ^{186}Re by way of the ^{186}W(d,2n)^{186}Re reaction and evaluate two separation methods for isolation of ^{186}Re from deuteron irradiated targets and recovery of ^{186}W. Further studies included additional separation methods that were evaluated with tungsten target solution mimics for their efficacy and efficiency.

3.3.1 Target preparation and deuteron bombardment

Enriched ^{186}W powder was pressed between two layers of graphite flakes to make a more robust target for deuteron irradiation [47]. The densities of uniaxially pressed graphite flakes and tungsten metal were determined by measuring the thickness of the individually pressed layers with a micrometer and solving for density (ρ) using **Equation 6**

$$\rho = \frac{m}{\pi \cdot r^2 \cdot h} \qquad \textbf{Equation 6}$$

where m = the mass of graphite or tungsten layer, r = the radius of the target holder and h = the thickness of the pressed layer. The Stopping and Range of Ions in Matter (SRIM-2013) was then used to determine the quantity of material needed for optimal production of ^{186}Re via ^{186}W(d,2n)^{186}Re and full beam stoppage in the bottom graphite layer [69]. The thickness of the top graphite layer (56 mg) was measured to be 0.18 mm and was estimated to degrade 22 MeV deuterons to 19 MeV before entering the ^{186}W layer. The ^{186}W layer (707 mg) had a thickness of 0.39 mm and an estimated deuteron beam exit of 6 MeV to maximize ^{186}Re yield before being fully stopped in the bottom graphite layer (106 mg), which was measured to be 0.32 mm (**Figures 26 and 27**).

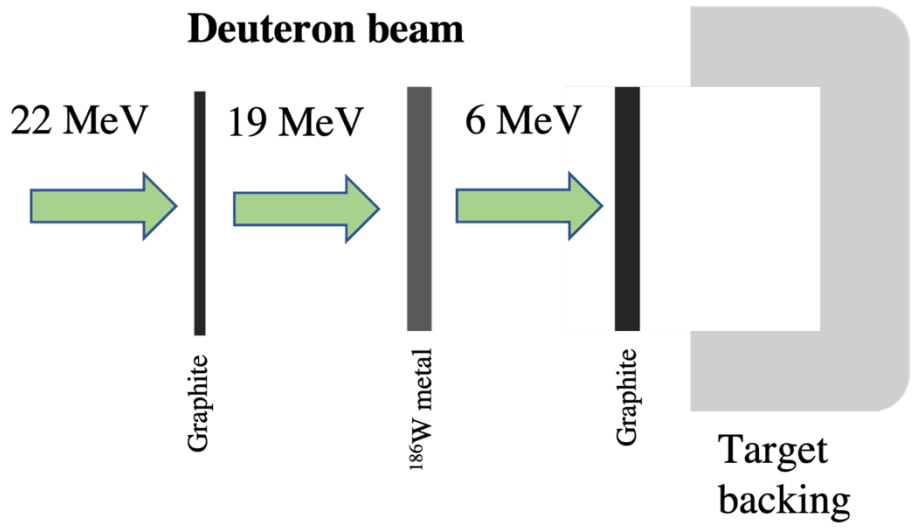

Figure 26: Solid target design showing graphite sandwiched ^{186}W metal target

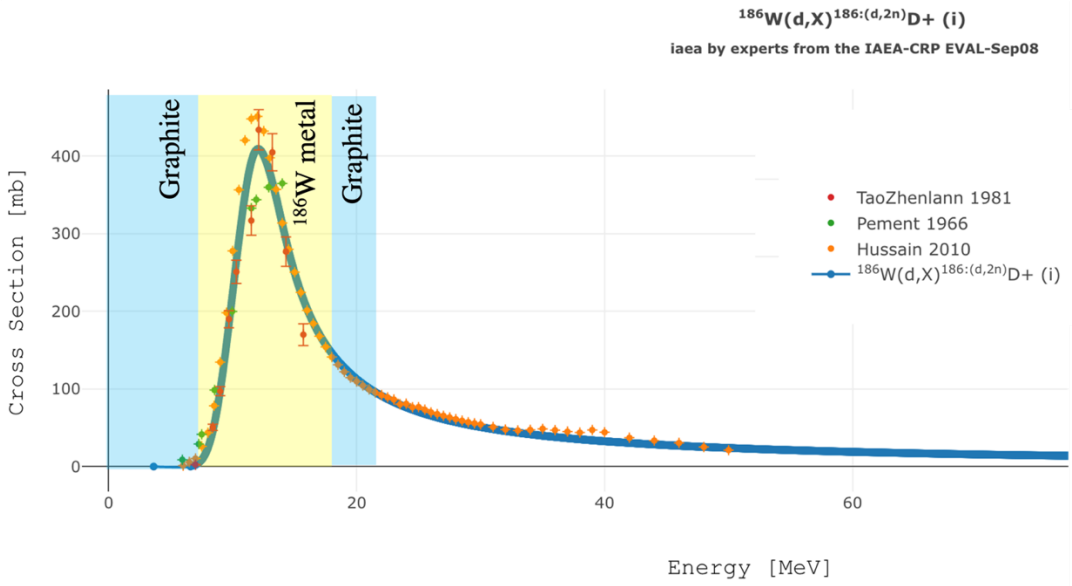

Figure 27: Combination of deuteron beam energy degradation data from SRIM and ^{186}W(d,2n)^{186}Re excitation functions in the target layers

Visual inspection of the target containing ^{186}W encased between graphite layers showed no cracks or deformities prior to being placed under high vacuum in the cyclotron (**Figure 28**).

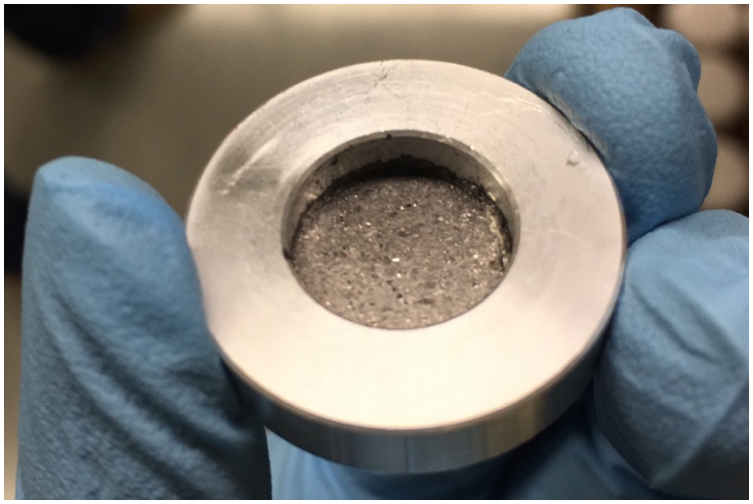

Figure 28: Photograph of the pressed target showing the upper graphite layer

A ^{186}Re yield of 0.611 GBq (16.52 mCi) at EOB was obtained after bombardment with 22 MeV deuterons for 27 μAh. To minimize the gamma dose from the co-produced ~1.5 GBq (40 mCi) of ^{187}W ($t_{1/2}$ = 24 h), the target was processed four days post irradiation (**Figure 29**). Visual inspection of the target post bombardment showed no discernable physical damage to the top graphite layer, indicating high target stability under the utilized bombardment parameters (**Figure 30**).

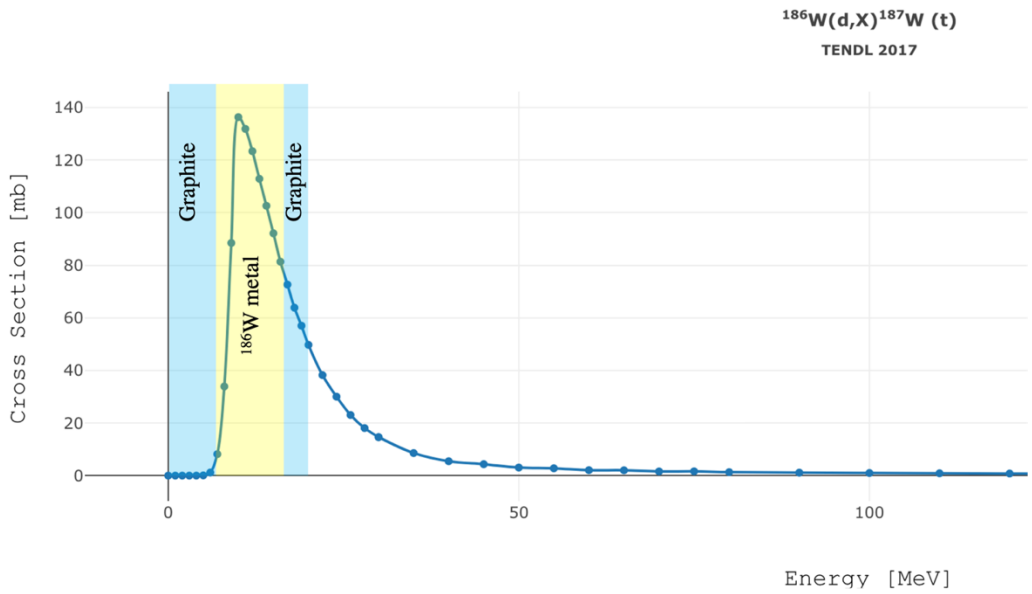

Figure 29: Combination of deuteron beam energy degradation data from SRIM and predicted $^{186}W(d,p)^{187}W$ excitation function showing the high cross section of co-produced ^{187}W

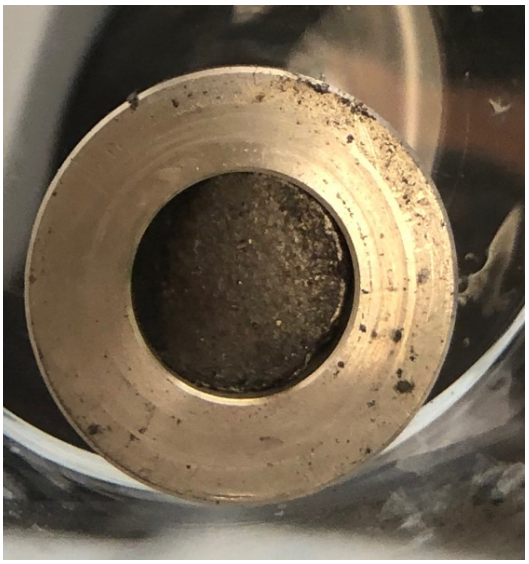

Figure 30: Photograph of the target after irradiation showing no discernable physical damage to the top graphite layer

3.3.2 Target processing and ^{186}Re isolation

Dissolution of the target post bombardment was achieved using 30% H_2O_2 with gentle heating. Teflon forceps were used to scrape off the top graphite layer to expose the ^{186}W layer to facilitate dissolution, and the H_2O_2 was decomposed by heating at 80 °C before ^{186}Re isolation.

3.3.3 Separation of [^{186}Re]ReO_4^- from the irradiated ^{186}W metal target

MEK extraction and a column separation with Analig Tc-02 were evaluated for isolation of [^{186}Re]ReO_4^- from the irradiated ^{186}W metal target. Both methods gave close to quantitative recoveries of the [^{186}Re]ReO_4^- with total isolation yields of 99% and 103% for the MEK extraction method and the Analig Tc-02 column method, respectively (**Tables 6** and **7**). The MEK extraction method achieved 94% extraction of ^{186}Re and 100% of ^{187}W recovery after one extraction. A second extraction was performed to recover residual ^{186}Re in the aqueous fraction to increase the total recovery of ^{186}Re and ^{187}W to 99% and 100%, respectively. The column method achieved 103% recovery of ^{186}Re across two elutions following the loading of the target solution and column wash, which recovered >113% ^{187}W.

Table 6. HPGe results for solvent extraction method.

Fraction	Volume (mL)	W-187 Activity[a] (%)	Re-186 Activity[b] (%)
Target solution	11.25	100	100
Aqueous (after 1st extraction)	11.25	100	2
1st MEK extraction	11.25	0	94
2nd MEK extraction	10	0	5

[a]The 480 keV gamma peak was monitored for ^{187}W. [b]The 137 keV gamma peak was monitored for ^{186}Re.

Table 7: HPGe results for column separation method.

Fraction	Volume (mL)	W-187 Activity[a] (%)	Re-186 Activity[b] (%)
Target solution	22.5	100	100
Pass-through solution	22.5	109	0
Column wash (1.5 M $(NH_4)_2CO_3$)	50	4	10
First 70 °C H_2O elution	3	0	88
Second 70 °C H_2O elution	3	0	15

[a]The 480 keV gamma peak was monitored for ^{187}W. [b]The 137 keV gamma peak was monitored for ^{186}Re.

Analysis of an aliquot of the decayed target solution revealed an EOB specific activity of 60.8 Ci/mg.

3.3.4 Radiolabeling of isolated ^{186}Re with 222-MAMA-N-propionate ligand

Prior to radiolabeling, the ligand was deprotected by cleaving the thiol-protecting trityl groups using TFA and TES (**S20-S22**). The yield of [^{186}Re]Re(V)-glucoheptonate synthesized was 77%, and a non-optimized [^{186}Re]Re(V)-222-MAMA-*N*-propionate radiolabeling yield of 18.9% was determined via radio-HPLC analysis, confirming that the HSA ^{186}Re produced by the $^{186}W(d,2n)^{186}Re$ can be used for further radiolabeling studies (**Figure 31**).

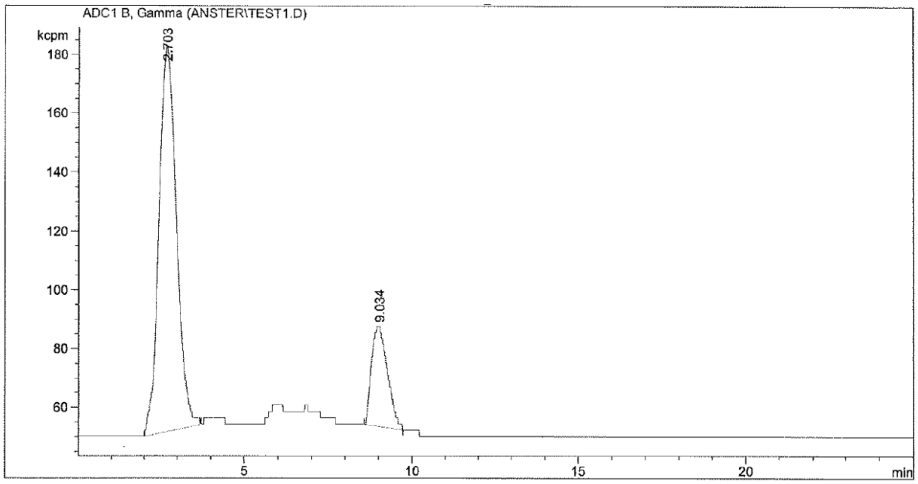

Figure 31. HPLC radio-chromatogram of radiolabeling reaction mixture showing radiolabeled [^{186}Re]Re-MAMA at 9 minutes and [^{186}Re]ReO_4^- at 2.7 minutes (20-80 % H_2O/MeCN in 20 min, 1 mL/min).

3.3.5 Comparison of Re isolation and W recovery methods

The acceptable performance of the two separation methods tested with the irradiated ^{186}W target prompted further investigations, which included five different methods to determine the most efficient process for Re isolation and W recovery for target solutions containing 350 mg and 700 mg W. The liquid-liquid extraction method was adapted from Moustapha et al. and used MEK to selectively extract ReO_4^- from the basic target solution containing WO_4^{2-} followed by purification on a small, acidified alumina column to remove any remaining WO_4^{2-} [45]. Another method developed by Balkin et al. added 3 M $(NH_4)_2CO_3$ to the dissolved tungsten target solution in a 1:1 ratio to prepare a 1.5 M $(NH_4)_2CO_3$ loading solution, which was then passed through a 1.5 M $(NH_4)_2CO_3$ preconditioned Analig Tc-02 column to elute WO_4^{2-} with successive washes of 1.5 M $(NH_4)_2CO_3$ followed by elution of ReO_4^- in 80 °C water [47, 52]. A third method

described by Gott used a 1 M NaOH loading solution into a preconditioned Analig Re-02 column, followed by successive column washes with 1 M NaOH to elute WO_4^{2-} and elution of ReO_4^- in 80 °C water [68, 70]. The final two extraction chromatography methods were developed by modifying the Balkin and Gott methods by substituting Re-02 resin for Tc-02 resin and vice versa. The liquid-liquid extraction method exploited the large difference in hydration energies and lipophilicity of WO_4^{2-} and ReO_4^- to selectively extract $NaReO_4$. The manufacturer of the Analig resins claims that their metal-selective molecular recognition technology binds to ions via a lock and key mechanism based on multiple parameters such as charge, solubility, and ion size.

3.3.5.1 Liquid extraction method

The majority of the Re-186 (94% ± 2) was isolated in the first extraction of the 350 mg tungsten metal target followed by 9% ± 1 in the second extraction (**Figure 32**). Back extractions performed on the MEK layers from the first and second extractions removed 2.0% ± 0.5 and 0.19% ± 0.06 of ^{187}W, respectively. The final 0.15 M NaCl solution containing the isolated ^{186}Re following purification with an acidified alumina column was 95% ± 2. The total tungsten recovered was 101% ± 2.

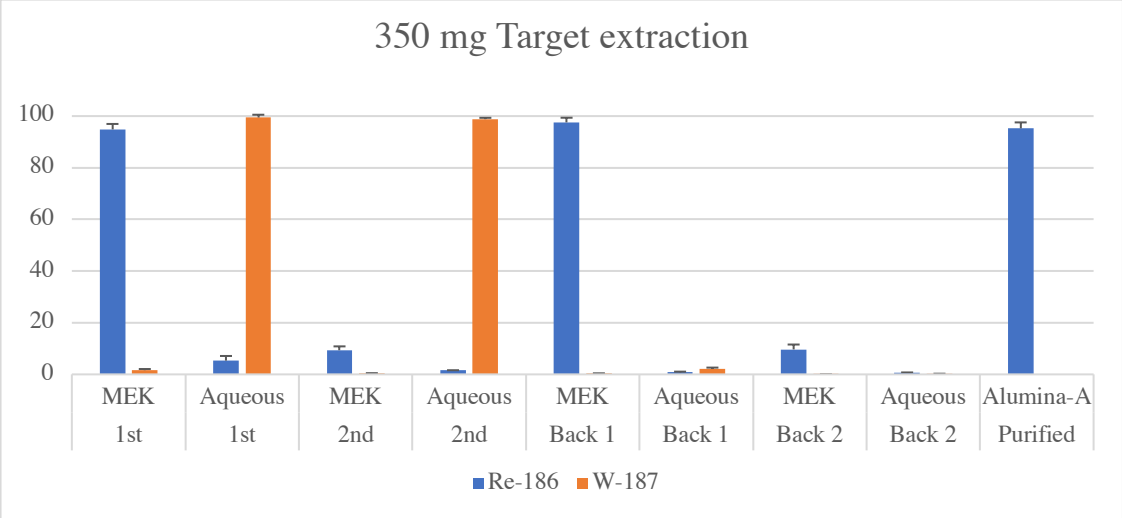

Figure 32. Chart showing results of extraction of ^{186}Re with MEK from a 350 mg W target solution (n = 3). ^{186}Re isolation and ^{187}W recovery yields of 95% ± 2 and 101% ± 2 were obtained, respectively.

Doubling the mass of tungsten metal to 700 mg showed almost identical yields for Re isolation and W recovery (**Figure 33**). Similar to the 350 mg target mass, a back extraction and acidified alumina column purification step proved vital for maximizing target recovery and reducing WO_4^{2-} in the final purified ^{186}Re, respectively.

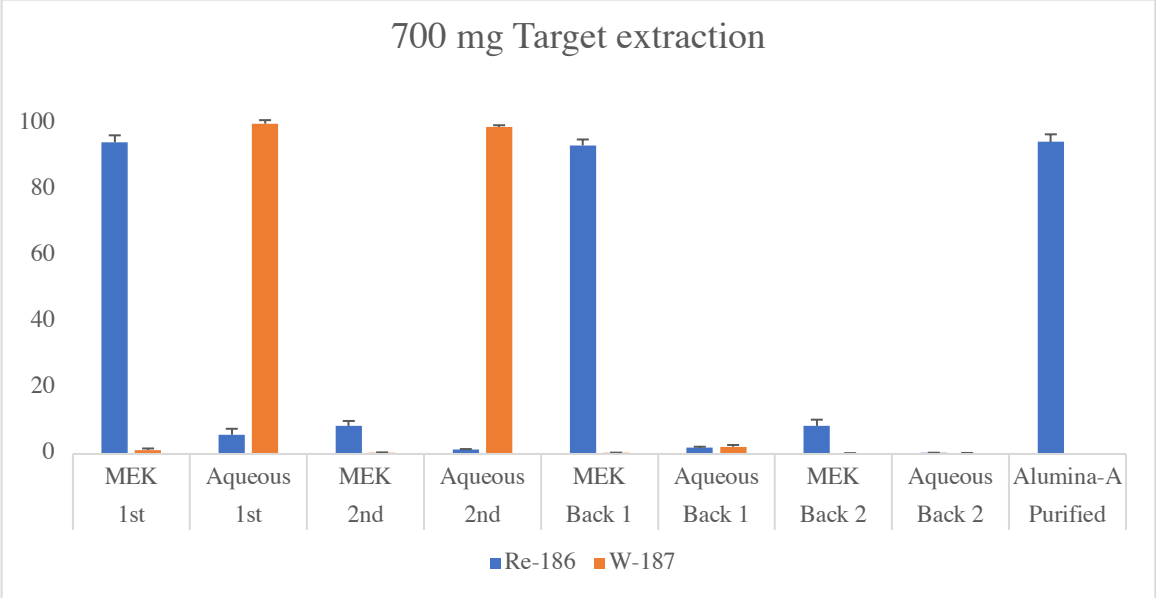

Figure 33. Chart showing results of extraction of ^{186}Re with MEK from a 700 mg W target solution (n = 3). ^{186}Re isolation and ^{187}W recovery yields of 94% ± 1 and 101 ± 2 were obtained, respectively.

The formation of emulsions at the interface between the MEK and aqueous layer initially affected the Re extraction yields. The molarity of W in the 350 mg and 700 mg W target solutions were 0.16 M and 0.32 M, respectively, with total ionic strengths of 0.48 mol/kg and 0.96 mol/kg respectively. Addition of NaCl (1 g) to the aqueous phases of the 350 mg and 700 mg W target solutions increased the ionic strength and polarity to 1.98 mol/kg and 2.46 mol/kg respectively, resulting in no emulsion formation and much improved yields [71]. The high Re isolation yields in the first extraction also eliminated the need for second and back extractions and thus dramatically reduced the time needed for the process.

3.3.5.2 Chromatographic methods in 1.5 M $(NH_4)_2CO_3$ loading solution

These methods employed Analig Tc-02 and Re-02 resins in 1.5 M $(NH_4)_2CO_3$ loading solutions for radio-chromatographic separation of ^{186}Re and ^{187}W. The ^{186}Re breakthrough was ~1% for both the 350 mg and 700 mg targets when utilizing Analig Tc-02 resin with the 1.5 M $(NH_4)_2CO_3$ loading solution, and 98% ± 2 and 99% ± 1 of the tungsten was recovered, respectively, in the pass-through and first column wash (**Figures 34** and **35**). The majority of the isolated ^{186}Re eluted in the first 3 mL (83% ± 2 and 82% ± 2, respectively) giving a total ^{186}Re yield of 92% ± 1 and 91% ± 1 for 350 mg and 700 mg, respectively.

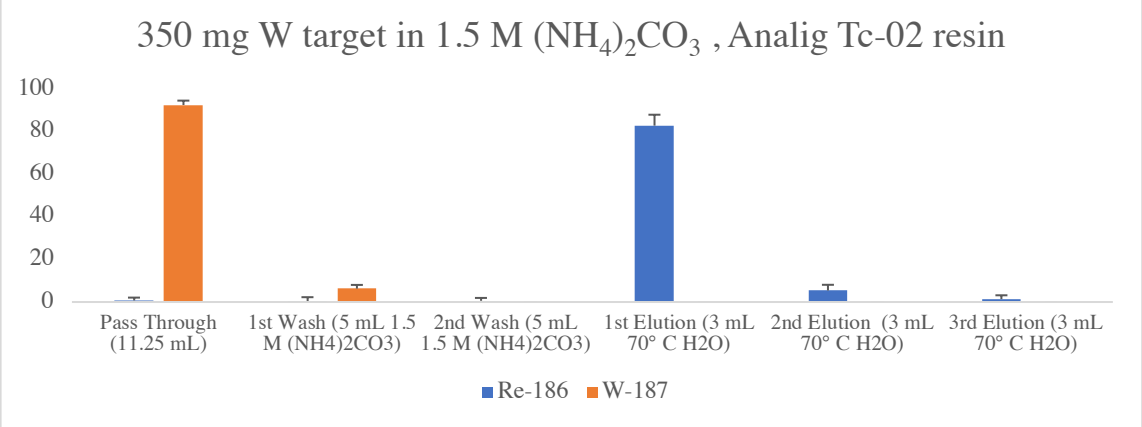

Figure 34. Chart showing results of ^{186}Re separation from a 350 mg W target solution with Analig Tc-02 resin (n = 3). ^{186}Re isolation and ^{187}W recovery yields of 91% ± 1 and 99% ± 1 were obtained, respectively.

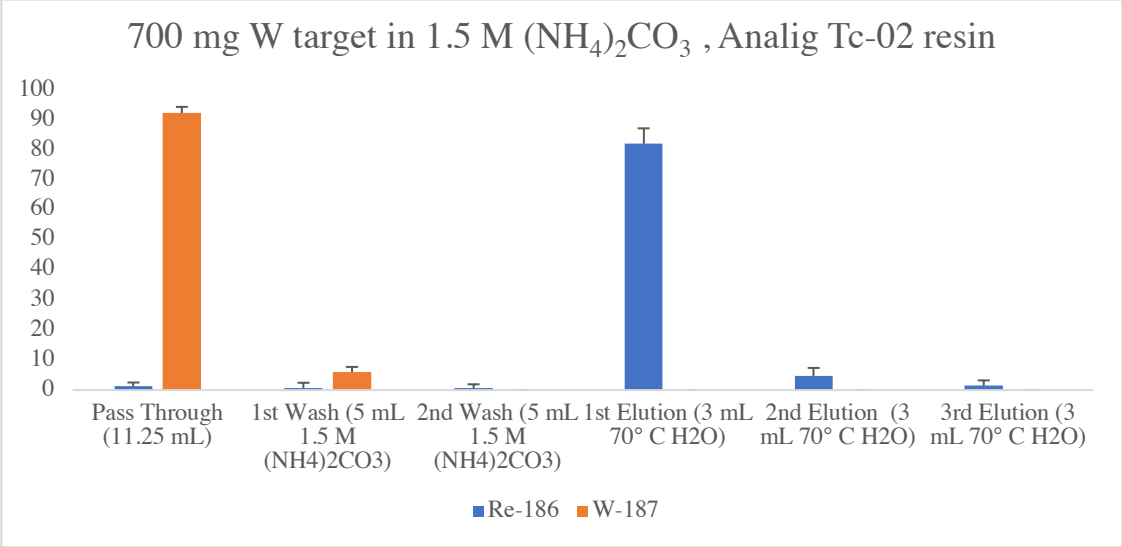

Figure 35. Chart showing results of ^{186}Re separation from a 700 mg W target solution with Analig Tc-02 resin (n = 3). ^{186}Re isolation and ^{187}W recovery yields of 91% ± 1 and 98% ± 2 were obtained, respectively.

Replacing Analig Tc-02 with Re-02 resin did not significantly reduce tungsten recovery, which remained at ~99%, but slightly reduced the total isolation yields of ^{186}Re (86% ± 4 and 87% ± 3 for 350 mg and 700 mg, respectively). This may have been due to the higher binding affinity of $^{186}ReO_4^-$ to Analig Re-02 resin, resulting in unrecovered ^{186}Re after successive elutions with 80 °C water (**Figures 36 and 37**).

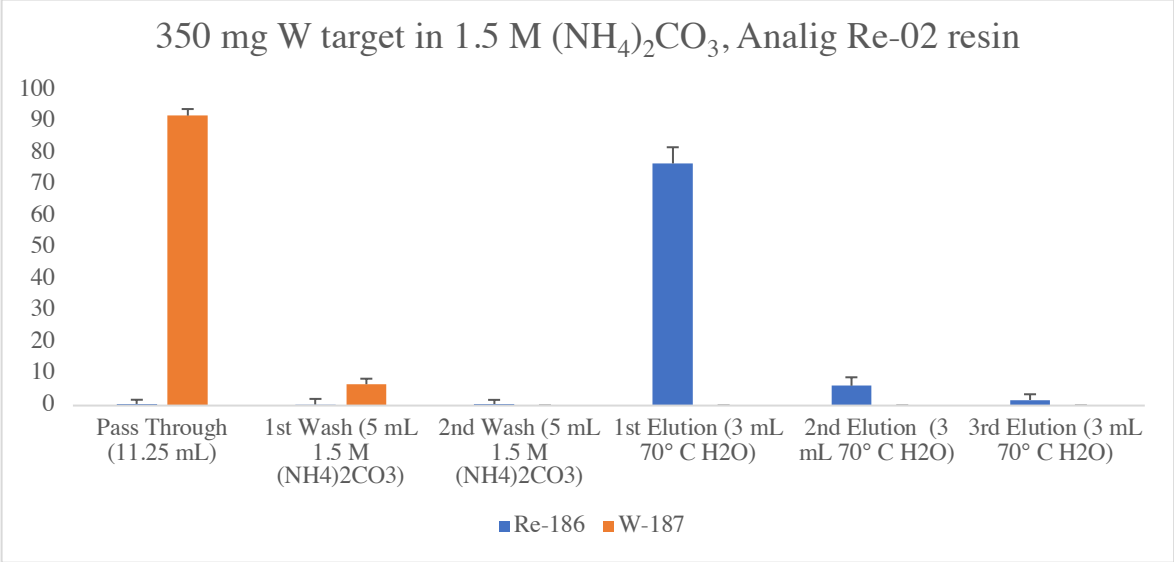

Figure 36. Chart showing results of ^{186}Re separation from a 350 mg W target solution with Analig Re-02 resin (n = 3). ^{186}Re isolation and ^{187}W recovery yields of 86% ± 1 and 98% ± 2 were obtained, respectively.

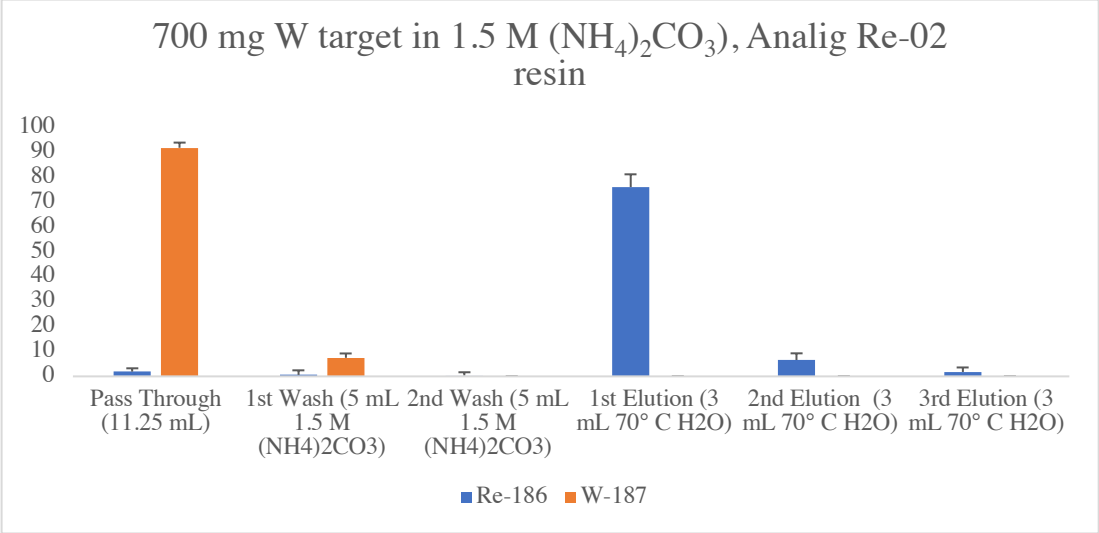

Figure 37. Chart showing results of ^{186}Re separation from a 700 mg W target solution with Analig Re-02 resin (n = 3). ^{186}Re isolation and ^{187}W recovery yields of 87% ± 3 and 99% ± 1 were obtained, respectively.

3.3.5.3 Chromatographic methods in 1 M NaOH loading solution

Replacing the 1.5 M $(NH_4)_2CO_3$ loading solution with a 1 M NaOH loading solution resulted in lower separation yields of ^{186}Re, mainly due to breakthrough during the loading phase, but ^{187}W recovery was unaffected. Using a 1 M NaOH loading solution with either the Analig Tc-02 or Re-02 resins resulted in an increase in Re breakthrough of up to 5X compared to the 1.5 M $(NH_4)_2CO_3$ loading solution (**Figures 38-39**). Gott also reported a large breakthrough of Re co-eluting with W when a high concentration of tungstate was present in the loading solution [68]. This is probably due to the comparatively higher pH of a 1 M NaOH (pH = 13) loading solution versus 1.5 M $(NH_4)_2CO_3$ (pH = 10.8) negatively affecting the binding affinity of ReO_4^- to the resin.

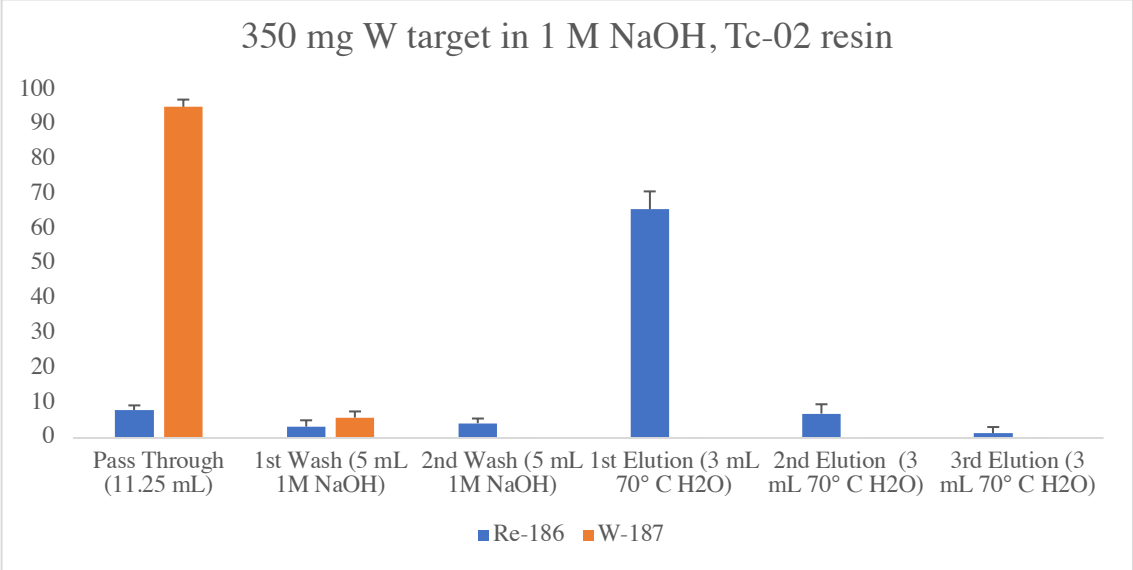

Figure 38. Chart showing results of ^{186}Re separation from a 350 mg W target solution with Analig Tc-02 resin (n = 3). ^{186}Re isolation and ^{187}W recovery yields of 81% ± 1 and 101% ± 3 were obtained, respectively.

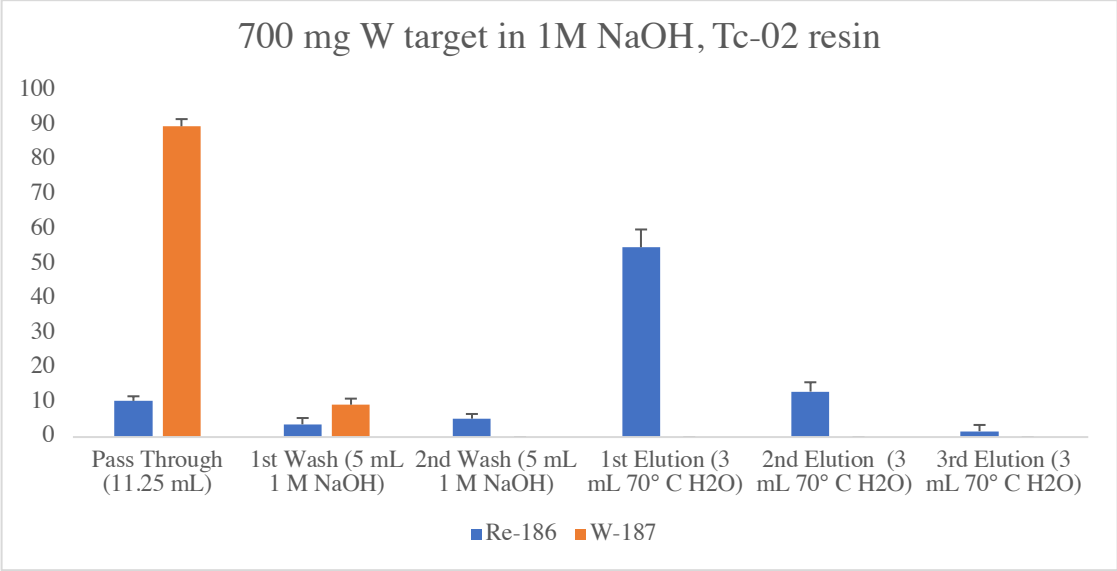

Figure 39. Chart showing results of ^{186}Re separation from a 700 mg W target solution with Analig Tc-02 resin (n = 3). ^{186}Re isolation and ^{187}W recovery yields of 79% ± 3 and 99% ± 2 were obtained, respectively.

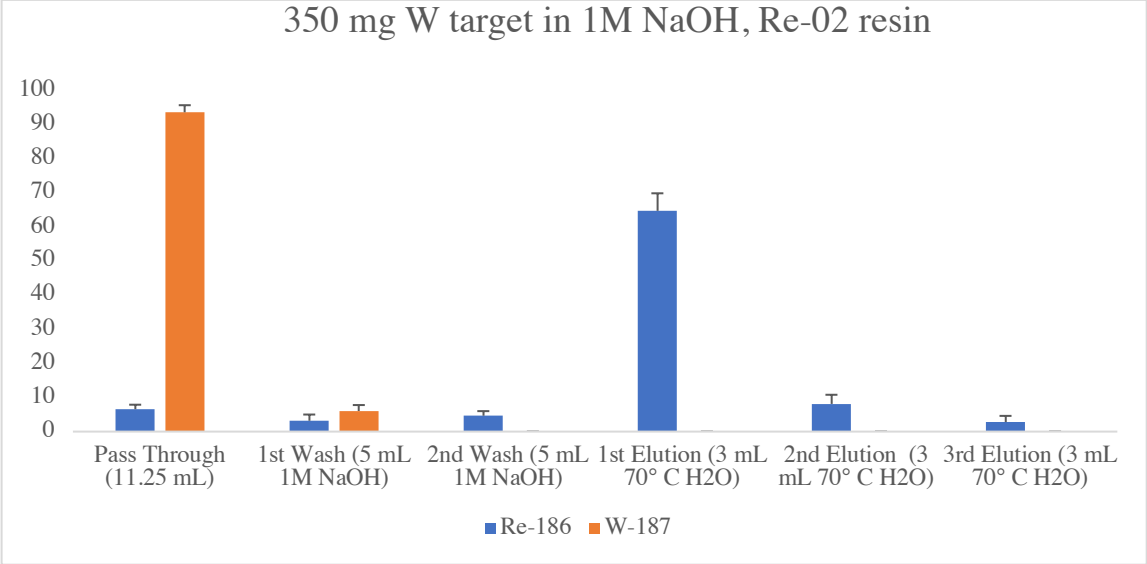

Figure 40. Chart showing results of ^{186}Re separation from a 350 mg W target solution with Analig Re-02 resin (n=3). ^{186}Re isolation and ^{187}W recovery yields of 83% ± 2 and 100% ± 2 were obtained, respectively.

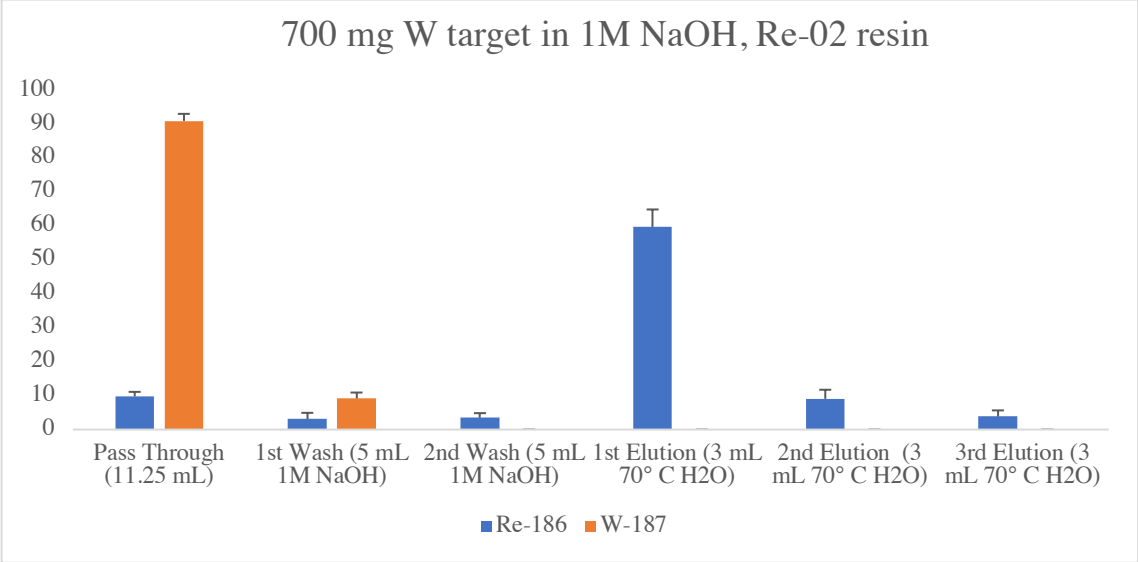

Figure 41. Chart showing results of ^{186}Re separation from a 700 mg W target solution with Analig Re-02 resin (n=3). ^{186}Re isolation and ^{187}W recovery yields of 79% ± 3 and 100% ± 3 were obtained, respectively.

3.3.5.4 Summary of separation studies

In addition to higher recovery yields of ^{186}Re, the solvent extraction method outperformed the chromatographic methods in duration by requiring only one third the time, and the best performing chromatographic method was the method developed by Balkin, which paired Tc-02 resin with a 1.5 M $(NH_4)_2CO_3$ loading solution (**Table 8**).

Table 8. Summary of ^{186}Re isolation and ^{187}W recovery yields obtained from several chromatographic separation methods.

Resin	Loading Solution	Tungsten Mass (mg)	Re-186 Isolation (%)	W-187 Recovery (%)
Analig Tc-02	1 M NaOH	350	81 ± 1	101 ± 3
Analig Tc-02	1 M NaOH	700	79 ± 1	99 ± 2
Analig Re-02	1 M NaOH	350	83 ± 2	100 ± 2
Analig Re-02	1 M NaOH	700	79 ± 3	100 ± 3
Analig Re-02	1.5 M $(NH_4)_2CO_3$	350	86 ± 4	98 ± 2
Analig Re-02	1.5 M $(NH_4)_2CO_3$	700	87 ± 3	99 ± 1
Analig Tc-02	1.5 M $(NH_4)_2CO_3$	350	92 ± 1	99 ± 1
Analig Tc-02	1.5 M $(NH_4)_2CO_3$	700	91 ± 1	98 ± 2
Liquid-liquid extraction		350	95 ± 2	101 ± 2
Liquid-liquid extraction		700	94 ± 1	101 ± 2

Due to a high backpressure in the syringe pump during the chromatographic separations, flow rates greater than 1.5 mL/min could not be used. An attempt to re-use Tc-02 resin for a subsequent separation resulted in very high backpressures and the presence of a cloudy suspension in the eluent. This rendered the material unusable after a single use due to the potential of contaminants in the eluent, which may compromise radiolabeling of the isolated ^{186}Re.

3.4 Conclusions

High specific activity ^{186}Re was produced in good yield and purity on a Scanditronix MC50 cyclotron via deuteron bombardment on an enriched ^{186}W target material. The $[^{186}Re][ReO_4]^-$ was isolated by MEK extraction and Analig Tc-02 resin followed by radiolabeling with a new 222-MAMA-*N*-ethylpropionate ligand [58]. MEK extraction is a promising method for both ^{186}Re isolation and ^{186}W recovery. It achieves higher

isolation yields of ^{186}Re than the Analig resin column methods in one-third of the total time. The high cost and lack of recyclability of the Analig resins also make them less attractive compared with the liquid-liquid extraction method. Other future studies may include the irradiation of ^{186}W and $^{186}WS_2$ target material at higher currents for longer durations to increase the yield at EOB for preclinical studies.

Chapter 4

Characterization and Reformulation of an ^{90}Y-Based Liquid Brachytherapy Agent

4.1 Introduction

Yttrium-90 ($t_{1/2}$ = 64 h, $E_{\beta\text{-max}}$ = 2.28 MeV (99.99%)) is a very good candidate for targeted radiotherapy due to its pure β^- particle emitting decay characteristics, moderate half-life and stable decay product, zirconium-90. The relatively simple chemistry of Y^{3+} ions has also facilitated the development of well-established complexes with chelating agents to fabricate therapeutic radiopharmaceuticals such as Zevalin® [72, 73]. Another outstanding advantage of ^{90}Y in therapy is the high energy of its β^- particles, which translates to an average targeted tissue range of 2.4 mm and a maximum range of 1.1 cm [74, 75]. This has been exploited by a type of radiotherapy known as radioembolization in the form of TheraSphere™ and SIR-Spheres®, which involves injecting tiny radioactive microspheres into arteries that supply the tumor [74–77].

Brachytherapy, which is another form of radiation therapy involving the implantation of sealed radioactive sources into tumors, may benefit from the decay characteristics of ^{90}Y, but a limitation of conventional brachytherapy is the patient's discomfort from intratumoral placement of multiple sources. [78, 79]. BetaBrach™, contrarily, is a novel approach to brachytherapy, formulated as a liquid suspension of ^{90}Y-labeled yttrium

hydroxycarbonate microparticles [80]. The liquid brachytherapy approach allows for implantation with a syringe for a less invasive administration [79]. The current synthetic procedure for BetaBrach™ generates the microparticles by heating a solution of urea, no-carrier added (NCA) [^{90}Y]YCl_3, and non-radioactive YCl_3 [80]. The application of heat to the solution de-composes the urea, yielding CO_2 and NH_3 *in situ* to yield a suspended precipitate of ^{90}Y-labeled hydroxycarbonate microparticles.

NCA ^{90}Y is procured by separation from its parent isotope, ^{90}Sr ($t_{1/2}$ = 28.7 y, $E_{\beta\ max}$ = 546 keV (100%)), through the use of a radionuclide generator system [81–83]. Due to the requirement for the addition of non-radioactive ^{89}Y in the synthetic procedure for BetaBrach™, the high specific activity of NCA ^{90}Y is not necessary.

Presented here is a new approach to BetaBrach™ microparticle synthesis that utilizes low specific activity (LSA) ^{90}Y produced in a nuclear reactor by way of the ^{89}Y(n,γ)^{90}Y nuclear reaction using an $^{89}Y_2O_3$ naturally monoisotopically enriched target [84]. Dissolution of the target generates $^{89/90}Y^{3+}$, which supplies the therapeutic ^{90}Y and the structural ^{89}Y required for the formulation. Physical and chemical characterization of the new BetaBrach™ formulation is also explored in this work alongside therapeutic *in vivo* studies in tumor bearing mice.

4.2 Experimental

4.2.1 Materials and methods

Chemically enriched Y_2O_3 (99.9%) was purchased from Cerac/Pure (Suffolk, UK). Urea and YCl_3 were purchased from Sigma-Aldrich (St. Louis, MO). All solvents and reagent grade acids and bases were purchased from Fisher Scientific or Sigma-Aldrich and used without further purification. Only 18 MΩ water was used during the experiments. The ^{88}Y radiotracer was purchased from Isotrak-Eckert & Ziegler (Berlin, Germany).

4.2.2 Physical measurements

Scanning electron microscopy (SEM) was performed using an FEI Quanta 600F Environmental SEM equipped with energy dispersive X-ray Spectroscopy (EDS) and a Bruker Quantax 200 Silicon Drift Detector. Transmission electron microscopy (TEM) was performed using a JEOL JEM-1400. X-ray powder diffraction (XRD) measurements were collected on a Bruker Prospector CCD diffractometer (Incoatec IμS micro-focus Cu source, λ = 1.54178 Å, 45 kV, 0.65 mA) with the samples in polyamide capillary tubes, and data were processed with DIFFRAC software. An ORTEC high purity germanium (HPGe) detector equipped with Genie multichannel analysis software was used to evaluate ^{90}Y and ^{88}Y lsamples along with a Capintec Radioisotope Calibrator CRC-7. Liquid scintillation counting (LSC) was performed using a Beckman LS6500 Multipurpose Scintillation Counter calibrated with ^{3}H and ^{14}C sources. A Perkin Elmer 2480 WIZARD^2 gamma counter equipped with a thallium activated sodium iodide crystal was used to evaluate ^{88}Y samples.

4.2.3 Physical and chemical characterization of non-radioactive microparticles

4.2.3.1 Synthesis of non-radioactive HSA-formulated microparticles

Non-radioactive HSA-formulated microparticles were synthesized in 2 mL Eppendorf vials via controlled heating of a solution of 475 μmol urea (5 M, 95 μL), 3.8 μmol YCl_3 (0.04 M, 95 μL), and 0.5 μmol HCl (0.05 M, 10 μL) in an Eppendorf Thermomixer® C (95 °C, 900 rpm, 60 min). The resulting suspension of microparticles were immediately placed in an ice bath for 20 min to stop the reaction. The reaction was also performed at 1.6 mL total volume (vs. 200 μL above) to evaluate the synthesis at a larger scale.

Additional reaction end points of 20, 40, and 60 min were also explored to investigate the growth of the microparticles during synthesis, and an additional method investigated the synthesis of microparticles using urease to decompose the urea instead of heat.

4.2.3.2 Non-radioactive yttrium oxide dissolution

Dissolution of Y_2O_3 was achieved by heating ~5 mg of the oxide in a 2 mL Eppendorf vial containing 0.35 M HCl with a ratio of 108 μL HCl per 1 mg of Y_2O_3 in a thermomixer at 90 °C and 900 rpm for 40 min to obtain a dissolved target solution.

4.2.3.3 Synthesis of non-radioactive LSA-formulated microparticles

Non-radioactive LSA-formulated microparticles (200 μL scale) were synthesized in 2 mL Eppendorf vials via controlled heating of a solution of 475 μmol urea (5 M, 95 μL), 2.7 μmol YCl_3 (0.045 M, 61 μL), and dissolved target solution (44 μL, 1.1 μmol YCl_3) in an

Eppendorf Thermomixer® C (95 °C, 900 rpm, 60 min). The resulting suspension of microparticles were immediately placed in an ice bath for 20 min to stop the reaction.

4.2.3.4 Microscopy analysis with SEM and EDS

SEM samples of freshly synthesized non-radioactive microparticles were prepared by transferring approximately 1 μL of vortexed microparticle suspension onto a silicon wafer that was then dried in an oven for 1 min at 50 °C. Following drying, the samples were mounted into the microscope and placed under vacuum. Due to crowding and stacking of the microparticles in the center of the silicon wafer, sample images for SEM and EDS were collected near the edge. Radioactive microparticles synthesized with ^{90}Y were also imaged by SEM after they were allowed to decay.

4.2.3.5 Stability tests of microparticles

Three 1.6 mL batches of LSA-formulated non-radioactive microparticles were prepared and stored at room temperature on a benchtop and exposed to light for 1 week. Aliquots were drawn from each sample after thorough mixing and analyzed using SEM. The samples were stored for 1 additional week under the same conditions followed by analysis using SEM. The stability of the microparticles was also tested in water by centrifuging aliquots of the microparticle suspension at 7000 rpm for 10 min and removing the supernatant, followed by resuspension in 1 mL water and storing for up to 2 weeks at room temperature.

The stability of one-week-old microparticles in phosphate buffered saline (PBS, 1X, pH ~7.4) solution was also tested. A one-week-old sample (200 μL) was centrifuged for 10 minutes, then the supernatant was removed. The particles were then resuspended in 200 μL of PBS and stored at room temperature for 1 week on a benchtop, followed by analysis using SEM and EDS. Additional SEM images of the PBS-incubated microparticles were collected after rinsing the microparticles with 1 mL water twice to remove the sodium chloride.

4.2.3.6 Target irradiations and dissolution

LSA ^{90}Y was produced by irradiating quartz ampoule sealed targets of Y_2O_3 (3.5-5 mg) in the flux trap at the University of Missouri Research Reactor (MURR) at a thermal flux of ~2.4 E+14 n/cm^2/s and a resonance flux of ~4.8 E+12 n/cm^2/s for ~156 h. Following irradiation, the targets were opened in a glove box with a cutting tool, and the radioactive Y_2O_3 was transferred into a 2 mL Eppendorf vial containing 0.35 M HCl with a ratio of 108 μL HCl per 1 mg of Y_2O_3. The mixture was heated in a thermomixer at 90 °C and 900 rpm for 40 min to achieve dissolution.

4.2.3.7 LSA-formulated radioactive microparticle synthesis and QC assessment

Depending on the irradiation parameters such as target mass, neutron flux and irradiation time, the concentrations of the reagents were varied to synthesize microparticles that contained equal ratios of $^{90}Y^{3+}$ and $^{89}Y^{3+}$. LSA-formulated radioactive microparticles (200 μL scale) were synthesized in 2 mL Eppendorf vials via controlled heating of a solution of 475 μmol urea in H_2O (4.1-5 M, 95-114 μL), 2.5-3.5 μmol YCl_3 in H_2O (0.049-0.075

M, 51-61 μL), dissolved LSA ^{90}Y target solution in HCl (50-8000 μCi), and ^{88}Y tracer (0-10 μCi) in an Eppendorf Thermomixer® C (95 °C, 900 rpm, 60 min) for particle migration and therapy studies in mice. The resulting suspension of microparticles were immediately placed in an ice bath for 20 min to stop the reaction.

QC methods were developed to test for ^{90}Y incorporation into the microparticles after synthesis. The microparticle suspension was vortexed for 1 min then a 20 μL aliquot was quickly transferred into a separate vial. A 90 μL portion of the remaining microparticle suspension was centrifuged at 7000 rpm for 10 min and 20 μL of the supernatant was transferred into a new vial. The final 90 μL of the microparticle suspension was filtered through a 0.22 micron filter, then 20 μL of the filtrate was transferred into a new vial. The activity in the three 20 μL aliquots were determined using dose calibrator or LSC readings.

4.2.3.8 *In vivo* particle migration studies

A study was designed to investigate the reproducibility of the microparticle synthesis across 3 batches from 2 LSA ^{90}Y productions, and the migration of the radioactive microparticles in healthy Balb/c, female mice (n=3 per batch). All applicable institutional and/or national guidelines for the care and use of animals were followed. More specifically, animal studies were conducted in compliance with a protocol approved by the Subcommittee for Animal Safety at the Harry S. Truman Memorial Veterans' Hospital and the Animal Care and Use Committee of the University of Missouri Animal Care Quality Assurance Office. The cells were obtained from the CIC (51 million cells, 4.6 total mL, 97% viability), then rinsed twice with PBS, followed by centrifugation at

1000 rpm for 2 minutes. The cells were then re-suspended to a concentration of $1x10^6$/0.1 mL (total volume 5.0 mL) with PBS. The microparticles used for this study were radiolabeled with LSA ^{90}Y and tracer ^{88}Y, with 50 μCi of ^{90}Y and 10 μCi of ^{88}Y administered to each mouse via 20 μL intramuscular (IM). The mice were humanely sacrificed 8 d post administration and the tissues were counted with a gamma counter.

Particle migration was also studied in tumor bearing mice (n = 3) following the implantation of 10^6 EMT-6 cells into the right flank. The microparticles used for this study were radiolabeled with LSA ^{90}Y and ^{88}Y tracer with 800 μCi of ^{90}Y and 10 μCi of ^{88}Y administered to each mouse via 20 μL intratumoral (IT) administration, 10 d post-inoculation. The mice were humanely sacrificed 8 d post-injection, and the tissues were counted with a NaI detector.

4.2.3.9 *In vivo* Therapy studies

The therapeutic effect of microparticles radiolabeled with LSA ^{90}Y was also investigated in EMT-6 tumor bearing mice (n = 7). A dose of 6.2 μCi of ^{90}Y was administered via 20 μL intratumoral (IT) injections. Control studies were performed alongside the ^{90}Y radiolabeled microparticles, with 20 μL saline and 20 μL non-radioactive microparticles IT administrations, each n=7. The volume of the tumors was measured in the days following administration until ulceration was observed in the tumors.

4.3 Results and Discussion

4.3.1 Synthesis of yttrium hydroxycarbonate microparticles

The synthesis of multiple batches of yttrium hydroxycarbonate microparticles according to the current HSA formulation protocol was achieved by the controlled decomposition of urea in the presence of Y^{3+} ions at 95 °C in 60 min. Since the source of ^{90}Y in this protocol is of high specific activity, the quantity of Y from ^{90}Y addition is negligible compared to the 3.8 μmol of Y required for the generation of the yttrium hydroxycarbonate microparticles, which and is added as a solution of $^{89}YCl_3$.

Conversely, microparticles synthesized by the new LSA formulation method receive a significant fraction of their total Y content from the dissolved target solution, therefore less Y must be supplemented with a solution of $^{89}YCl_3$ to make up the required 3.8 μmol of total Y. **Table 9** below summarizes 3 microparticle preparations of different ^{90}Y doses prepared according to the LSA formulation method. The source of the radioactivity was the 5 mg mass Y_2O_3 targets after irradiation for 1 week in the flux trap at MURR. Transferred aliquots of the dissolved irradiated target contained varying amounts of carrier ^{89}Y, and a simple calculation determined the required amount of ^{89}Y to be added from the $^{89}YCl_3$ stock solution.

Table 9: Examples of three microparticle preparations showing the ratio of transferred $^{89/90}Y$ versus supplemented ^{89}Y to make up the required Y total of 3.8 μmol.

^{90}Y activity used in preparation (mCi)	Transferred $^{89/90}Y$ (μmol)	^{89}Y added (μmol)
0.05	0.28	3.52
9.03	1.3	2.5
0.065	0.08	3.72

4.3.2 Dissolution of Y_2O_3 target for LSA formulation method

A robust target dissolution method was developed by varying the acid type, acid concentration, acid volume, and temperature of the dissolution mixture. The optimal parameters were found to be 108 μL of 0.35 M HCl per 1 mg of Y_2O_3 at 95 °C for 40 min. The volume of acid was kept to a minimum to preserve a high activity concentration of the dissolved target solution before transferring an aliquot into the microparticle reaction vial. The number of moles of excess HCl was also kept to a minimum since the use of higher concentrations of HCl failed to produce a microparticle suspension at the end of synthesis.

4.3.3 Physical and chemical characterization of yttrium hydroxycarbonate microparticles

Analysis of three batches of each non-radioactive LSA-formulated and HSA-formulated microparticles by SEM revealed similar morphology between the two formulation methods owing to spherical particles that were interestingly interconnected to neighboring spheres to form clusters (**Figure 42**). The sizes of the spheres demonstrated some variability between batches across both methods in agreement with data published by Lee et al. [85].

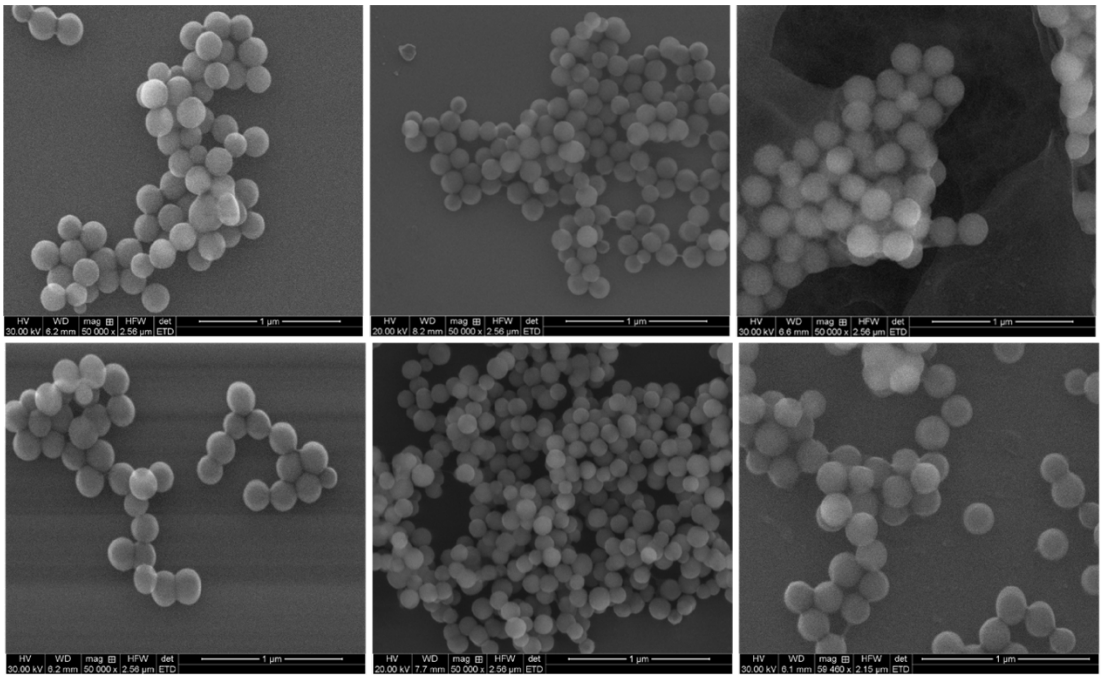

Figure 42: SEM images of HSA-formulated (top row) and LSA-formulated (bottom row) microparticles synthesized in different batches and imaged on the day of synthesis.

Particle size analysis of one sample from each method gave further insight into the size distribution of the spheres. The spheres from the HSA method displayed an average diameter of 271 ± 35 nm (**Figure 43**). Comparably, the spheres from the LSA method

exhibited an average diameter of 258 ± 30 nm (**Figure 44**). The size distributions loosely followed a gaussian distribution.

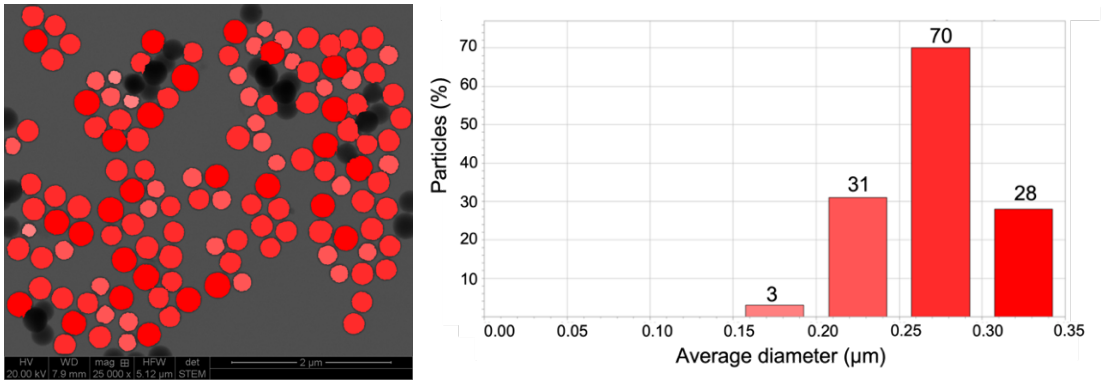

Figure 43: Particle size analysis of particles synthesized using the HSA formulation. Average sphere diameter = 271 ± 35 nm. The color palette of the spheres represents different size categories and corresponds to the colors on the histogram.

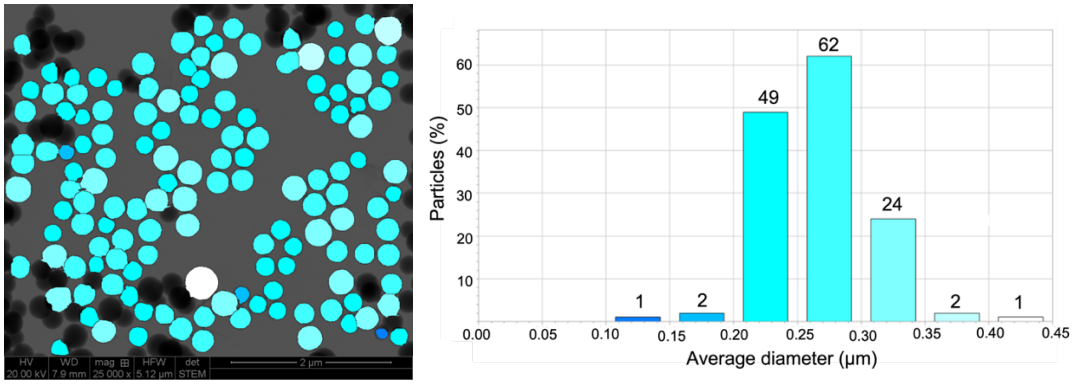

Figure 44: Particle size analysis of particles synthesized using the LSA formulation. Average sphere diameter = 258 ± 30 nm. The color palette of the spheres represents different size categories and corresponds to the colors on the histogram.

The chemical composition of the spheres from the new LSA formulation was determined qualitatively using TEM/EDS. Emissions of the characteristic X-rays produced during the analysis confirmed the presence of Y, O and C in the sample (**Figure 45**).

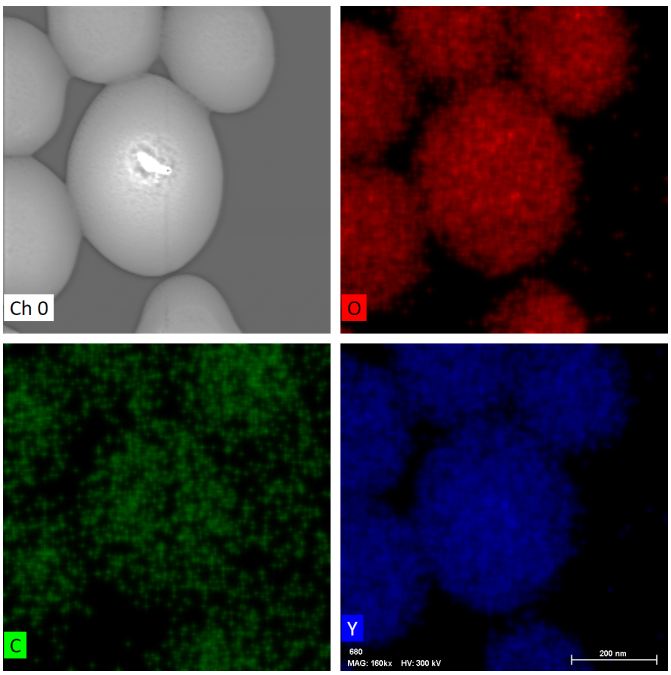

Figure 45: TEM/EDS of LSA-formulated microparticles showing the signals for elemental O (red), C (green), and Y (blue).

Analysis of the microparticles synthesized for reaction end points of 20, 40, and 60 min revealed an increase in the size of the spheres from 20 min to 40 min, but no discernable difference between the 40 min and 60 min endpoints (**S26**). The method that relied on urease to synthesize microparticles resulted in the formation of irregular spheres with a large distribution in the range of size and shape of the spheres (**S27**) and thus not further pursued.

4.3.4 Stability studies of non-radioactive LSA-formulated microparticles

The microparticles synthesized by the LSA formulation displayed high stability after being stored at room temperature and in water. SEM analysis revealed no discernable difference between freshly prepared microparticles, 1-week-old microparticles in their reaction media, and microparticles stored in water for 2 weeks (**Figures 46** and **47**).

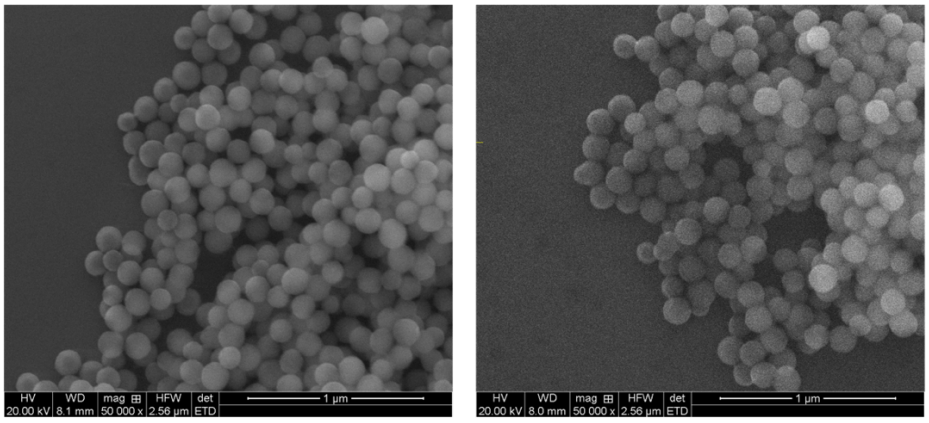

Figure 46: SEM images of non radioactive LSA-formulated microparticles on the day of synthesis (left) and after 2 weeks stored at room temperature in reaction media (right).

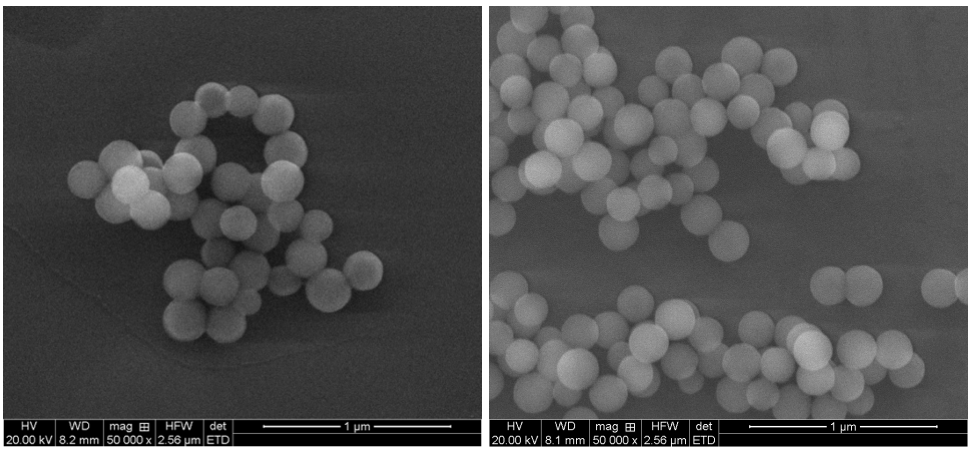

Figure 47: SEM images of non radioactive LSA-formulated microparticles on the day of synthesis (left) and after 2 weeks stored in water (right).

Analysis of decayed LSA-formulated microparticles imaged four months after synthesis revealed no discernable changes in their morphology, giving further support to their high stability (**Figure 48**).

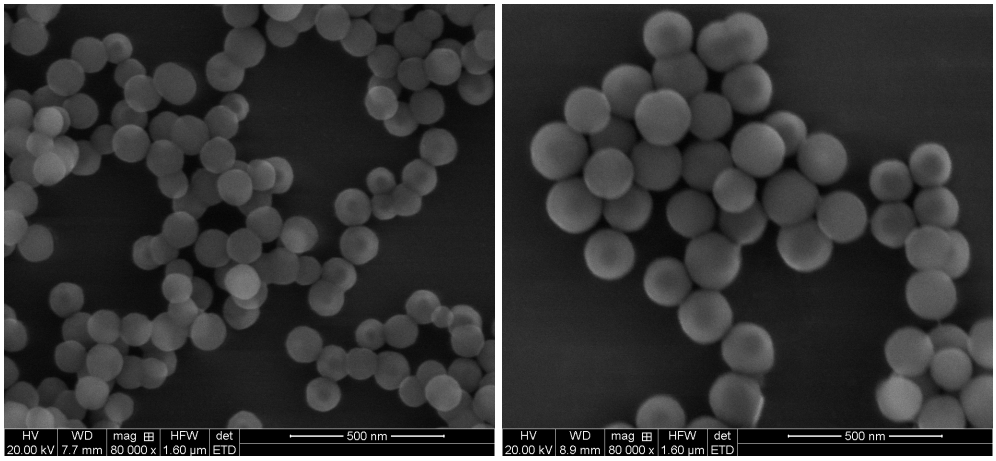

Figure 48: SEM of non-radioactive LSA-formulated microparticles (left) and decayed LSA-formulated microparticles imaged 4 months after radiosynthesis (right).

However, incubation of LSA-formulated microparticles in PBS, as a surrogate for the biological environment of cells, revealed a dramatic change in their morphology as evidenced by SEM (**Figure 49**).

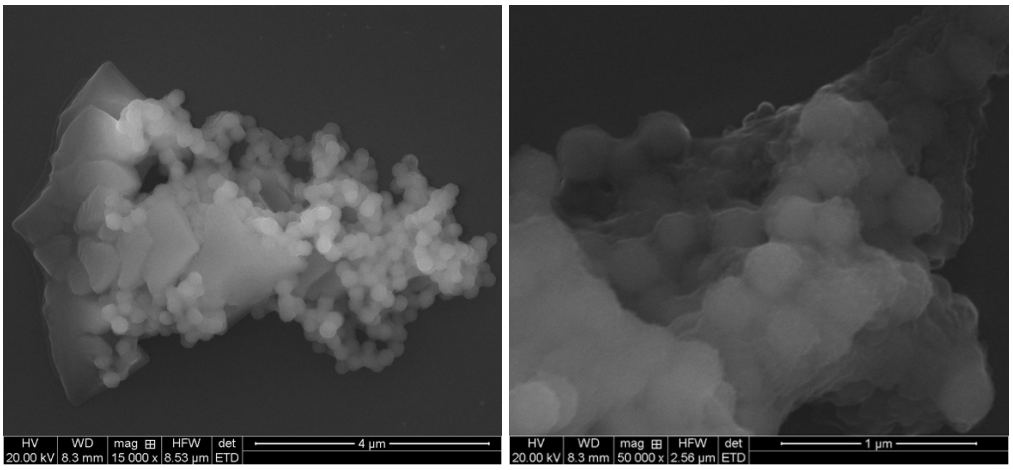

Figure 49: SEM images of microparticles after incubation in PBS solution for 1 week

SEM/EDS analysis provided further insight, revealing the incorporation of phosphorus on the surface of these microparticles (**Figure 50**).

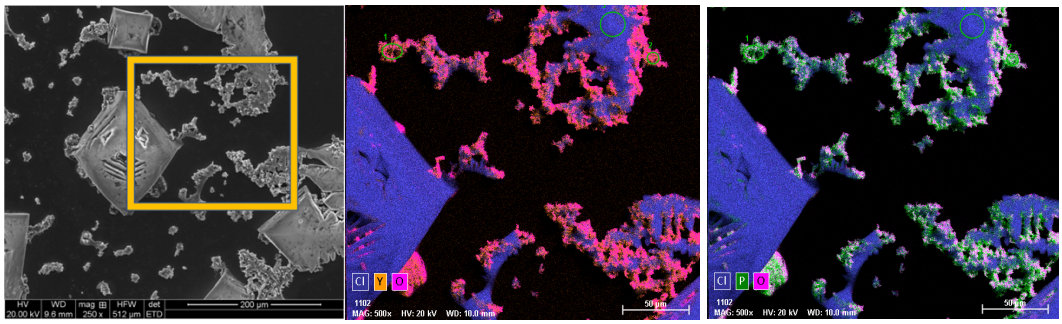

Figure 50: SEM/EDS images of LSA-formulated non-radioactive microparticles after incubation in PBS solution for 1 week. The yellow box in the image on the left represents the field of view of the middle and right images. The color key displays the elements that

correspond to the colors in the SEM/EDS map. NaCl crystals are present due to crystalization during the sample preparation.

Rinsing the PBS-incubated microparticles with water to remove the NaCl allowed for a closer examination of the difference in their structure compared to freshly prepared microparticles, interestingly revealing a similar size distribution (**Figures 51** and **52**).

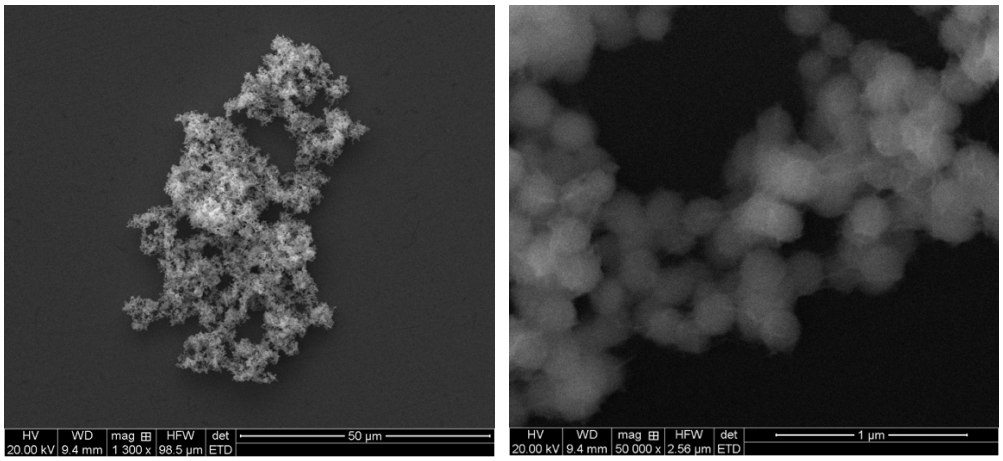

Figure 51: SEM images of water-rinsed microparticles after incubation in PBS solution for 1 week.

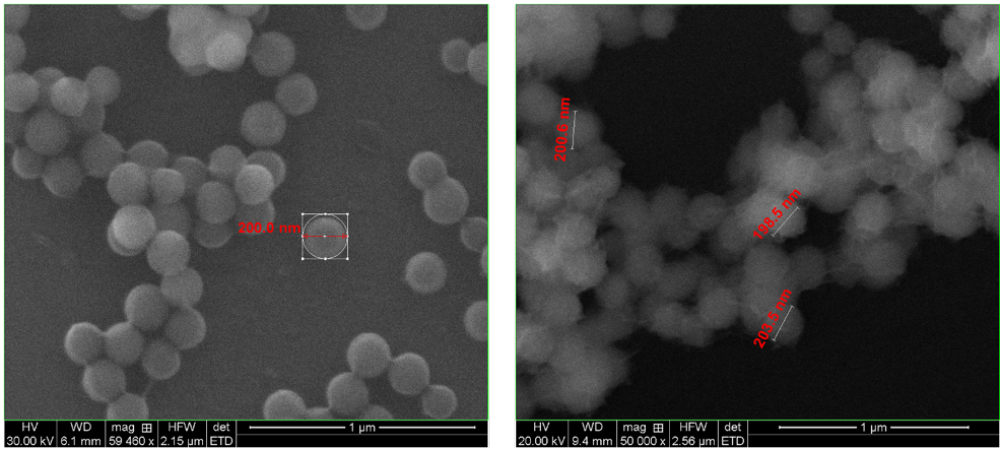

Figure 52: Left, SEM image of non-radioactive LSA-formulated microparticles on the day of synthesis. Right, SEM image of microparticles after being incubated in PBS for 1 week and then rinsed with water.

A possible explanation for this phenomenon is an ion exchange mechanisim between the phosphate ions in solution and the hydroxide and carbonate ions in the microparticles. A study done by Haron et al. demonstrated the removal of phosphate ions from solution using basic yttrium carbonate microparticles prepared by a similar method to this study [86]. The study also revealed a strong correlation between the amount of phosphate adsorbed by the microparticles and the amount of carbonate released, but due to the increase in pH during the incubation period, it was hypothesized that the hydroxide ions in the microparticles were also involved in the exchange [86]. These characteristics may also prove to be favorable for the retention of microparticles in tissues after administration since cell membranes are composed of phospholipids.

4.3.5 *In vivo* migration studies

The radioactive microparticles prepared across three batches for the IM migration studies were synthesized using LSA ^{90}Y from two reactor production runs. The microparticles that were prepared for the first IM migration study were synthesized on the same day that the ^{90}Y target was removed from the reactor. The microparticles that were prepared for the second IM migration study were synthesized using ^{90}Y from the same irradiated target as the first preparation, two days after the EOI. The third microparticle preparation was synthesized using a new target on the same day that the ^{90}Y target was removed from the reactor. The QC tests performed prior to the administration of the microparticles confirmed a radiochemical purity of >92% across all batches during the course of the studies (**Table 10**). Slight variations in the radiochemical purity of the microparticles may be attributed to excess acid transferred into the reaction vial from the transfer of an aliquot of the dissolved target solution; a partial transfer of the total mass of the Y_2O_3 irradiated target before the dissolution process means that the dissolved target solution contained excess moles of HCl.

Table 10: Summary of the radioactive microparticle activities used for mouse migration and therapy studies, and the results of their corresponding QC tests after synthesis

Study	^{90}Y activity (μCi)	^{88}Y activity (μCi)	Activity in supernatant (%)	Actvity in filtrate (%)
IM migration 1	50	10	5.5	7.5
IM migration 2	50	10	1.6	0.9
IM migration 3	50	10	7.9	6.1
IT migration	8000	10	5.6	6.3
IT therapy	6.2	0	0.3	0.2
IT migration	6.2	0	0.3	0.2

The results of the intramuscular migration study suggested a design flaw in the study. Localization of an injected volume into muscle tissue is challenging due to the fibres and striations in the structure of the tissue as well as high vascularity [87, 88]. Analysis of the tissues of the mice revealed inconsistency in percent dose of the ^{88}Y tracer at the site of the administration (**Figures 53-55**).

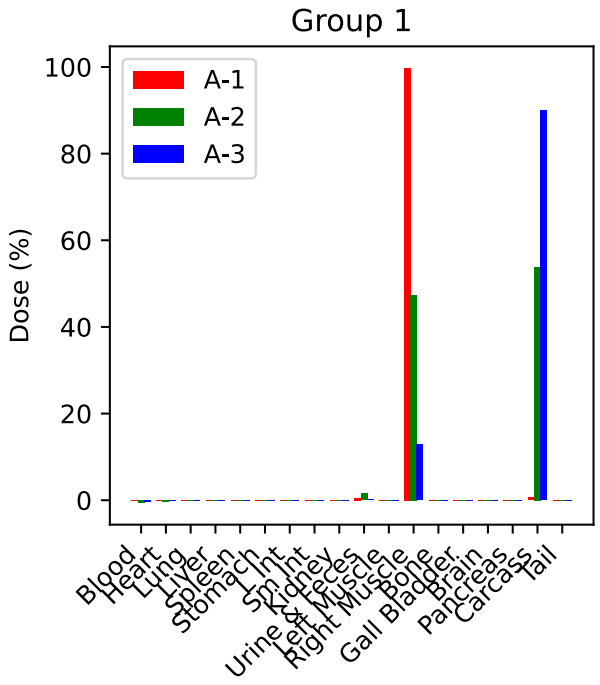

Figure 53: Biodistribution of ^{88}Y tracer in mice (n=3) following 20 µL IM administration of microparticles (^{90}Y: 50 µCi, ^{88}Y: 10 µCi) in the first migration study

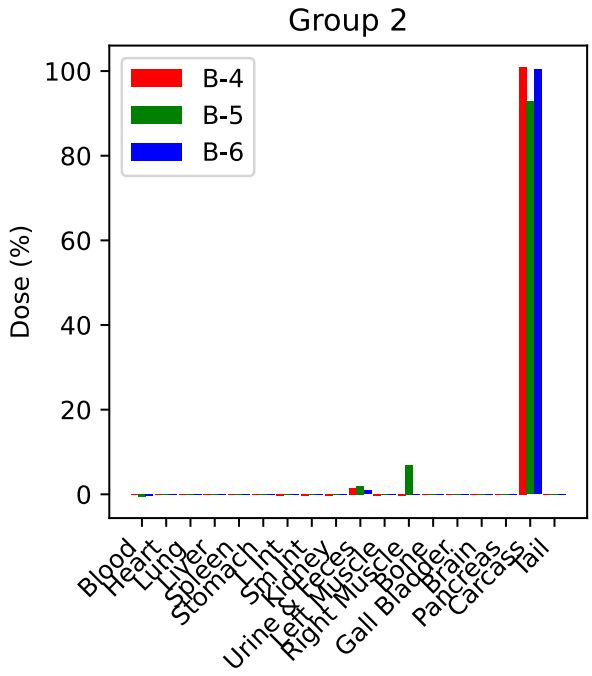

Figure 54: Biodistribution of ^{88}Y tracer in mice (n=3) following 20 µL IM administration of microparticles (^{90}Y: 50 µCi, ^{88}Y: 10 µCi) in the second migration study

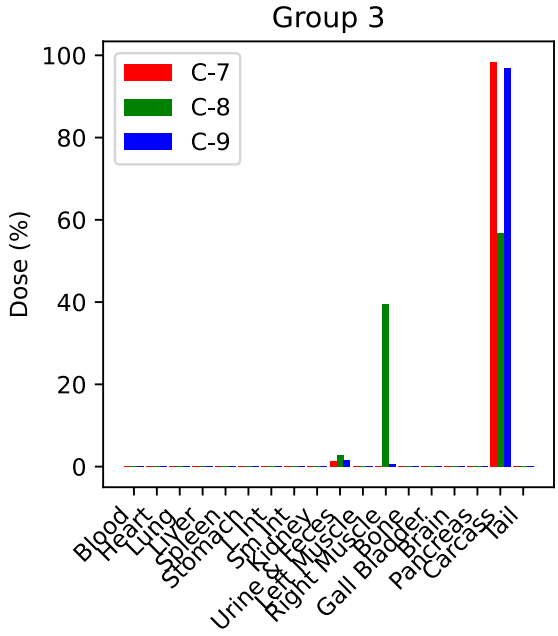

Figure 55: Biodistribution of ^{88}Y tracer in mice (n=3) following 20 µL IM administration of microparticles (^{90}Y: 50 µCi, ^{88}Y: 10 µCi) in the third migration study

However, since only one of the muscles in the right thigh of the mice was extracted for counting, this could suggest that the large percent injected dose measured in the carcass was due to localized microparticles left behind in the right thigh. The lack of percent dose in the other tissues and organs also suggests that the ^{88}Y-labeled microparticles did not migrate from the site of administration.

The microparticle migration studies performed in the mice bearing EMT-6 tumors showed more promising results. However, the intratumorally injected activity of 800 μCi of ^{90}Y per tumor caused an estimated 5000 Gy dose at the surface of the tumors instead of the intendeded 50 Gy. This extremely high dose resulted in necrosis of the skin and tumor at the site of the IT administration. In addition, the muscle directly below the tumor exhibited deterioration due to radioactive burns. The outcome of this is reflected in **Figure 56**, which shows an unexpectedly high percent injected dose in the right muscle and carcass of the mice.

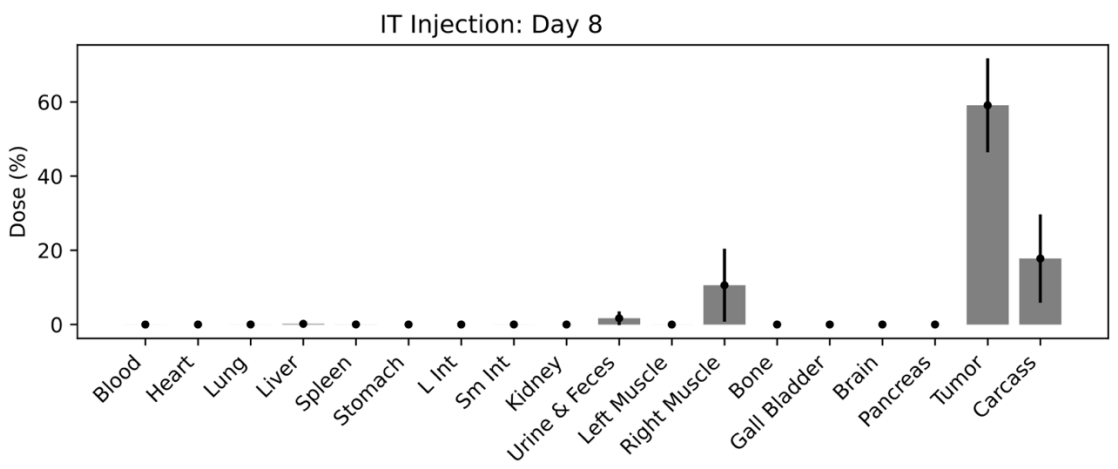

Figure 56: Biodistribution of ^{88}Y tracer in mice (n=3) following 20 μL IT injection of microparticles (^{90}Y: 800 μCi, ^{88}Y: 10 μCi).

4.3.6 *In vivo* Therapy studies

Prior to the therapy study, the optimal for IT administration was determined by a Monte Carlo simulation by Dr. Charles Maitz to be 8 μCi in 20 μL of ^{90}Y per tumor. As expected, the mouse control group that was injected with saline had the fastest growing tumors. Interestingly, the control mice injected with non-radioactive ^{89}Y microparticles showed a slower growth rate than the saline injected mice (**Figure 57**). The actual activity of ^{90}Y injected into the tumors of the therapy group of mice was ~6.2 μCi instead of 8 μCi, due to a miscalculation during the microparticle synthesis, resulting in a lower than intended IT dose. Regardless, the trend seen in **Figure 57** suggests a therapeutic effect of the ^{90}Y-labeled microparticles over both non-radioactive microparticles and saline administrations.

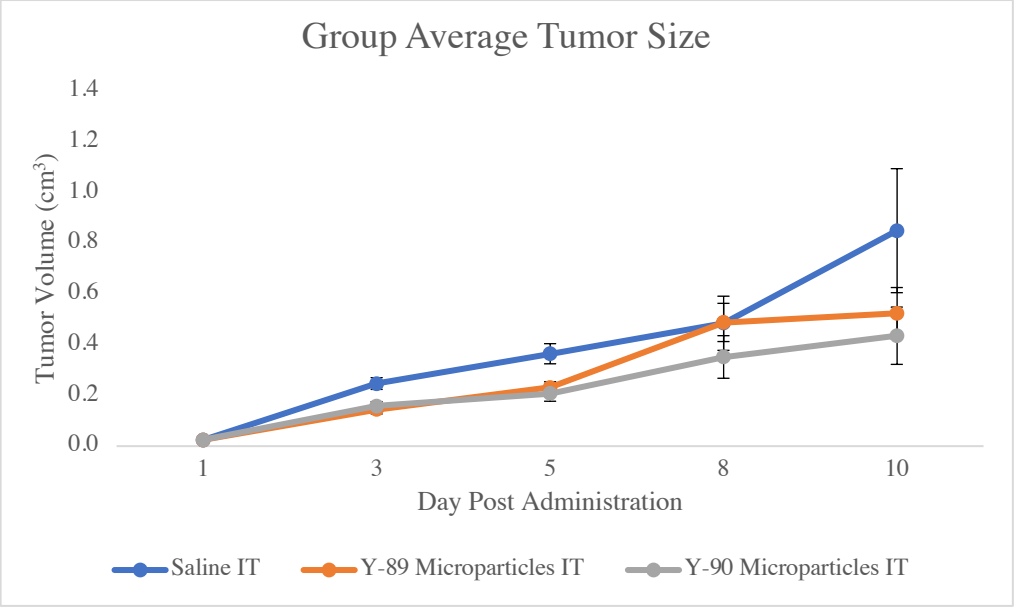

Figure 57: Growth rate of the tumors in mice injected with saline, non-radioactive microparticles, and 6.2 μCi of ^{90}Y-labeled microparticles.

Examination of the tumor volume data from each group revealed an insignificant difference between the non-radioactive microparticles and ^{90}Y-labeled microparticle treatments ($p = 0.35$) (**Figure 57**). The tumors administered with non-radioactive microparticles displayed a slower but statistically insignificant trend in growth rate compared to the saline administered tumors ($p = 0.26$) suggesting that the phosphate ion exchange effect may provide a therapeutic benefit. The tumors administered with ^{90}Y-labeled microparticles displayed an even slower growth rate compared to the saline administered tumors ($p = 0.17$), but the difference was also insignificant perhaps due to the suboptimal dose.

The tumor growth curves of the individual groups reflect that ulceration began to occur in the tumors injected with saline much earlier than the non-radioactive microparticles and ^{90}Y-labeled microparticles (**Figures 58-60**). The study was ended on day 10 post IT treatment.

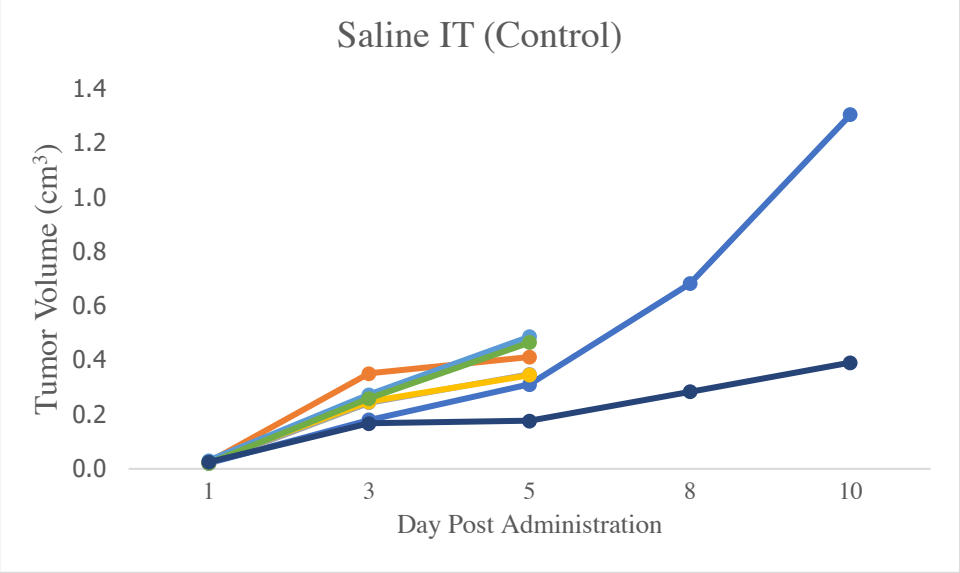

Figure 58: Growth curves of the tumors in mice injected with saline.

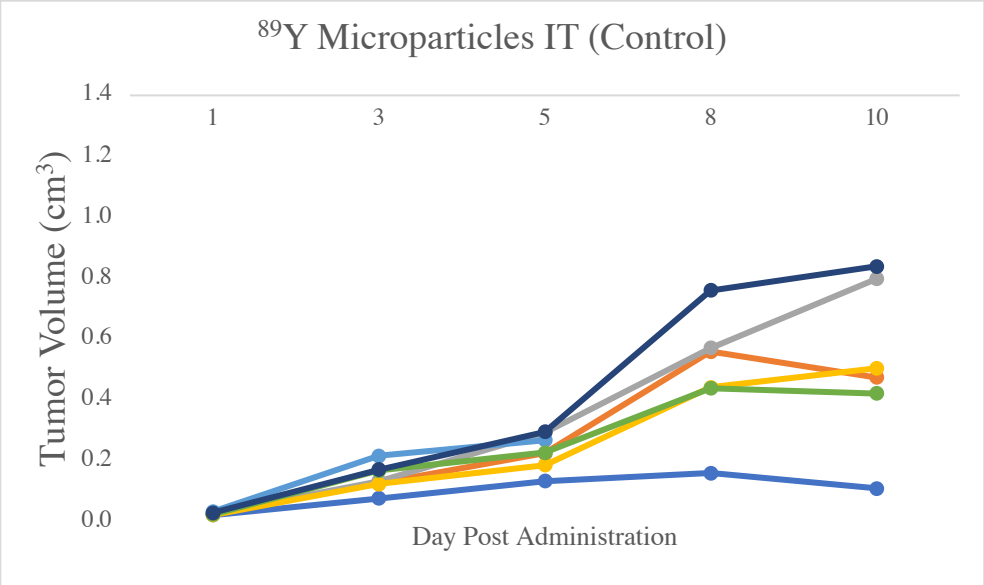

Figure 59: Growth curves of the tumors in mice injected with non-radioactive microparticles.

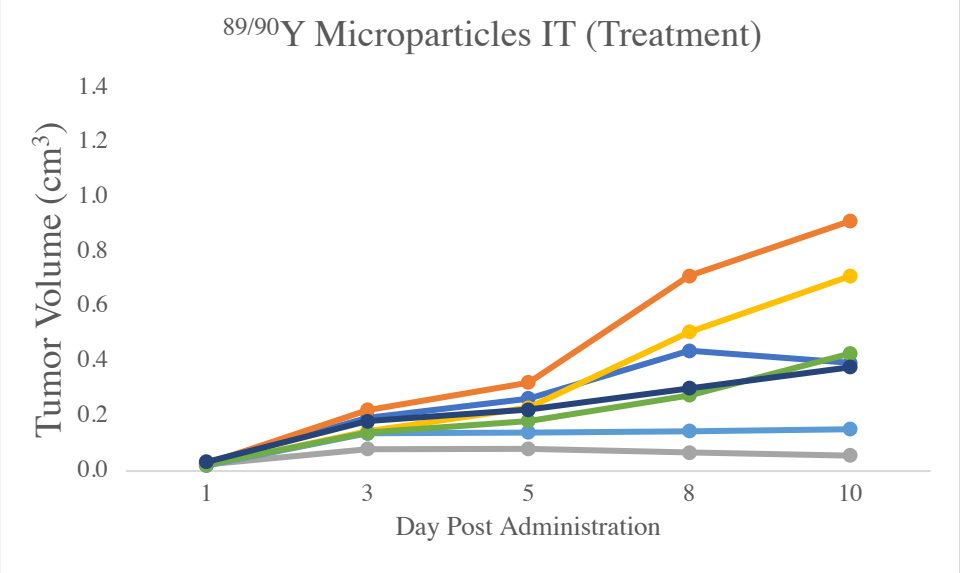

Figure 60: Growth curves of the tumors in mice injected with ~6.5 µCi of ^{90}Y-labeled microparticles.

An error in the tumor volume calculations used in the Monte Carlo simulation resulted in a simulation with tumor volumes 4.4x smaller than the actual tumors. A corrected "as delivered" simulation revealed that the actual average dose on the surface of the tumors was 37 Gy, 26% lower than the desired 50 Gy (**Figure 61**).

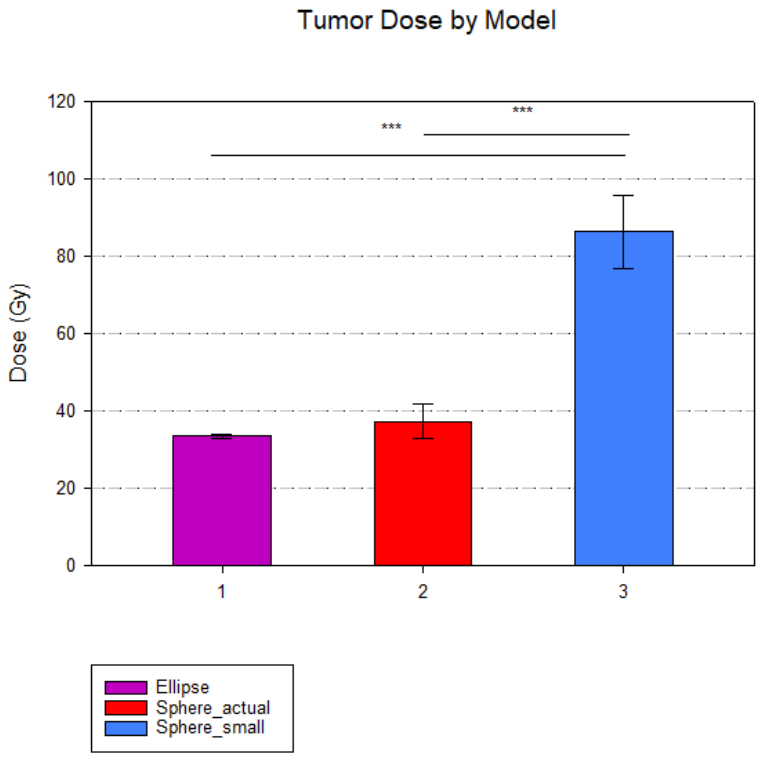

Figure 61: Monte Carlo estimated actual doses on the surface of tumor volumes of ellipsoid and spherically-shaped tumors and spherical tumors that were 4.4x smaller in volume.

An additional biodistribution study (n=3 mice) was performed with lower activity administrations of 6.2 μCi of ^{90}Y-labeled microparticles, showing a much improved retention of the dose at the IT injection site (**Table 11**). The elevated carcass activity

observed in Mouse C was ruled out as an outlier by a Dixon Q-Test ($Q_{statistic} = 0.996 > 0.994$ at an alpha level of 0.01).

Table 11: Biodistribution of ^{90}Y in mice (n=3) following 20 μL IT injection of microparticles (^{90}Y: 6.2 μCi) in an IT study.

%Administered dose		
Organ	**Mouse A**	**Mouse B**
Blood	0.00	0.00
Heart	0.00	0.00
Lung	0.00	0.00
Liver	0.01	0.00
Spleen	0.00	0.00
Stomach	0.00	0.00
L Int	0.00	0.00
Sm Int	0.00	0.00
Kidney	0.00	0.00
Urine & Feces	0.39	5.19
Left Muscle	0.00	0.00
Right Muscle	0.02	0.02
Bone	0.00	0.00
Gall Bladder	0.00	0.00
Brain	0.00	0.00
Pancreas	0.00	0.01
Tumor	**99.18**	**94.59**
Carcass	0.39	0.19

4.4 Conclusions

A new formulation of BetaBrach™ was developed using LSA ^{90}Y produced via the $^{89}Y(n,\gamma)^{90}Y$ nuclear reaction using $^{89}Y_2O_3$ naturally enriched targets. A robust target dissolution method was also developed alongside QC test methods for radiochemical purity assessment of the radiomicroparticles. The newly reformulated LSA method microparticles displayed similar morphology to the microparticles synthesized by the HSA formulation method and were stable in water over two weeks. Incubation of the microparticles in PBS revealed both a change in their appearance and the incorporation of phosphorous, suggesting an ion exchange process between phosphate ions in solution and the carbonate and/or hydroxide ions of the microparticles, offering as a potential explanation of microparticle retention. The microparticles displayed a retention of >94% at the IT administration site in mice, and a modest (though not significant) therapeutic effect was observed in mice treated with ^{90}Y-labeled microparticles over non-radioactive microparticles and saline control treatments. Using these findings to improve our *in vivo* study design, studies are underway to investigate the therapeutic effect of microparticles in A375 tumor bearing mice with an optimized dose of ^{90}Y-labeled microparticles. These preclinical studies are expected to provide preliminary data to support testing of the LSA formulated microparticles in feline oral squamous carcinoma patients, as a spontaneous cancer model of human head and neck cancer.

Chapter 5

General Summary and Future Directions

5.1 Summary of the production of HSA ^{186}Re in a small medical cyclotron

The ability to routinely produce HSA ^{186}Re by way of the ^{186}W(p,n)^{186}Re nuclear reaction in a small medical cyclotron with ~16.5 MeV protons would be an exciting prospect for the development of ^{186}Re-based radioimmunotherapy drugs. The availability of more than 1000 small medical PET cyclotrons globally and 150 in the US would democratize the supply of single digit millicurie quantities of HSA ^{186}Re for preclinical studies (**Figure 62**) [89, 90]. The cost effectiveness of the synthesis and recyclability of enriched $^{186}WS_2$ targets, coupled with the simple MEK liquid-liquid extraction may also encourage adoption.

Figure 62: Geographical distribution of PET Cyclotrons in the US [89].

However, the amount of ^{186}Re radioactivity that can be produced using a PET cyclotron is not sufficient for therapy studies because the EOB yields are limited by a relatively low reaction cross section[47, 52]. The irradiation schedule of most medical cyclotrons is also designed to maximize the production of PET tracers such as ^{18}F for clinical applications and would also limit the possibility of longer irradiations for higher ^{186}Re yields.

5.2 Summary of the production of HSA ^{186}Re at the UW Medical Cyclotron Facility

Deuteron bombardment of enriched $^{186}WS_2$ targets to produce ^{186}Re by way of the ^{186}W(d,2n) ^{186}Re reaction offers higher EOB yields over the ^{186}W(p,n) ^{186}Re reaction owing to a maximum reaction cross section that is ~7x higher [61]. The lack of co-produced Re nuclides also allows for a target design that maximizes the thickness of the $^{186}WS_2$ layer to ensure a beam degradation that corresponds to the maximum region of the excitation function. The difference in EOB ^{186}Re yields obtained from the irradiation of $^{186}WS_2$ targets via the ^{186}W(p,n) ^{186}Re and ^{186}W(d,2n) ^{186}Re reactions can be seen in **Figure 63**, which shows yields of 41.9 mCi and 3.5 mCi, respectively. It should be noted that the mass of $^{186}WS_2$ required to prepare targets that degrade 19 MeV deuterons to 6 MeV is higher than the mass needed to degrade ~10.8 MeV protons to ~7.6 MeV, thus, a significant amount of the increase in yield is due to the higher number of ^{186}W nuclei in the deuteron irradiated target. Another noted advantage was the confirmed higher EOB ^{186}Re specific activity of 60.8 Ci/mg from a ^{186}W(d,2n) ^{186}Re irradiation versus 38.5 Ci/mg from a ^{186}W(p,n) ^{186}Re irradiation.

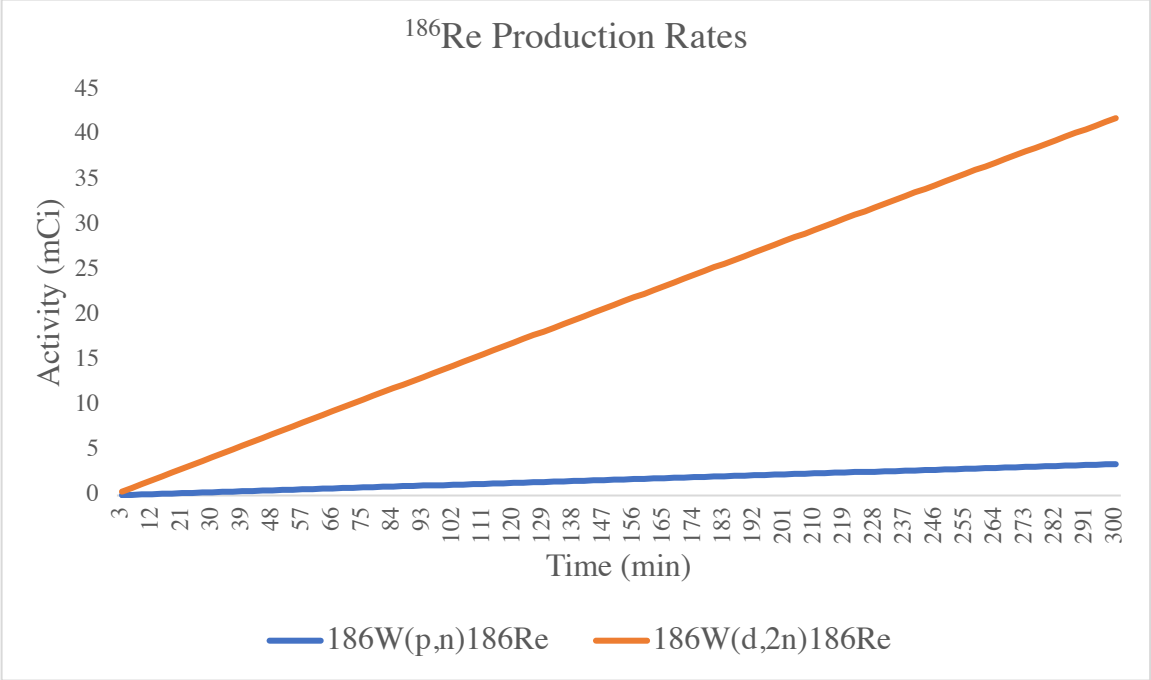

Figure 63: Production rates of ^{186}Re from the irradiation of $^{186}WS_2$ targets via the $^{186}W(p,n)^{186}Re$ and $^{186}W(d,2n)^{186}Re$ reactions.

Production of HSA ^{186}Re by deuteron bombardment is not without its own challenges, as evidenced by the co-production of ^{187}W during irradiation (**Figure 64**). The nuclide's relatively short half-life of 24 h and high energy gamma emissions pose a hazard to operators during the target dissolution and ^{186}Re separation processes. Exposure to ^{187}W can be mitigated by allowing it to decay until the dose levels are more manageable, but this solution is not practical dues to the concurrent loss of ^{186}Re during this decay period resulting in lower yields and specific activity.

The more appropriate solution would be to perform the processes inside of a hot cell or a glove box to shield the user from the high levels of radiation.

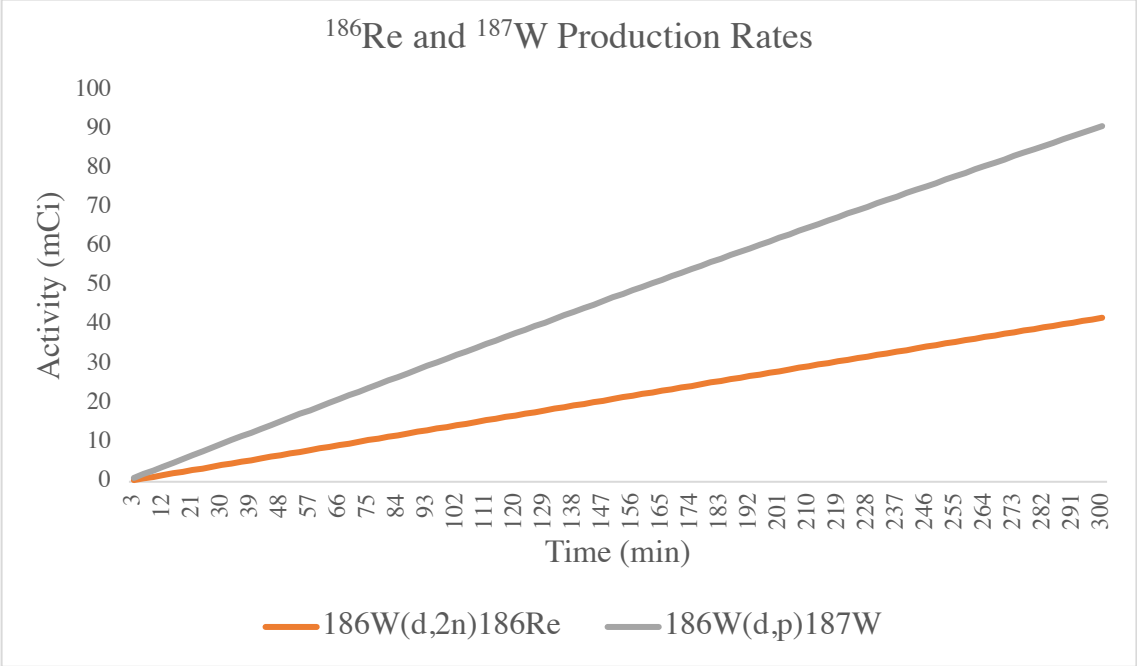

Figure 64: Production rates of ^{186}Re and co-produced ^{187}W from the irradiation of $^{186}WS_2$ targets via the ^{186}W(d,2n) ^{186}Re and ^{186}W(d,p) ^{187}W reactions.

Another potential limitation of deuteron irradiation would be the increase in damage sustained by the target material during irradiation due to the higher LET of the deuterons compared to targets irradiated with relatively lower LET protons [91]. This effect would become more pronounced when higher currents and higher irradiation times are utilized.

5.3 Summary of the production of HSA ^{186}Re at BNL

The Brookhaven Linac Isotope Producer (BLIP) at Brookhaven National Lab offers unique features that would allow ^{186}Re to be produced at a larger scale via the proton bombardment of $^{186}WS_2$ targets for substantially longer periods than what is possible in a medical cyclotron. The ^{186}W(p,n) ^{186}Re reaction reaches a theoretical maximum production yield at roughly 60 days when a 30 μA proton beam is used (**Figure 65**). The

BLIP is currently capable of irradiating targets continuously for periods of up to several months and the irradiation of an enriched $^{186}WS_2$ target identical in mass and thickness to the ones described in Chapter 2 for ~60 days would result in an EOB yield of ~85 mCi (**Figure 65**). Irradiating the target for ~15 days would be a more efficient use of the facility, yielding ~80 mCi at EOB.

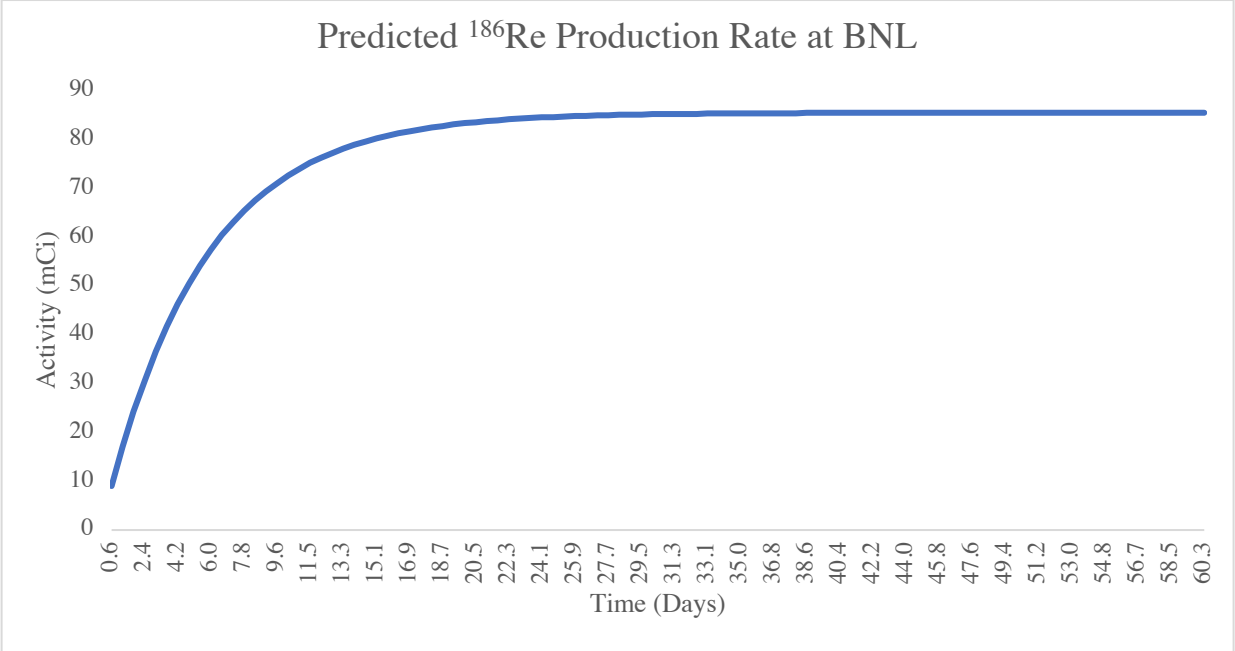

Figure 65: Production rates of ^{186}Re from the irradiation of $^{186}WS_2$ targets via the $^{186}W(p,n)^{186}Re$ reactions at BNL.

The target cooling capabilities at the BLIP would also offer significant improvements over what is achievable in a medical cyclotron to facilitate elevated currents. The current solid target design utilized for the irradiations in Chapter 2 creates a vacuum on the front of the target capsule which only allows heat to be extracted from the front lid by conduction through the inner layers of the target and then through the water contact on

the back of the target. Since roughly one third of the heat generated in this target capsule originates from heat buildup in the lid, irradiations at higher currents are severely limited by this flaw, resulting in target failure at the front. Some medical cyclotrons are equipped with helium cooling gas on the front of the target to aid in heat extraction, but helium gas is significantly less effective at cooling compared to water. The BLIP utilizes a target design that is submerged in cooling water to aid in heat extraction (**Figure 66**) [92].

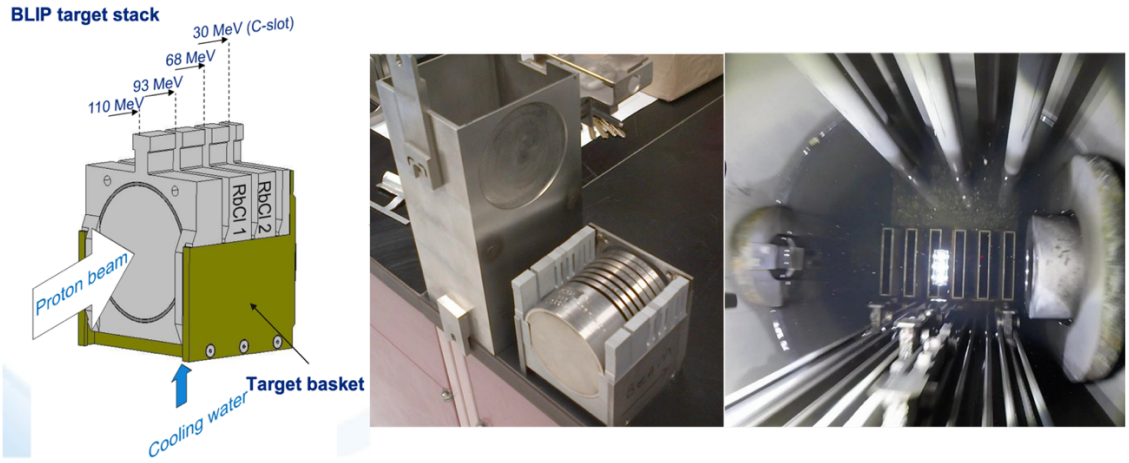

Figure 66: Schematic of BLIP target stack and target basket (left). Photograph of target stack and target basket (middle). Photograph of the cooling water system [92].

Another advantageous feature available at the BLIP is beam rastering, which spreads out the power density of the beam on the targets to improve reliability and yield. The implementation of this feature has led to a 50% overall increase in yields in some targets [92].

The target design at the BLIP is also capable of accommodating much larger targets than medical cyclotrons. The targets utilized in Chapters 2 and 3 were limited to ~13 mm in diameter, while the BLIP can accommodate targets at ~70 mm in diameter [92].

Exploiting this feature along with the efficient cooling and sophisticated beam rastering at the facility could theoretically facilitate hundred milliCurie-Curie EOB ^{186}Re yields to support large clinical therapy studies based on HSA ^{186}Re radiopharmaceuticals.

5.4 Summary of the production of LSA ^{90}Y for BetaBrach™ at MURR

MURR is capable of producing large quantities of ^{90}Y for clinical studies based on LSA formulated BetaBrach™. The largest target mass (~5.5 mg) used in the preclinical studies in Chapter 4 produced ~170 mCi of ^{90}Y after a 1-week irradiation in the flux trap at MURR. Increasing the target mass to 20 mg would produce an ^{90}Y yield to ~630 mCi if self-shielding is not taken into consideration. Alternatively, the total yield of ^{90}Y can be increased to several Curies by irradiating several targets at once should demand arise. Large scale productions would likely decrease the cost of acquiring LSA ^{90}Y at the end user level, making it an attractive alternative over HSA ^{90}Y.

Since the radiochemical purity of the microparticles is affected by the amount of acid in the reaction, the synthesis of the microparticles needs to occur within a time window that preserves the activity concentration of the dissolved target solution to ensure that the aliquot transferred to the reaction vial is kept to a minimum. Microparticles were recently synthesized with a target solution that was dissolved four days prior and the QC assessment determined a radiochemical purity of 99.7%. This suggests that target solutions can be prepared at the reactor and shipped within the US to meet the needs of the end user. Another alternative may be to synthesize the microparticles at MURR and ship them across the US. The stability studies show that the integrity of the microparticles

is preserved after storage at room temperature for a week, therefore the packaging of the microparticles during transit will not require temperature control.

BetaBrach™ has previously been used to treat equine sarcoid patients using the HSA formulation (**Figure 67**). The activity concentration of the microparticle suspension used in these patients was ~5 μCi/μL. The LSA formulation described in Chapter 4 has been used to prepare microparticle suspensions with activity concentrations of up to 40 μCi/μL with >93% radiochemical purity, indicating that the LSA formulation can more than meet the requirements of this therapy.

Figure 67: Preparation for BetaBrach™ microparticle administration to an equine sarcoid patient following external beam radiation therapy. The red arrow denotes the tumor.

REFERENCES

1. Vermeulen, K., Vandamme, M., Bormans, G., Cleeren, F.: Design and Challenges of Radiopharmaceuticals. Seminars in Nuclear Medicine. **49**, 339 (2019).
2. Owunwanne, A.: The Handbook of Radiopharmaceuticals. Springer 2012, p.
3. Bhattacharyya, S., Dixit, M.: Metallic radionuclides in the development of diagnostic and therapeutic radiopharmaceuticals. Dalton Transactions. **40**, 6112 (2011).
4. Drozdovitch, V., Brill, A.B., Callahan, R.J., Clanton, J.A., DePietro, A., Goldsmith, S.J., Greenspan, B.S., Gross, M.D., Hays, M.T., Moore, S.C., Ponto, J.A., Shreeve, W.W., Melo, D.R., Linet, M.S., Simon, S.L.: Use of Radiopharmaceuticals in Diagnostic Nuclear Medicine in the United States. Health Physics. **108**, 520 (2015).
5. Knapp, F.F.R., Dash, A.: Radiopharmaceuticals for Therapy. Springer 2016, p.
6. Loveland, W., Mosrrissey, D.J., Seaborg, G.T.: Modern Nuclear Chemistry. John Wiley & Sons, Inc 2006, p.
7. Mag, H.J.: Alpha Decay. Annu. Rev. Nucl. Sci. **14**, 1 (1964).
8. Konopinski, J.: Beta-Decay. Rev. Mod. Phys. **15**, 209 (1943).
9. Blaser, J.P., Boehm, F., Marmier, P.: The Positron Decay of 18F. Physical Review. **75**, 1953 (1949).
10. Bambynek, W., Behrens, H., Chen, M.H., Crasemann, B., Fitzpatrick, M.L., Ledingham, K.W.D., Genz, H., Mutterer, M., Intemann, R.L.: Orbital electron capture by the nucleus. Reviews of Modern Physics. **49**, 77 (1977).
11. Rösel, F., Fries, H.M., Alder, K., Pauli, H.C.: Internal conversion coefficients for all atomic shells. Atomic Data and Nuclear Data Tables. **21**, 291 (1978).
12. Al-Okour, A.: Radiation Physics: Radiation interaction with matter. Materials Today: Proceedings (2021).
13. Blanksby, S.J., Ellison, G.B.: Bond Dissociation Energies of Organic Molecules. Accounts of Chemical Research. **36**, 255 (2003).
14. Choppin, G., Liljenzin, J.-O., Rydberg, J., Ekberg, C.: Radiation Effects on Matter. In: *Radiochemistry and Nuclear Chemistry*. Elsevier (2013).
15. Mould, R.F.: Pierre Curie, 1859–1906. Current Oncology. **14**, 74 (2007).
16. Carvalho, F.P.: Marie Curie and the Discovery of Radium (2011).
17. Adams, A.: The origin and early development of the Belgian radium industry. Environment International. **19**, 491 (1993).
18. Gunderman, R.B., Gonda, A.S.: Radium Girls. Radiology. **274**, 314 (2015).
19. Hall, J., Angèle, S.: Radiation, DNA damage and cancer. Molecular Medicine Today. **5**, 157 (1999).
20. Baldacchino, G., Parc, D. le, Hickel, B., Gardès-Albert, M., Abedinzadeh, Z., Jore, D., Deycard, S., Bouffard, S., Mouton, V., Balanzat, E., Gardes-Albert, M.: Direct Observation of HO 2 /O 2 - Free Radicals Generated in Water by a High-Linear Energy Transfer Pulsed Heavy-Ion Beam. Radiation Research. **149**, 128 (1998).

21. Hawkins, R.B.: A Statistical Theory of Cell Killing by Radiation of Varying Linear Energy Transfer. Radiation Research. **140**, 366 (1994).
22. Hoglund, E.B.J.C., E.: DNA damage induced by radiation of different linear energy transfer: initial fragmentation. International Journal of Radiation Biology. **76**, 539 (2000).
23. Parker, C., Nilsson, S., Heinrich, D., Helle, S.I., O'Sullivan, J.M., Fosså, S.D., Chodacki, A., Wiechno, P., Logue, J., Seke, M., Widmark, A., Johannessen, D.C., Hoskin, P., Bottomley, D., James, N.D., Solberg, A., Syndikus, I., Kliment, J., Wedel, S., Boehmer, S., Dall'Oglio, M., Franzén, L., Coleman, R., Vogelzang, N.J., O'Bryan-Tear, C.G., Staudacher, K., Garcia-Vargas, J., Shan, M., Bruland, Ø.S., Sartor, O.: Alpha Emitter Radium-223 and Survival in Metastatic Prostate Cancer. New England Journal of Medicine. **369**, 213 (2013).
24. Norum, J., Traasdahl, E.R., Totth, A., Nieder, C., Olsen, J.A.: Health Economics and Radium-223 (Xofigo®) in the Treatment of Metastatic Castration-Resistant Prostate Cancer (mCRPC): A Case History and a Systematic Review of the Literature. Global Journal of Health Science. **8**, 1 (2015).
25. Syed, A.M.N., Puthawala, A., Austin, P., Cherlow, J., Perley, J., Tansey, L., Shanberg, A., Sawyer, D., Baghdassarian, R., Wachs, B., Tomasulo, J., Rao, J., Syed, R.: Temporary iridium-192 implant in the management of carcinoma of the prostate. Cancer. **69**, 2515 (1992).
26. Chargari, C., Deutsch, E., Blanchard, P., Gouy, S., Martelli, H., Guérin, F., Dumas, I., Bossi, A., Morice, P., Viswanathan, A.N., Haie-Meder, C.: Brachytherapy: An overview for clinicians. CA: A Cancer Journal for Clinicians. **69**, 386 (2019).
27. SMITH, T.A.D.: FDG uptake, tumour characteristics and response to therapy. Nuclear Medicine Communications. **19**, 97 (1998).
28. Ollinger, J.M., Fessler, J.A.: Positron-emission tomography. IEEE Signal Processing Magazine. **14**, 43 (1997).
29. Price, E.W., Orvig, C.: Matching chelators to radiometals for radiopharmaceuticals. Chemical Society Review **43**, 260 (2014).
30. Okoye, N.C., Baumeister, J.E., Najafi Khosroshahi, F., Hennkens, H.M., Jurisson, S.S.: Chelators and metal complex stability for radiopharmaceutical applications. Radiochimica Acta. **107**, 1087 (2019).
31. Liu, S., Edwards, D.S.: Bifunctional Chelators for Therapeutic Lanthanide Radiopharmaceuticals. Bioconjugate Chemistry. **12**, 7 (2001).
32. Rayudu, G.V.S.: Production of radionuclides for medicine. Seminars in Nuclear Medicine. **20**, 100 (1990).
33. Qaim, S.M.: Cyclotron Production of Medical Radionuclides. In: *Handbook of Nuclear Chemistry*. Springer US, Boston, MA (2011).
34. Ehrhardt, G.J., Ketring, A.R., Ayers, L.M.: Reactor-produced radionuclides at the University of Missouri Research Reactor. Applied Radiation and Isotopes. **49**, 295 (1998).
35. Qaim, S.M.: Target development for medical radioisotope production at a cyclotron. Nuclear Instruments and Methods in Physics Research Section A:

Accelerators, Spectrometers, Detectors and Associated Equipment. **282**, 289 (1989).
36. Coskun, O.: Separation Tecniques: CHROMATOGRAPHY. Northern Clinics of Istanbul. (2016).
37. De, A.K., Khopkar, S.M., Chalmers, R.A.: SOLVENT EXTRACTION OF METALS. Osti 1970, p.
38. Ali, S.A., Ache, H.J..: Production Techniques of Fission Molybdenum-99. Radiochimica Acta. **41**, 65 (1987).
39. Boyd, R.E.: Technetium-99m generators—The available options. The International Journal of Applied Radiation and Isotopes. **33**, 801 (1982).
40. Dash, A., Chakravarty, R.: Pivotal role of separation chemistry in the development of radionuclide generators to meet clinical demands. RSC Advances. **4**, 42779 (2014).
41. Milenic, D.E., Brady, E.D., Brechbiel, M.W.: Antibody-targeted radiation cancer therapy. Nature Reviews Drug Discovery. **3**, 488 (2004).
42. Kelkar, S.S., Reineke, T.M.: Theranostics: Combining imaging and therapy. Bioconjugate Chemistry. **22**, 1879 (2011).
43. Banerjee, S., Ambikalmajan Pillai, M.R., Ramamoorthy, N.: Evolution of Tc-99m in diagnostic radiopharmaceuticals. Seminars in Nuclear Medicine. **31**, 260 (2001).
44. Deutsch, E., Libson, K., Vanderheyden, J.-L., Ketring, A.R., Maxon, H.R.: The chemistry of rhenium and technetium as related to the use of isotopes of these elements in therapeutic and diagnostic nuclear medicine. International Journal of Radiation Applications and Instrumentation. Part B. Nuclear Medicine and Biology. **13**, 465 (1986).
45. Moustapha, M.E., Ehrhardt, G.J., Smith, C.J., Szajek, L.P., Eckelman, W.C., Jurisson, S.S.: Preparation of cyclotron-produced ^{186}Re and comparison with reactor-produced ^{186}Re and generator-produced ^{188}Re for the labeling of bombesin. Nucl Med Biol. **33**, (2006).
46. Ehrhardt, G.J., Blumer, M.E., Su, F.M., Vanderheyden, J.L., Fritzberg, A.R.: Experience with aluminum perrhenate targets for reactor production of high specific activity Re-186. Applied Radiation and Isotopes. **48**, 1 (1997).
47. Balkin, E.R., Gagnon, K., Dorman, E., Emery, R., Li, Y., Lake Wooten, A., Smith, B.E., Strong, K.T., Pauzauskie, P.J., Fassbender, M.E., Cutler, C.S., Ketring, A.R., Jurisson, S.S., Scott Wilbur, D.: Scale-up of high specific activity ^{186g}Re production using graphite-encased thick ^{186}W targets and demonstration of an efficient target recycling process. Radiochimica Acta. **105**, 1071 (2017).
48. Fassbender, M.E., Ballard, B., Birnbaum, E.R., Engle, J.W., John, K.D., Maassen, J.R., Nortier, F.M., Lenz, J.W., Cutler, C.S., Ketring, A.R., Jurisson, S.S., Wilbur, D.S.: Proton irradiation parameters and chemical separation procedure for the bulk production of high-specific-activity ^{186g}Re using WO_3 targets. Radiochimica Acta. **101**, 339 (2013).
49. Lapi, S., Mills, W.J., Wilson, J., McQuarrie, S., Publicover, J., Schueller, M., Schyler, D., Ressler, J.J., Ruth, T.J.: Production cross-sections of $^{181-186}$Re isotopes from

proton bombardment of natural tungsten. Applied Radiation and Isotopes. **65**, 345 (2007).
50. Bonardi, M.L., Groppi, F., Manenti, S., Persico, E., Gini, L.: Production study of high specific activity NCA Re-186g by proton and deuteron cyclotron irradiation. Applied Radiation and Isotopes. **68**, 1595 (2010).
51. Alekseev, I.E., Lazarev, V. v.: Cyclotron production and radiochemical isolation of the therapeutical radionuclide ^{186}Re. Radiochemistry. **48**, 497 (2006).
52. Balkin, E.R., Gagnon, K., Strong, K.T., Smith, B.E., Dorman, E.F., Emery, R.C., Pauzauskie, P.J., Fassbender, M.E., Cutler, C.S., Ketring, A.R., Jurisson, S.S., Wilbur, D.S.: Deuteron irradiation of W and WO_3 for production of high specific activity ^{186}Re: Challenges associated with thick target preparation. Applied Radiation and Isotopes. **115**, 197 (2016).
53. Gott, M.D., Hayes, C.R., Wycoff, D.E., Balkin, E.R., Smith, B.E., Pauzauskie, P.J., Fassbender, M.E., Cutler, C.S., Ketring, A.R., Wilbur, D.S., Jurisson, S.S.: Accelerator-based production of the ^{99m}Tc-^{186}Re diagnostic-therapeutic pair using metal disulfide targets (MoS_2, WS_2, OsS_2). Applied Radiation and Isotopes. **114**, 159 (2016).
54. Tan, C., Zhang, H.: Two-dimensional transition metal dichalcogenide nanosheet-based composites. Chemical Society Reviews. **44**, 2713 (2015).
55. Zhao, G., Wu, Y., Shao, Y., Hao, X.: Large-quantity and continuous preparation of two-dimensional nanosheets. Nanoscale. **8**, 5407 (2016).
56. Lei, W., Xiao, J.-L., Liu, H.-P., Jia, Q.-L., Zhang, H.-J.: Tungsten disulfide: synthesis and applications in electrochemical energy storage and conversion. Tungsten. **2**, 217 (2020).
57. Goethals, P.-E., Zimmermann, R.: Cyclotrons Used in Nuclear Medicine World Market Report & Directory. 2015, p. 74–185.
58. Charles, A., Najafi, F.K., Ma, L., Munindradasa, C., Hoerres, R., Lydon, J.D., Kelley, S.P., Guthrie, J., Rotsch, D., Medvedev, D., Cutler, C.S., Li, Y., Wilbur, D.S., Hennkens, H.M., Jurisson, S.S.: Evaluation of $^{186}WS_2$ target material for production of high specific activity ^{186}Re via proton irradiation: Separation, radiolabeling and recovery/recycling. Radiochimica Acta. **1**, (2022).
59. Makris, G., Radford, L.L., Kuchuk, M., Gallazzi, F., Jurisson, S.S., Smith, C.J., Hennkens, H.M.: NOTA and NODAGA [^{99m}Tc]Tc- and [^{186}Re]Re-Tricarbonyl Complexes: Radiochemistry and First Example of a [^{99m}Tc]Tc-NODAGA Somatostatin Receptor-Targeting Bioconjugate. Bioconjugate Chemistry. **29**, 4040 (2018).
60. Shigeta, N., Matsuoka, H., Osa, A., Koizumi, M., Izumo, M., Kobayashi, K., Hashimoto, K., Sekine, T., Lambrecht, R.M.: Production method of no-carrier-added ^{186}Re. Journal of Radioanalytical and Nuclear Chemistry Articles. **205**, 85 (1996).
61. Hussain, M., Sudár, S., Aslam, M.N., Malik, A.A., Ahmad, R., Qaim, S.M.: Evaluation of charged particle induced reaction cross section data for production of the important therapeutic radionuclide ^{186}Re. Radiochimica Acta. **98**, 385 (2010).

62. Maxon, H.R., Schroder, L.E., Thomas, S.R., Hertzberg, V.S., Deutsch, E.A., Scher, H.I., Samaratunga, R.C., Libson, K.F., Williams, C.C., Moulton, J.S.: Re-186(Sn) HEDP for treatment of painful osseous metastases: initial clinical experience in 20 patients with hormone-resistant prostate cancer. Radiology. **176**, 155 (1990).
63. Van Gog, F.B., Visser, G.W., Stroomer, J.W., Roos, J.C., Snow, G.B., van Dongen, G.A.: High dose rhenium-186-labeling of monoclonal antibodies for clinical application: pitfalls and solutions. Cancer. **15**, 80 (1997).
64. Yordanova, A., Eppard, E., Kürpig, S., Bundschuh, R., Schönberger, S., Gonzalez-Carmona, M., Feldmann, G., Ahmadzadehfar, H., Essler, M.: Theranostics in nuclear medicine practice. OncoTargets and Therapy. **10**, 4821 (2017).
65. Knapp, F.F., Mirzadeh, S., Beets, A.L.: Reactor production and processing of therapeutic radioisotopes for applications in nuclear medicine. Research and Development of Isotopes. 93 (1996).
66. Zhang, X., Li, Q., Li, W., Sheng, R., Shen, S.: Production of no-carrier-added ^{186}Re via deuteron induced reactions on isotopically enriched ^{186}W. Applied Radiation and Isotopes. **54**, 89 (2001).
67. Zhu, Z.H., Wang, X.Y., Wu, Y.H., Liu, Y.F.: An improved Re/W separation protocol for preparation of carrier-free ^{186}Re. Journal of Radioanalytical and Nuclear Chemistry. **221**, 199 (1997).
68. Gott, M.: Accelerator-based production of high specific activity radionuclides for radiopharmaceutical applications, (2015).
69. Ziegler, J.F., Ziegler, M.D., Biersack, J.P.: SRIM – The stopping and range of ions in matter (2010). Nuclear Instruments and Methods in Physics Research Section B: Beam Interactions with Materials and Atoms. **268**, 1818 (2010).
70. Burgeson, I.E., Blanchard Jr., D.L., Deschane, J.R.: Small column testing of Superlig 639 for removing 99Tc from Hanford Tank Waste 241-AN-102 Supernate (Evelope C) Mixed with Tank 241-C-104 Solids (Envelope D) Wash and Permeate Solutions. 2004, p.
71. Hyde, A.M., Zultanski, S.L., Waldman, J.H., Zhong, Y.-L., Shevlin, M., Peng, F.: General Principles and Strategies for Salting-Out Informed by the Hofmeister Series. Organic Process Research & Development. **21**, 1355 (2017).
72. Kozak, R.W., Raubitschek, A., Mirzadeh, S., Brechbiel, M.W., Junghaus, R., Gansow, O.A., Waldmann, T.A.: Nature of the Bifunctional Chelating Agent Used for Radioimmunotherapy with Yttrium-90 Monoclonal Antibodies: Critical Factors in Determining in Vivo Survival and Organ Toxicity. Cancer Research. **49**, 2639 (1989).
73. Walker, L.A.: Radioactive Yttrium 90: A review of its properties, biological behavior, and clinical uses. Acta Radiologica: Therapy, Physics, Biology. **2**, 302 (1964).
74. Kim, Y.-C., Kim, Y.-H., Uhm, S.-H., Seo, Y.S., Park, E.-K., Oh, S.-Y., Jeong, E., Lee, S., Choe, J.-G.: Radiation Safety Issues in Y-90 Microsphere Selective Hepatic Radioembolization Therapy: Possible Radiation Exposure from the Patients. Nuclear Medicine and Molecular Imaging. **44**, 252 (2010).

75. Murthy, R., Nunez, R., Szklaruk, J., Erwin, W., Madoff, D.C., Gupta, S., Ahrar, K., Wallace, M.J., Cohen, A., Coldwell, D.M., Kennedy, A.S., Hicks, M.E.: Yttrium-90 Microsphere Therapy for Hepatic Malignancy: Devices, Indications, Technical Considerations, and Potential Complications. RadioGraphics. **25**, S41 (2005).
76. Geschwind, J.F.H., Salem, R., Carr, B.I., Soulen, M.C., Thurston, K.G., Goin, K.A., van Buskirk, M., Roberts, C.A., Goin, J.E.: Yttrium-90 microspheres for the treatment of hepatocellular carcinoma. Gastroenterology. **127**, S194 (2004).
77. Kallini, J.R., Gabr, A., Salem, R., Lewandowski, R.J.: Transarterial radioembolization with yttrium-90 for the treatment of hepatocellular carcinoma. Advances in Therapy. **33**, 699 (2016).
78. Chargari, C., Deutsch, E., Blanchard, P., Gouy, S., Martelli, H., Guérin, F., Dumas, I., Bossi, A., Morice, P., Viswanathan, A.N., Haie-Meder, C.: Brachytherapy: An overview for clinicians. CA: A Cancer Journal for Clinicians. **69**, 386 (2019).
79. Wang, W., Fliedner, F.P., Hansen, A.E., Eliasen, R., Melander, F., Kjaer, A., Andresen, T.L., Jensen, A.I., Henriksen, J.R.: Preclinical evaluation of cationic DOTA-triarginine-lipid conjugates for theranostic liquid brachytherapy. Nanotheranostics. **4**, 142 (2020).
80. Wilson, D.A., Frank, R.K., Simon, J., Crump, D.K.: Radioactive compositions and methods for their therapeutic use, (2012).
81. INTERNATIONAL ATOMIC ENERGY AGENCY: THERAPEUTIC RADIONUCLIDE GENERATORS: 90Sr/90Y AND 188W/188Re GENERATORS. , Vienna 2009, p.
82. Chakravarty, R., Dash, A.: Availability of Yttrium-90 from Strontium-90: A Nuclear Medicine Perspective. Cancer Biotherapy and Radiopharmaceuticals. **27**, 621 (2012).
83. Dyrssen, D., Christiansen, J., Moutschen-Dahmen, M., Noer, B., Reio, L.: Separation of Strontium-90 and Yttrium-90 and the Preparation of Carrier-free Yttrium-90. Acta Chemica Scandinavica. **11**, 1277 (1957).
84. Boldeman, J.W., Allen, B.J., Musgrove, A.R. de L., Macklin, R.L.: The Neutron Capture Cross Section of Yttrium-89. Nuclear Science and Engineering. **64**, 744 (1977).
85. Lee, S.-H., Kim, K.-W., Lee, B.-T., Bang, S., Kim, H., Kang, H., Jang, A.: Enhanced Arsenate Removal Performance in Aqueous Solution by Yttrium-Based Adsorbents. International Journal of Environmental Research and Public Health. **12**, 13523 (2015).
86. Haron, M.J., Wasay, S.A., Tokunaga, S.: Preparation of Basic Yttrium Carbonate for Phosphate Removal. Water Environment Federation. **69**, 1047 (1997).
87. Gad, S.C.: Rodents model for toxicity testing and biomarkers. In: *Biomarkers in Toxicology*. Elsevier (2014).
88. Bolger, G.T.: Routes of Drug Administration ☆. In: *Reference Module in Biomedical Sciences*. Elsevier (2018).
89. Ikotun, O., Clarke, B., Sunderland, J.: A Snapshot of United States PET Cyclotrons and Radiopharmaceutical Production Operations and Locations. Journal of Nuclear Medicine. **53**, 1085 (2012).

90. Goethals, P.-E., Zimmerman, R.: Cyclotrons Edition 2015 THE MOST COMPREHENSIVE EVALUATION REPORT AND DIRECTORY WRITTEN BY EXPERTS IDENTIFYING MORE THAN 1,200 MEDICAL CYCLOTRONS WORLDWIDE. 2015, p.
91. Zakalek, P., Doege, P.-E., Baggemann, J., Mauerhofer, E., Brückel, T.: Energy and target material dependence of the neutron yield induced by proton and deuteron bombardment. EPJ Web of Conferences. **231**, 03006 (2020).
92. Kim, D.: Radiation Capabilities at Brookhaven National Laboratory. 2018, p. 1–20.

Appendix A: Production and Radiochemical Evaluation of ^{105}Rh from Recycled ^{104}Ru Metal Target

Part of this work is reprinted (adapted) with permission from Nkemakonam C. Okoye, Tim E. Phelps, Anster Charles, Donald E. Wycoff, John D. Lydon, Mary F. Embree, James Guthrie, Steven P. Kelley, Charles L. Barnes, Alan R. Ketring, Heather Hennkens and Silvia S. Jurisson. Recovery, Recycling and Re-irradiation of Enriched ^{104}Ru Metal Targets for Cost Effective Production of ^{105}Rh. Applied Radiation and Isotopes. Dec 2020.

1 Introduction

Rhodium-105 has been of interest since Grazman and Troutner first identified it as a potential therapeutic radionuclide. Rhodium-105 (half-life = 35.4 hours) is a moderate energy beta emitter [β^-_{max} = 567 keV (75%), β^-_{avg} = 152 keV], with low energy gamma emissions [319 keV (19%) and 306 keV (5%)]. The beta energy of ^{105}Rh is comparable to the beta energies of ^{177}Lu (β^-_{avg} = 134 keV) and ^{131}I (β^-_{avg} = 182 keV), which are currently used in FDA-approved therapeutic radiopharmaceuticals.

A very attractive chemical property of Rh is the kinetic inertness of Rh(III) complexes, which favors a low spin octahedral d^6 arrangement. This suggests that ^{105}Rh(III) complexes should exhibit high *in vivo* stability since they should be stable to transchelation by serum proteins. With this in mind, ^{105}Rh(III) complexes have been investigated as potential radiotherapeutic agents. Various chelates have been evaluated,

including derivatives of cyclam and cyclen, diethylenetriamine, amine oxime, porphyrin, tetradentate thiamacrocycles, tetrathioethers, and diaminedithioethers. The reported biological distribution studies in mice highlight the potential clinical utility of ^{105}Rh for the development of therapeutic radiopharmaceuticals.

Rhodium-105 can be produced directly in high specific activity (HSA) in a reactor from ^{235}U fission via the ^{235}U(n,f)^{105}Rh reaction or from fast neutron irradiation of ^{105}Pd via the ^{105}Pd(n,p)^{105}Rh reaction. Indirect production of ^{105}Rh at the University of Missouri Research Reactor Center (MURR) involves thermal neutron (~9.78 x 10^{13} n/cm^2/s) irradiation of an enriched (>99%) ^{104}Ru metal target to give ^{105}Ru (half-life = 4.4 hours), which subsequently decays by beta particle emission to ^{105}Rh (**Equation 7**).

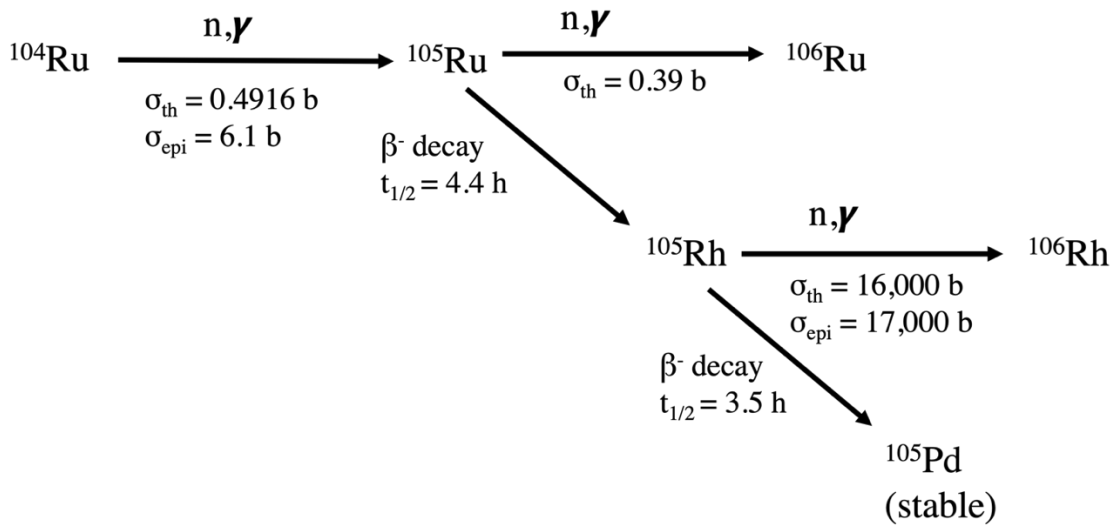

Equation 7. Production of ^{105}Rh

Following decay of ^{105}Ru to ^{105}Rh, the residual ^{104}Ru metal target is oxidized to [^{104}Ru]RuO_4 using hypochlorite generated *in situ* by bubbling Cl_2 into a 2 M NaOH

solution containing the target. The resultant [^{104}Ru]RuO_4 is then separated from the ^{105}Rh daughter by distillation at ~90 °C and trapped in 3 M HCl for recovery and recycling (**Figure 68**).

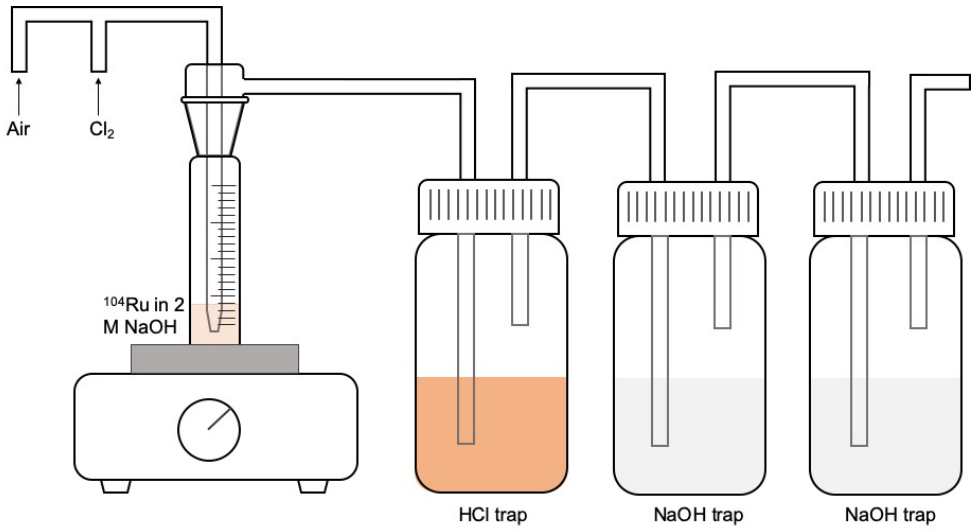

Figure 68. Schematic for ^{105}Rh separation

Ruthenium has seven naturally occurring stable isotopes, with ^{104}Ru present in 18.62% abundance. Hence, a highly enriched ^{104}Ru target is necessary for the production of ^{105}Rh in high radionuclidic purity. Due to the high cost of the enriched ^{104}Ru metal target (>99%; ~$20,000/g), it is necessary that the target material be recovered for reuse in order to make routine ^{105}Rh production economically feasible. Less than 1% of the total ^{104}Ru atoms are converted to ^{105}Ru atoms following neutron irradiation and thus, the ^{104}Ru metal target can be reused multiple times if successfully recovered. A process to recover and reuse enriched ^{104}Ru metal targets, which were previously irradiated to produce several batches of ^{105}Rh over a period of more than two decades, is described in this study. The recovered ^{104}Ru metal is fully characterized and re-irradiated to produce ^{105}Rh.

Initial ^{105}Rh-labeling studies using [^{105}Rh]$RhCl_3$ produced from the recovered ^{104}Ru are also reported.

2 Experimental

2.1 Production of ^{105}Rh from Recycled ^{104}Ru Metal Target

Three separate neutron irradiations of the recycled ^{104}Ru metal and one irradiation of new ^{104}Ru metal were performed at MURR, as summarized in **Table 12**. The theoretical yields were calculated using IsoChain based on **Equation 2**. Briefly, ^{104}Ru metal target material (1-5 mg) was encapsulated in a 4 x 6 mm quartz vial and irradiated for ~90 hours with neutrons ($\Phi_{thermal}$ ~9.78 (or 9.53) x 10^{13} n/cm^2/s; $\Phi_{epithermal}$ 2.93 (or 2.86) x 10^{12} n/cm^2/s; ~3% of thermal flux) at a MURR neutron reflector position. A 24-hour cooling period was allowed to ensure the decay of ^{105}Ru (4.4 h half-life) into ^{105}Rh. After the cooling period, the total activity of the irradiated target in the quartz vial was measured on an Atomlab 100 radioisotope calibrator (Biodex; setting 171). Subsequently, the quartz vial was scored and broken, and the irradiated target was transferred into a 30 mL glass midget impinger containing 2 mL of 2 M NaOH. The impinger was connected to one 3 M HCl (500 mL) and two 5 M NaOH (500 mL) traps using Teflon-lined tubing as shown schematically in **Figure 68**.

Table 12. ^{105}Rh production from recycled ^{104}Ru metal target at MURR						
Production Run	^{104}Ru Target* (mg)	Irradiation time (h)	Theoretical ^{105}Rh activity** (mCi)	Initial ^{105}Rh activity (mCi)***	Recovered ^{105}Rh activity (mCi)	% ^{105}Rh recovery (decay corrected)****
1[a]	1.44	90.02	6.18	7.17	1.50	24.3
2[b]	3.24	89.15	14.31	23.90	3.30	23.1
3[b]	4.78	89.67	21.06	38.20	19.79	94.0
4[b]	4.46	90.02	19.63	36.60	19.10	97.3

*Recycled ^{104}Ru metal target was used except for Production Run 2. **Based on Bateman Equation and accounting for product burn-up. [a]9.53E13 n/cm^2/s thermal flux, 2.86E12 n/cm^2/s epithermal flux. [b]9.78E13 n/cm^2/s thermal flux, 2.93E12 n/cm^2/s epithermal flux. ***Includes activity from ^{104}Ru, ^{24}Na and possible others present in irradiated quartz vial. ****Based on theoretical activity value.

$$N_{Rh-105} = N^0_{Ru-104} \cdot \Lambda^*_{Ru-104} \cdot \Lambda^*_{Ru-105} \left[\frac{e^{-\Lambda_{Ru-104} \cdot t}}{(\Lambda_{Ru-105} - \Lambda_{Ru-104})(\Lambda_{Rh-105} - \Lambda_{Ru-104})} + \ldots \right]$$

$$\Lambda^*_{Ru-104} = \phi\sigma \qquad \phi_{th} = 9.53E13 / 9.78E13 \text{ n/cm}^2\text{s}$$

$$\Lambda^*_{Ru-105} = \lambda_{Ru-105} \qquad \phi_{epi} = 2.86E12 / 2.93E12 \text{ n/cm}^2\text{s}$$

Equation 8. Formula used to predict ^{105}Rh production yields.

The bulk ^{104}Ru metal target was separated from the ^{105}Rh produced by oxidation of ^{104}Ru metal to [^{104}Ru]RuO_4 using hypochlorite generated *in situ*, and subsequent distillation of [^{104}Ru]RuO_4 at elevated temperatures. To accomplish this, Cl_2 at ~30 mL/min (50 seconds for production 1 and 2, 2 minutes for production 3, and 5 minutes for production 4) was then bubbled into the impinger containing the irradiated ^{104}Ru metal target in 2 mL of 2 M NaOH. The impinger was heated at 40 °C for 1 hour under constant airflow (~30 mL/min). Additional Cl_2 at ~30 mL/min (12 minutes for productions 1 and 2, and 25

minutes for productions 3 and 4) was bubbled into the impinger followed by heating at 90 °C for 1 hour under constant airflow (~30 mL/min). The target solution was filtered through a 0.8 μm PES syringe filter into a clean midget impinger. The solution was heated for an additional 30 minutes at 90 °C under constant airflow (~30 mL/min). Finally, 0.25 mL of 1 M HCl was added to the solution, which was then heated for 30 minutes at 90 °C without airflow. Rhodium-105 was obtained in a final volume of ~ 2 mL as a mixture of ^{105}Rh chloride species including $[^{105}Rh]RhCl_3(OH_2)_3$, $[^{105}Rh]RhCl_4(OH_2)_2^{1-}$, $[^{105}Rh]RhCl_5(OH_2)_2^{2-}$, and $[^{105}Rh]RhCl_6^{3-}$, as previously determined by electrophoretic analysis. The radionuclidic purity of the final ^{105}Rh stock solution was evaluated by HPGe gamma spectroscopy. Additionally, a 200-µL aliquot of the ^{105}Rh stock solution was analyzed by inductively coupled plasma mass spectrometry (ICP-MS) after decay of ^{105}Rh.

3 Results and Discussion

3.1 Production of ^{105}Rh from Recycled ^{104}Ru Metal Target

Three separate neutron irradiations of the recycled ^{104}Ru metal (production 1, 3 and 4) and one irradiation of new ^{104}Ru metal (production 2) were performed at MURR as summarized in **Table 12**. The ^{105}Rh recovery in productions 3 and 4 (94.0% and 97.3%, respectively) was significantly higher than the ^{105}Rh recovery from productions 1 and 2 (24.3% and 23.1%, respectively). The time for Cl_2 bubbling during the target processing procedure in productions 3 and 4 was more than double that used in productions 1 and 2. Bubbling more Cl_2 into NaOH solution would potentially generate more hypochlorite *in situ*, which would facilitate the dissolution of the ^{104}Ru target and the release of ^{105}Rh into

the solution. This might explain why the ^{105}Rh recovery was higher in productions 3 and 4, which had more time for Cl_2 bubbling.

Although high ^{105}Rh recovery was achieved in productions 3 and 4, visual inspection of the midget impinger during the dissolution of the recycled ^{104}Ru target revealed that the target did not completely dissolve, given that some very fine black particles were still observed after heating *in situ* generated hypochlorite for 1 hour at 40 °C. It is possible that the high temperatures required during the target recycling process might have affected the particle size of the metal powder, thereby making it more difficult to dissolve. However, excellent recovery of ^{105}Rh was observed in both production runs. HPGe gamma spectrometry analysis of the final ^{105}Rh stock solutions revealed the predominant gamma peaks associated with ^{105}Rh (318 and 306 keV). However, very minimal impurities from ^{24}Na (< 0.1%) at 1368 keV were observed. The ^{24}Na impurity is most likely from the neutron activation of NaCl contaminants contained in the recycled ^{104}Ru metal, which is consistent with what was observed in the NAA analyses. No other radionuclide impurities were identified.

3 Conclusions

In this study, a method for the recovery of ^{104}Ru metal trapped in 3 M HCl solution for over two decades from previous ^{105}Rh productions at MURR is reported. The target recovery process involves concentrating the 3 M HCl solutions to dryness to yield hydrated ruthenium chloride ($[^{104}Ru]RuCl_3{\cdot}xH_2O$), dehydrating $[^{104}Ru]RuCl_3{\cdot}xH_2O$ with Ar at 525 °C, and subsequently reducing to ^{104}Ru metal with H_2 at 800 °C. ICP-MS

analysis determined that the isotopic enrichment of the recovered metal target was 98.94% ^{104}Ru (originally purchased as 99.21 and 99.05%). Neutron activation analysis of the recovered ^{104}Ru metal target produced mainly ^{105}Ru, with very minimal amounts of ^{24}Na (0.3% of total ^{105}Ru) from neutron activation of minor NaCl contaminants in the recovered ^{104}Ru metal.

Supplemental Material

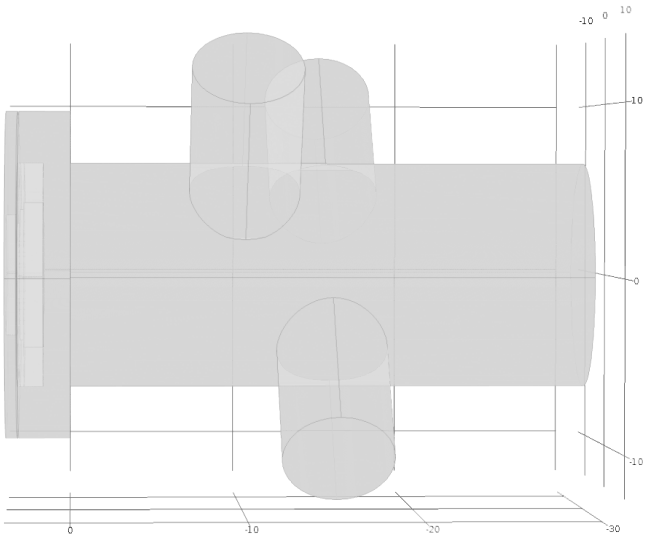

S1: 3D model of the pressed $^{186}WS_2$ target and water-cooling system designed using COMSOL Multiphysics

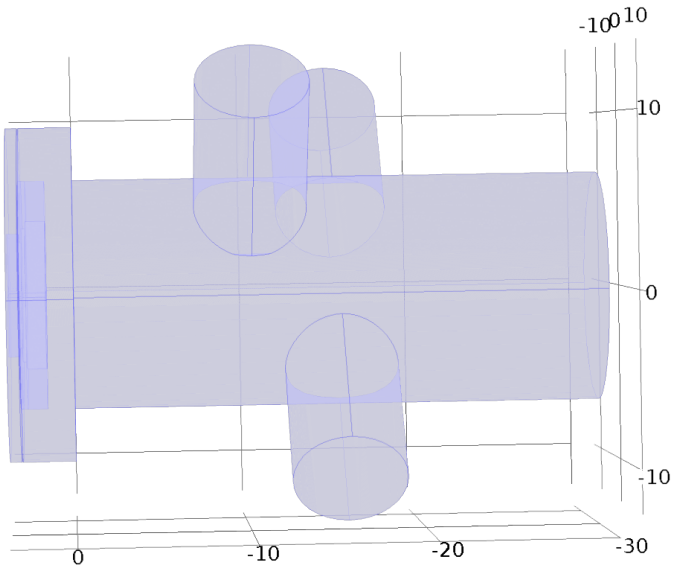

S2: 3D model of the pressed $^{186}WS_2$ target and water-cooling system designed using COMSOL Multiphysics showing the temperature insulation boundaries highlighted in blue.

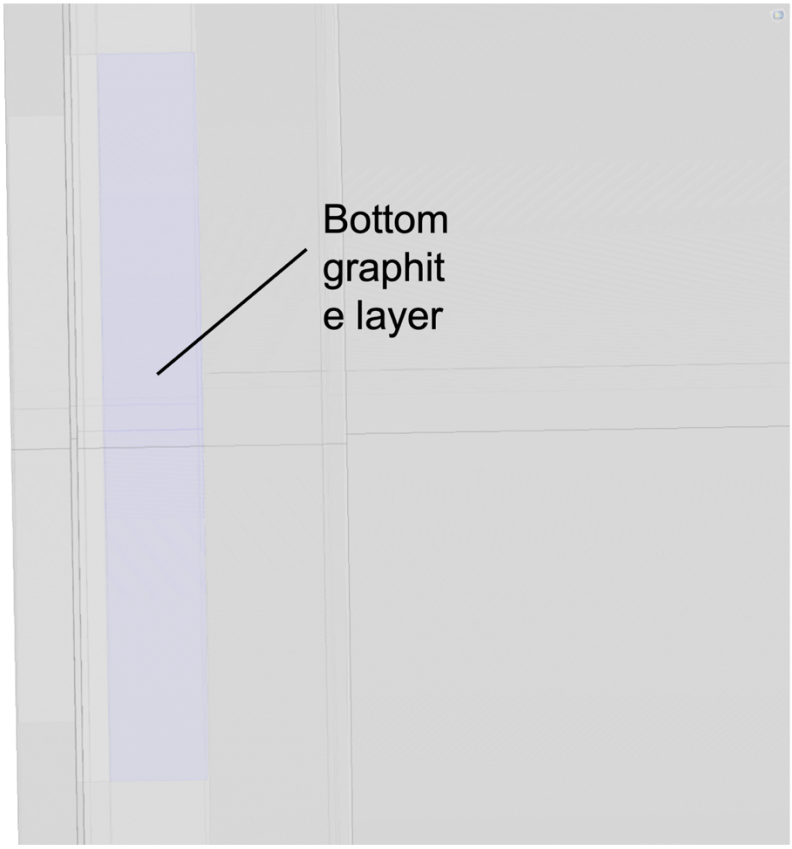

S3: 3D model of the pressed $^{186}WS_2$ target and water-cooling system designed using COMSOL Multiphysics showing the bottom graphite layer highlighted in blue.

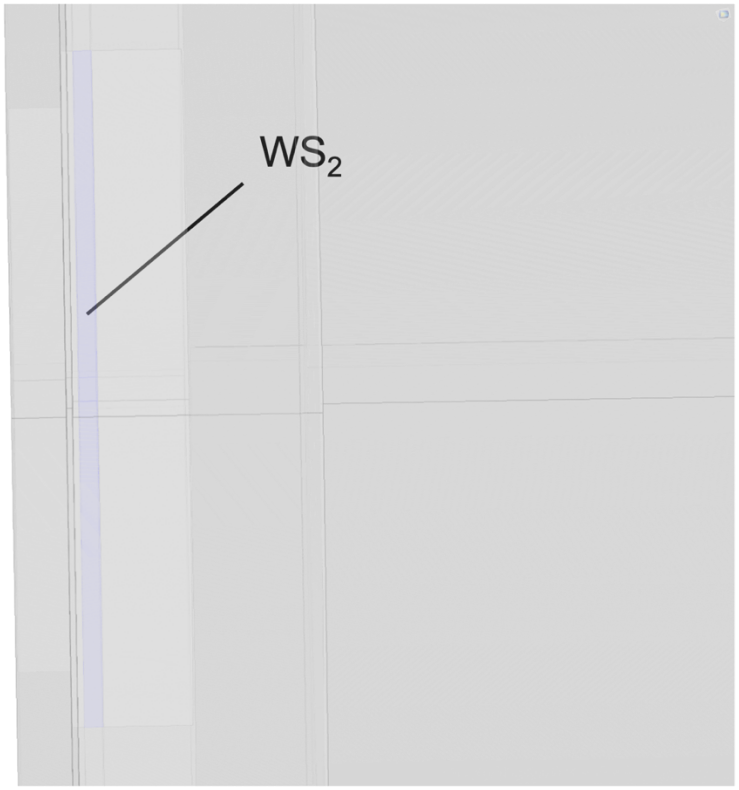

S4: 3D model of the pressed $^{186}WS_2$ target and water-cooling system designed using COMSOL Multiphysics showing the $^{186}WS_2$ layer highlighted in blue.

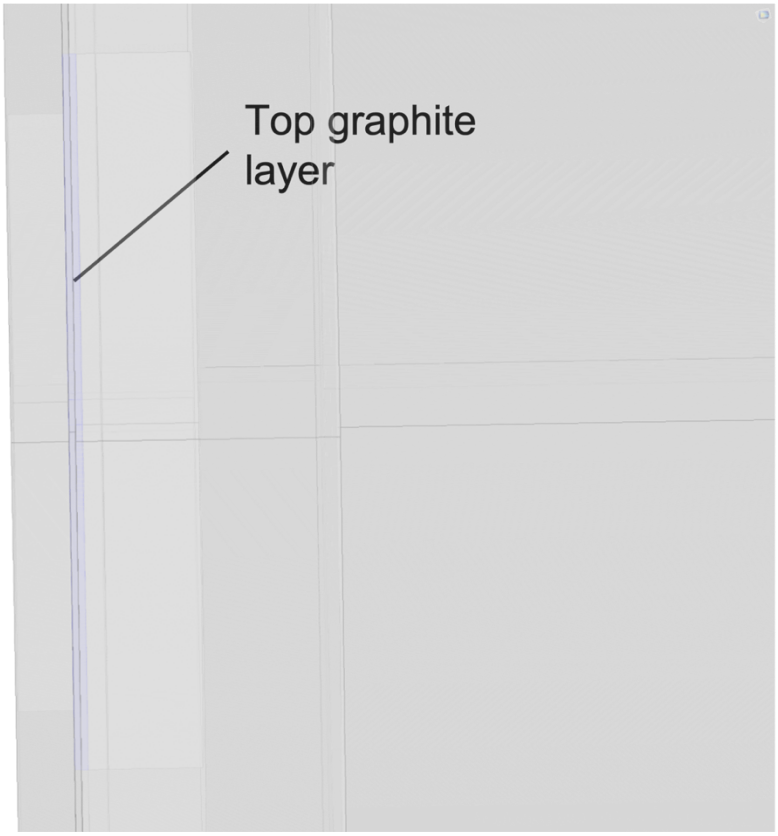

S5: 3D model of the pressed $^{186}WS_2$ target and water-cooling system designed using COMSOL Multiphysics showing the top graphite layer highlighted in blue.

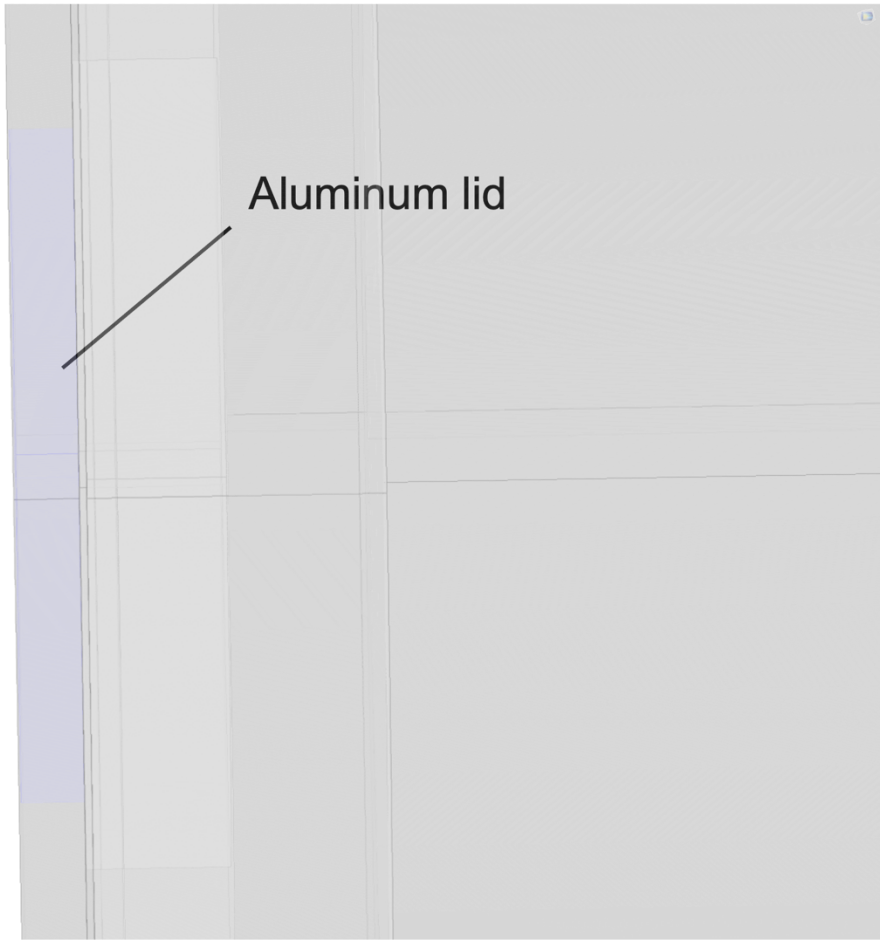

S6: 3D model of the pressed $^{186}WS_2$ target and water-cooling system designed using COMSOL Multiphysics showing the aluminum lid highlighted in blue.

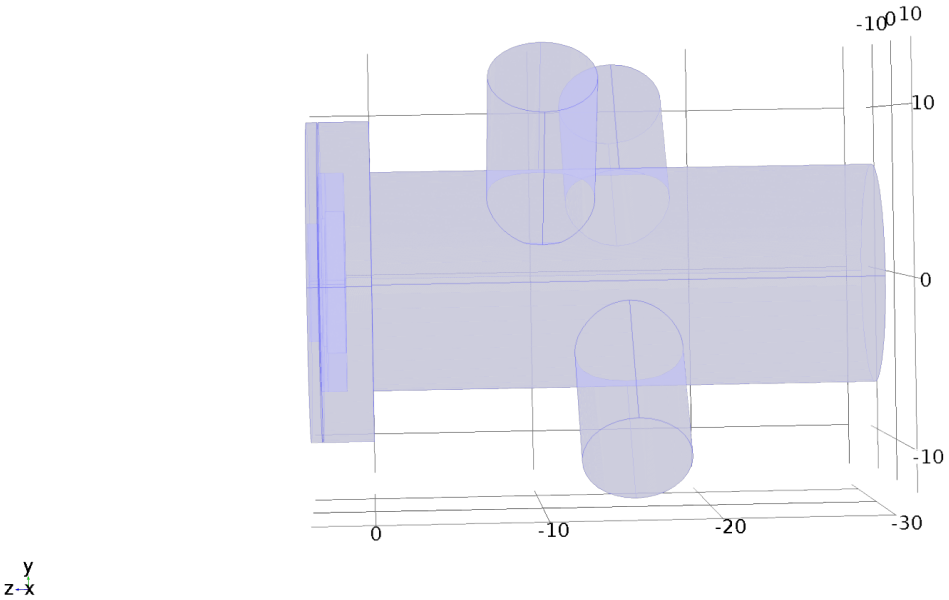

S7: 3D model of the pressed $^{186}WS_2$ target and water-cooling system designed using COMSOL Multiphysics showing the heat transfer domains highlighted in blue.

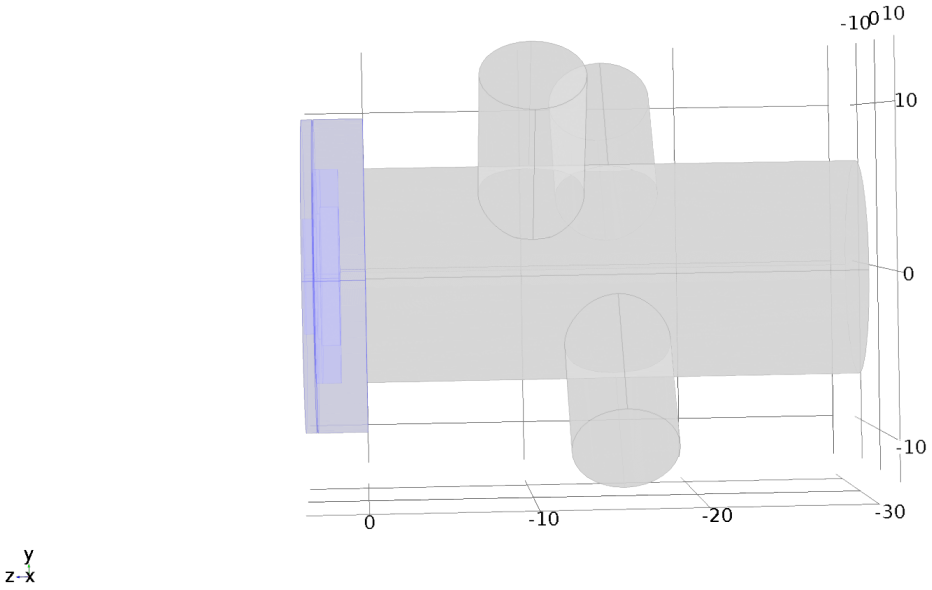

S8: 3D model of the pressed $^{186}WS_2$ target and water-cooling system designed using COMSOL Multiphysics showing the heat transfer in solid domains highlighted in blue.

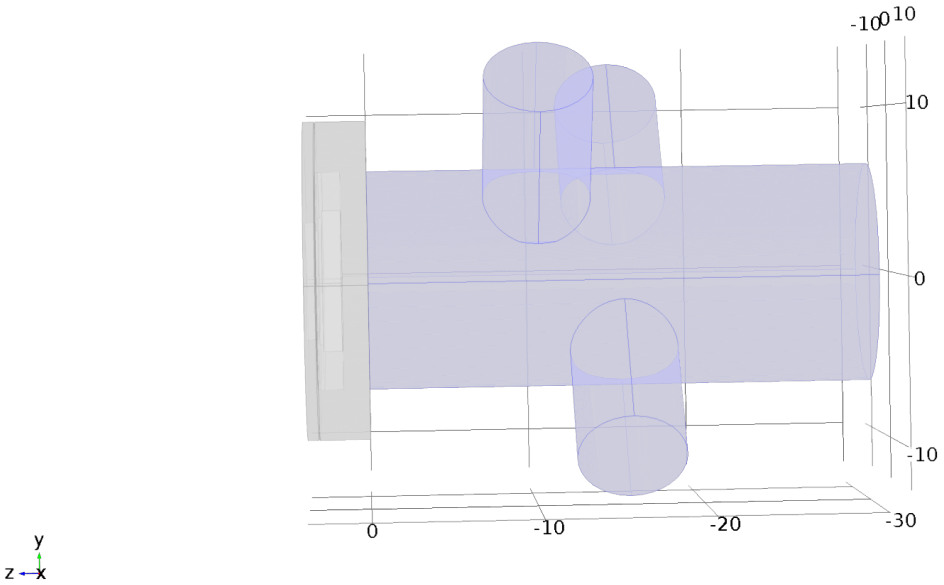

S9: 3D model of the pressed $^{186}WS_2$ target and water-cooling system designed using COMSOL Multiphysics showing the heat transfer in fluid domains highlighted in blue.

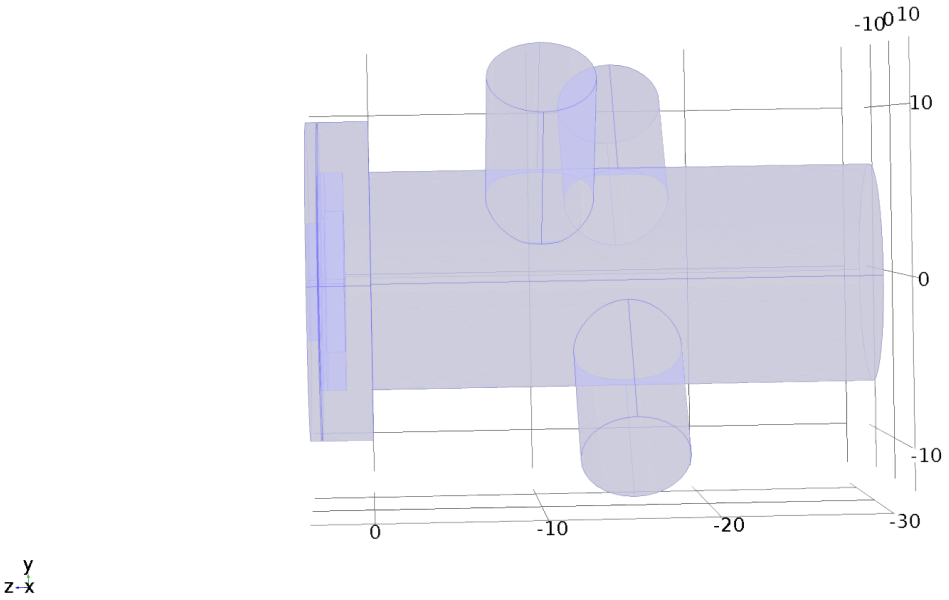

S10: 3D model of the pressed $^{186}WS_2$ target and water-cooling system designed using COMSOL Multiphysics showing the initial temperature of 293 K domains highlighted in blue

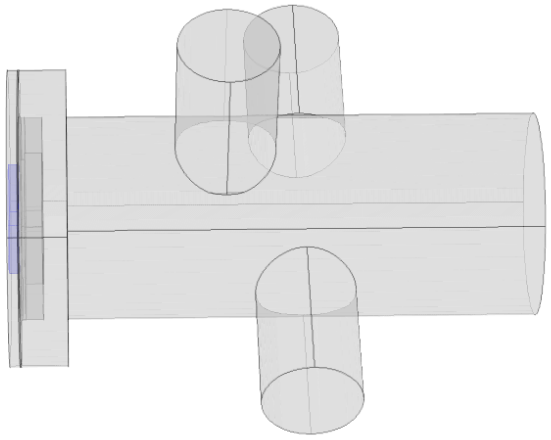

S11: 3D model of the pressed $^{186}WS_2$ target and water-cooling system designed using COMSOL Multiphysics showing the source of heat generated from the proton beam degradation in the aluminum lid highlighted in blue.

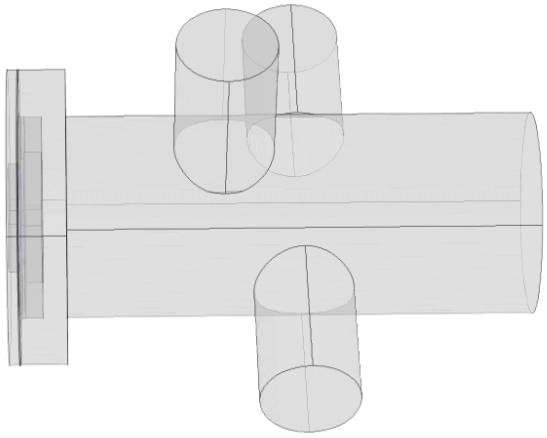

S12: 3D model of the pressed $^{186}WS_2$ target and water-cooling system designed using COMSOL Multiphysics showing the source of heat generated from the proton beam degradation in the top graphite layer highlighted in blue.

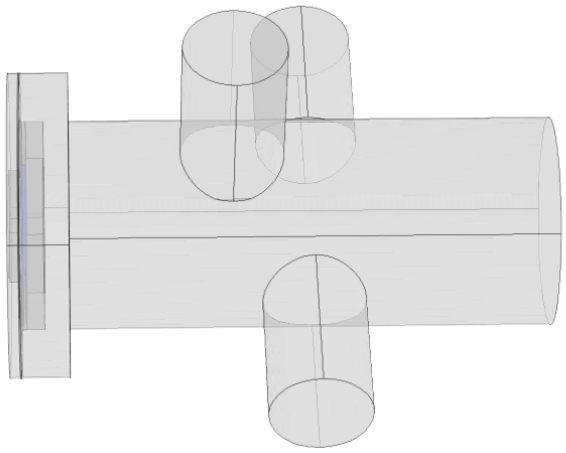

S13: 3D model of the pressed $^{186}WS_2$ target and water-cooling system designed using COMSOL Multiphysics showing the source of heat generated from the proton beam degradation in the $^{186}WS_2$ layer highlighted in blue.

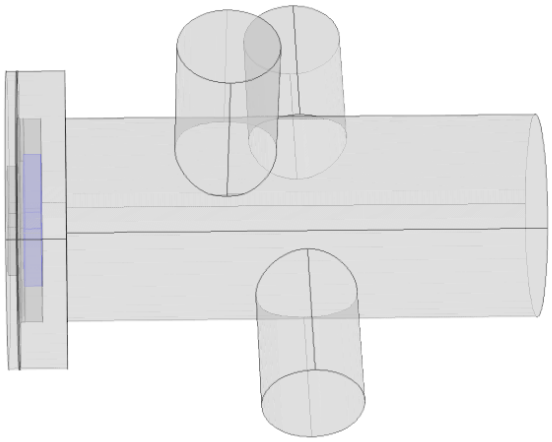

S14: 3D model of the pressed $^{186}WS_2$ target and water-cooling system designed using COMSOL Multiphysics showing the source of heat generated from the proton beam degradation in the bottom graphite layer highlighted in blue.

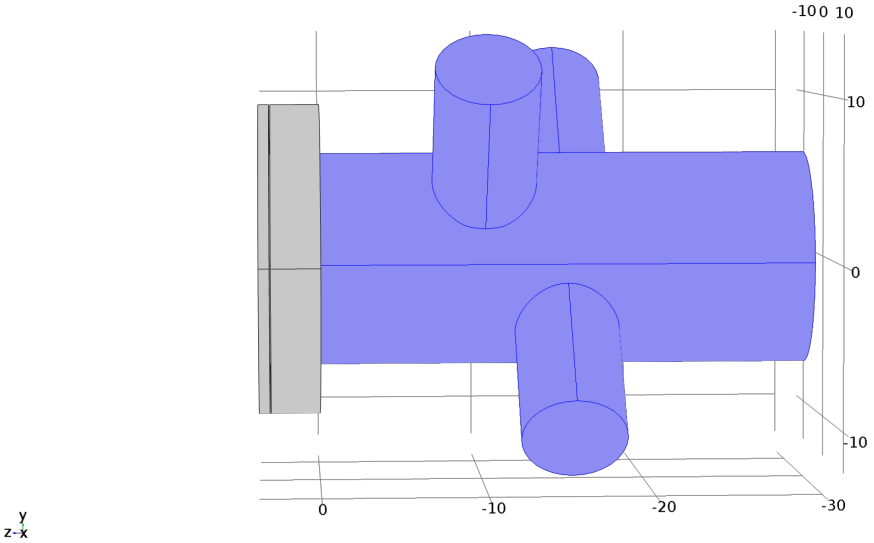

S15: 3D model of the pressed $^{186}WS_2$ target and water-cooling system designed using COMSOL Multiphysics showing the turbulent flow fluid domain highlighted in blue.

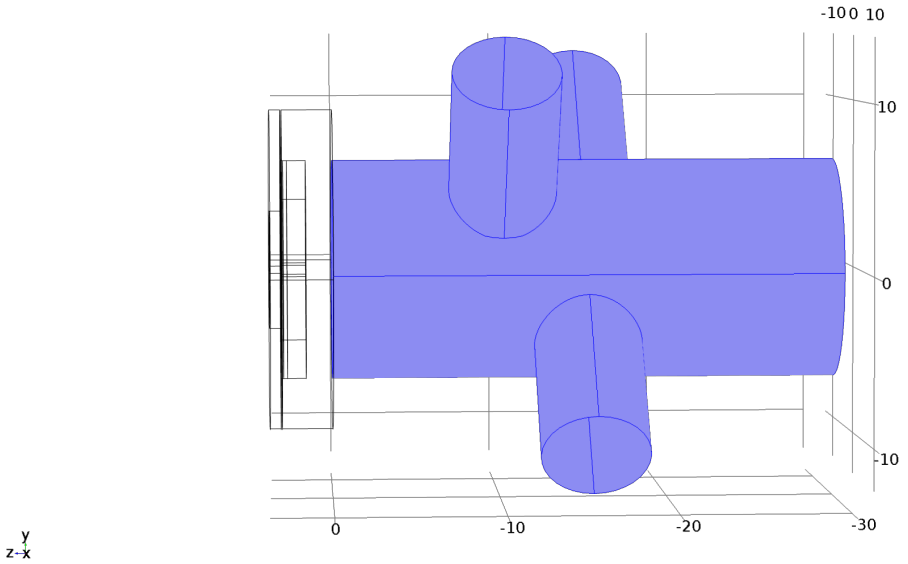

S16: 3D model of the pressed $^{186}WS_2$ target and water-cooling system designed using COMSOL Multiphysics showing the wall fluid domain highlighted in blue.

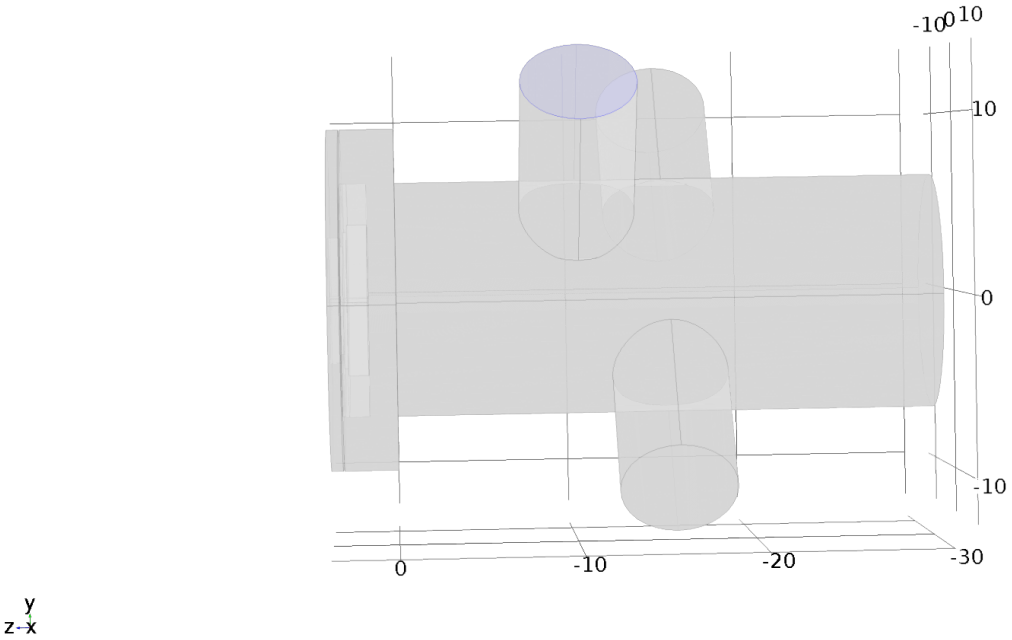

S17: 3D model of the pressed $^{186}WS_2$ target and water-cooling system designed using COMSOL Multiphysics showing the 20 °C temperature domain at the water inlet highlighted in blue.

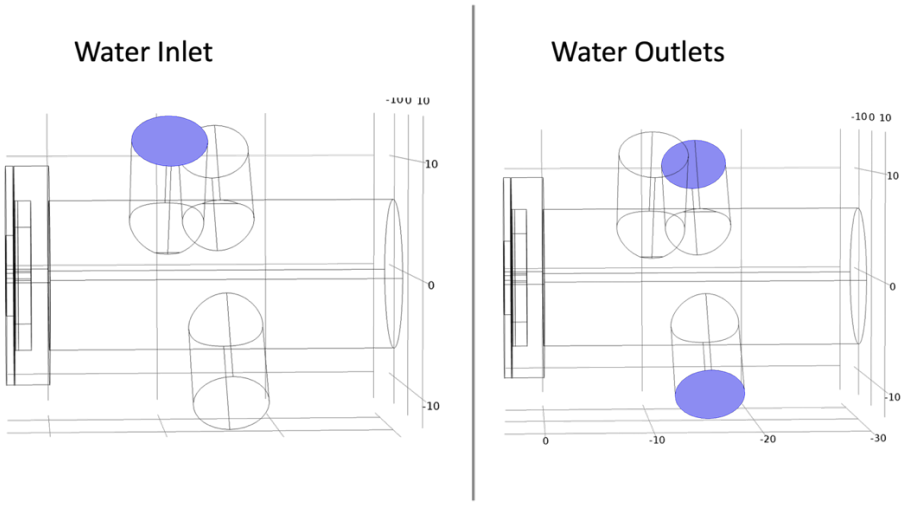

S19: 3D model of the pressed $^{186}WS_2$ target and water-cooling system designed using COMSOL Multiphysics showing the water inlet and outlets highlighted in blue.

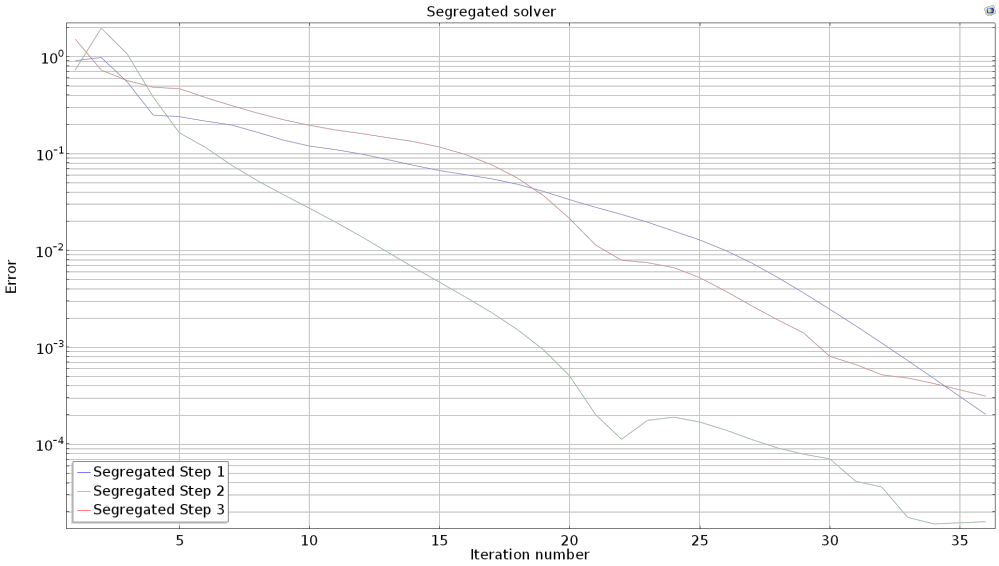

S19: Convergence plot generated by the stationary solver in COMSOL Multiphysics.

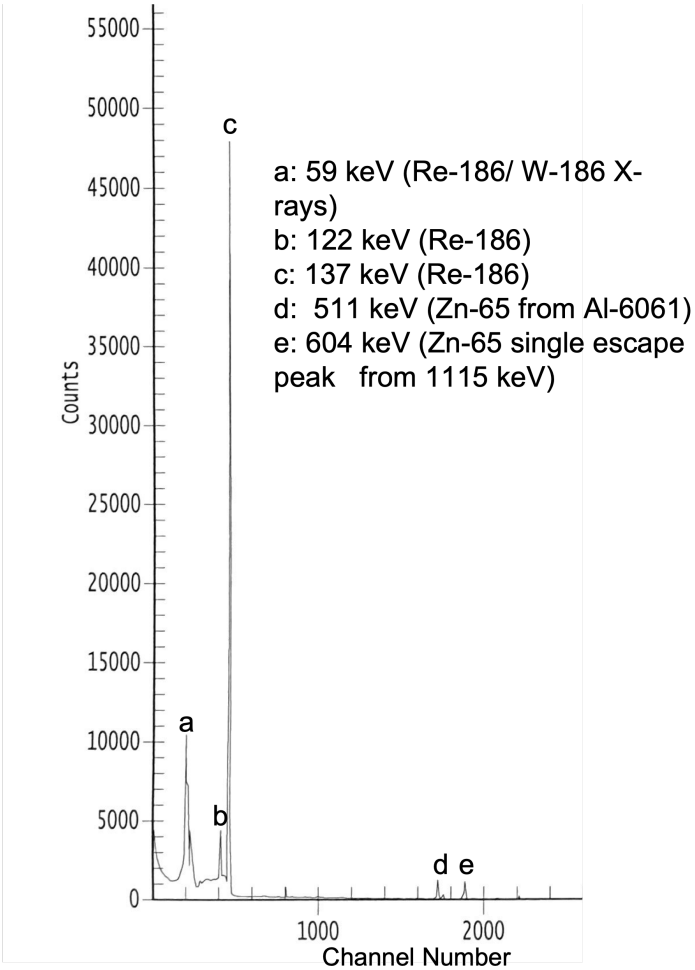

Figure S20: HPGe spectrum of dissolved target aliquot before purification

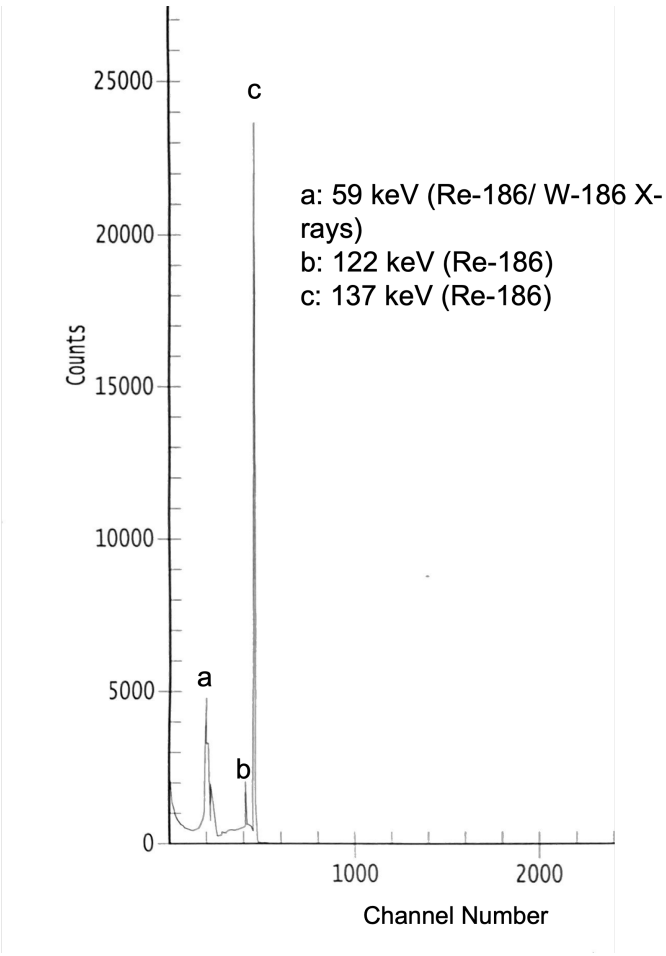

Figure S21: HPGe spectrum of purified ^{186}Re aliquot

Table S22: ICP-MS results (ppm or mg/g material) for the purchased $^{186}WO_3$, the synthesized $^{186}WS_2$, the recovered ^{186}W, and the separated ^{186}Re

Sample	**Origin**		**Atom %**				
		Re	**^{180}W**	**^{182}W**	**^{183}W**	**^{184}W**	**^{186}W**
$^{186}WO_3$	Isoflex	13.1	1 x 10^{-7}	0.000210	0.000135	0.000133	0.9983
$^{186}WS_2$	Synthesized	10.7	6 x 10^{-7}	0.000206	0.000139	0.000132	0.9983
^{186}W	Recovered	<LOD	3.2 x 10^{-7}	0.00037	0.00022	0.000153	0.99788
		Re	**W total**				
^{186}Re	Isolated	0.0324	0.2089				

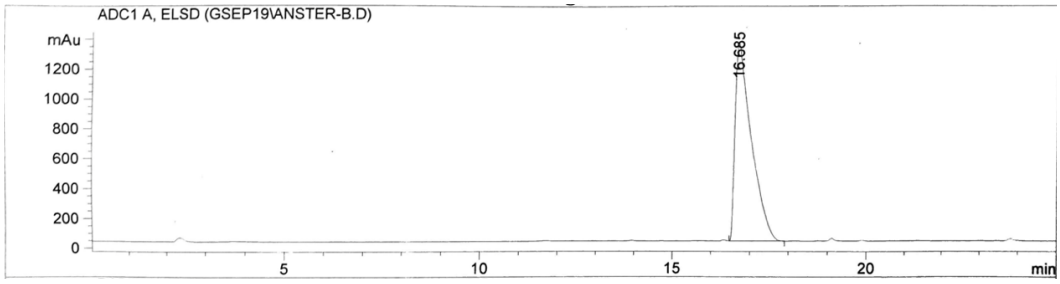

S23. HPLC Chromatogram of trityl protected 222-MAMA-N-proprionate at 16.685 minutes (30-100 % H_2O/MeCN in 15 min, 1 mL/min).

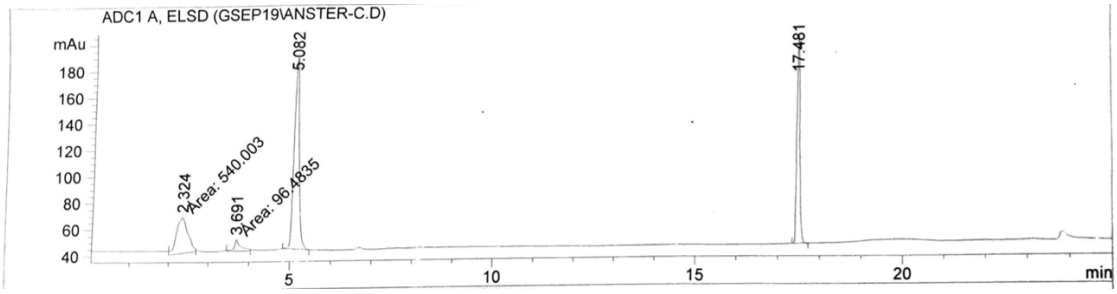

S24: HPLC Chromatogram of de-protected 222-MAMA-N-proprionate at 5.082 minutes (30-100 % H_2O/MeCN in 15 min, 1 mL/min).

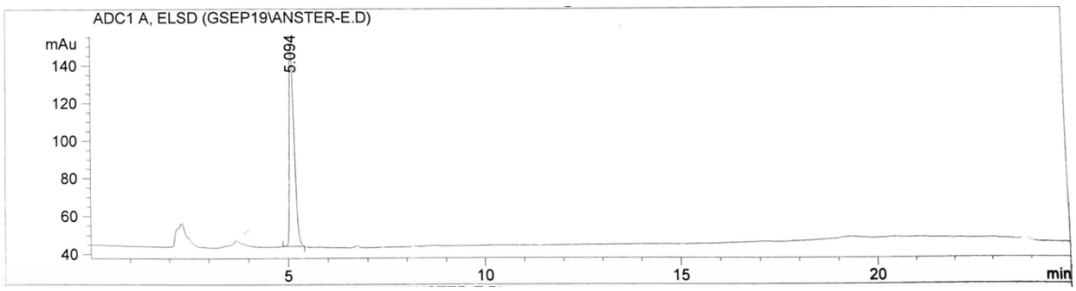

S25. HPLC Chromatogram of purified de-protected 222-MAMA-N-proprionate at 5.094 minutes (30-100 % H_2O/MeCN in 15 min, 1 mL/min).

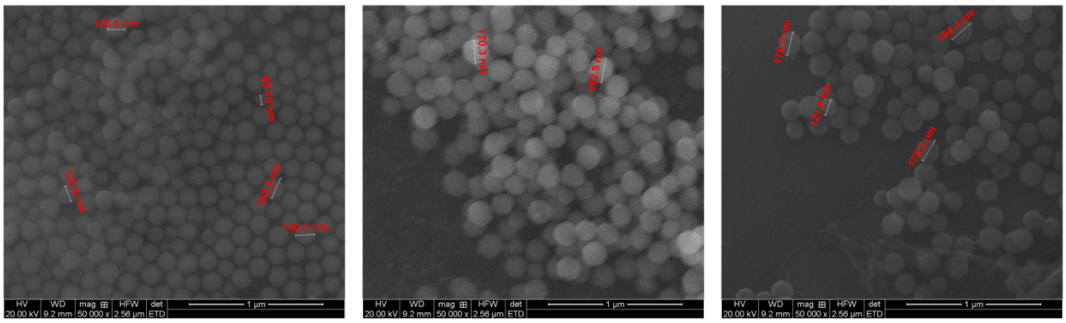

S26: Left to right, SEM images of microparticles synthesized for reaction end timepoints of 20, 40, and 60 min.

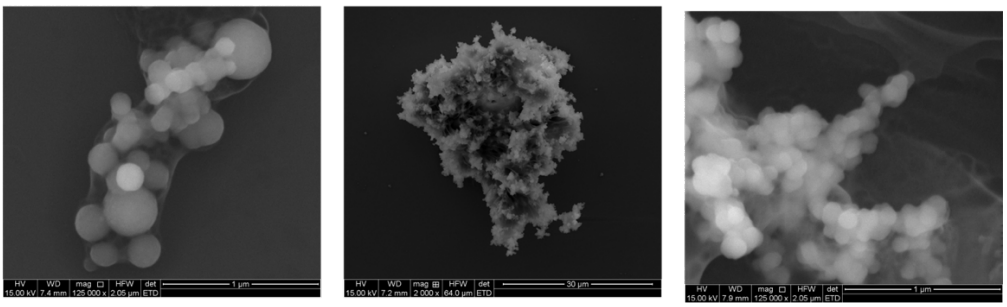

S27: SEM images of microparticles synthesized using the urease method

VITA

Anster Charles was born in Castries, Saint Lucia on June 19th, 1990 to Antoine Charles and Alice Charles. He graduated from the Saint Mary's College High School in Castries, Saint Lucia in May of 2007 and pursued a career as an amateur track and field athlete and laboratory technician until August 2013, when he matriculated at Coppin State University in Baltimore, Maryland for a bachelor's degree in chemistry through a track and field scholarship. During his tenure at Coppin, he interned at Pfizer's Analytical Research and Development department at their Groton campus in the summer of 2016. Anster graduated in the following year and joined the doctoral program in chemistry at the University of Missouri – Columbia. He will receive his PhD in chemistry in July of 2022.